Intrinsic Electrical Remodeling Underlies Atrioventricular Block in Athletes

Pietro Mesirca, Shu Nakao, Sarah Dalgas Nissen, Gabriella Forte, Cali Anderson, Tariq Trussell, Jue Li, Charlotte Cox, Min Zi, Sunil Logantha, et al.

Full title: Intrinsic electrical remodelling underlies atrioventricular block in athletes

Running title: Mesirca; Electrical remodelling of the AV node in athletes

Authors: Pietro Mesirca[1*], Shu Nakao[2,3*], Sarah Dalgas Nissen[4*], Gabriella Forte[2], Cali Anderson[2], Tariq Trussell[2], Jue Li[2], Charlotte Cox[2], Min Zi[2], Sunil Logantha[2,5], Sana Yaar[2], Helena Cartensen[4], Isabelle Bidaud[1], Luke Stuart[2], Luca Soattin[2], Gwilym M Morris[2], Paula A da Costa Martins[6], Elizabeth J Cartwright[2], Delvac Oceandy[2], Matteo E Mangoni[1], Thomas Jespersen[7], Rikke Buhl[4], Halina Dobrzynski[2,8], Mark R Boyett[2,7†], Alicia D'Souza[2†]

*Equal contribution

†Joint senior authors

Affiliations: [1]IGF, Université de Montpellier, CNRS, INSERM, Montpellier, France; [2]Division of Cardiovascular Sciences, University of Manchester, UK; [3]Department of Biomedical Sciences, Ritsumeikan University, Japan; [4]Department of Veterinary Clinical Sciences, Faculty of Health and Medical Sciences, University of Copenhagen, Denmark; [5]Liverpool Centre for Cardiovascular Sciences, University of Liverpool, UK; [6]Department of Cardiology, Maastricht University, Maastricht, Netherlands; [7]Department of Biomedical Sciences, University of Copenhagen, Denmark; [8]Department of Anatomy, Jagiellonian University Medical College, Poland

Corresponding author: Dr Alicia D'Souza, Division of Cardiovascular Sciences, University of Manchester, 46 Grafton Street, Manchester, UK; Phone: +4401612751226; Email: Alicia.dsouza@manchester.ac.uk

Word Count: 13057; **Subject Codes:** exercise physiology, arrhythmia, cardiac electrophysiology, ion channels/membrane transport, microRNA

ABSTRACT

Rationale: Athletes present with atrioventricular node (AV node) dysfunction manifesting as AV block. This can necessitate electronic pacemaker implantation, known to be more frequent in athletes with a long training history.

Objective: AV block in athletes is attributed to high vagal tone. Here we investigated the alternative hypothesis that electrical remodelling of the AV node is responsible.

Methods and results: Radio-telemetry ECG data and AV node biopsies were collected in sedentary and trained Standardbred racehorses, a large-animal model of the athlete's heart. Trained horses presented with longer PR intervals (that persisted under complete autonomic block) *versus* sedentary horses, concomitant with reduced expression of key ion channels involved in AV node conduction: L-type Ca^{2+} channel subunit $Ca_V1.2$ and the hyperpolarization-activated cyclic nucleotide gated channel 4 (HCN4). AV node electrophysiology was explored further in mice; prolongation of the PR interval (*in vivo* and *ex vivo*), Wenckebach cycle length and AV node refractory period was observed in mice trained by swimming *versus* sedentary mice. Transcriptional profiling in laser-capture microdissected AV node revealed striking reduction in pacemaking ion channels in trained mice, translating into protein downregulation of $Ca_V1.2$ and HCN4. Correspondingly, patch clamp recordings in isolated AV node myocytes demonstrated a training-induced reduction in $I_{Ca,L}$ and I_f density that likely contributed to the observed lower frequency of action potential firing in trained cohorts. microRNA (miR) profiling and *in vitro* studies revealed miR-211-5p and miR-432 as direct regulators of $Ca_V1.2$ and HCN4. *In vivo* miRs suppression or detraining restored training-induced PR prolongation and ion channel remodelling.

Conclusions: Training-induced AV node dysfunction is underscored by likely miR-mediated transcriptional remodelling that translates into reduced current density of key ionic currents involved in impulse generation and conduction. We conclude that electrical

remodelling is a key mechanism underlying AV block in athletes.

Keywords: AV block, Athletic training, Electrophysiology, Ion channels, microRNAs

Non-standard abbreviations: AV, atrioventricular node; AVERP, atrioventricular node effective refractory period; τ, time constant; miR, microRNA

INTRODUCTION

Despite its many well-recognised cardiovascular benefits, it is now accepted that sustained endurance exercise leads to the development of cardiac arrhythmias including atrial fibrillation,[1-5] sinus bradycardia[6-8] and atrioventricular (AV) block (also known as heart block).[6, 9, 10] AV block (impairment of conduction through the AV node), is a common occurrence in athletes, manifesting as a longer PR interval (first degree AV block), a prolonged Wenckebach cycle length (minimum cycle length at which the AV node fails to conduct in a 1:1 manner) and second-degree AV block (intermittent block of conduction through the AV node).[10-12] AV block in athletes has been correlated to the intensity and length of the training period;[13] in veteran endurance athletes, the prevalence of first- and second-degree AV block has been recorded as ranging from 28–45% and 15–40% respectively,[14] in contrast to 0.60% and 0.03% in the general population.[15] Several studies have also noted the presence of asystolic pauses in athletes that last from 1.6 to 15 s.[7, 8, 16] In athletes, first-degree and type-I second-degree AV block are generally considered as benign physiological changes; however, recent large-scale clinical studies have concluded that type-I second-degree AV block increases the risk of atrial fibrillation and pacemaker implantation in later life.[17-19] AV block may also present symptomatically; in second-degree AV block, conduction failure through the AV node can result in syncope or palpitations.[20] These observations likely contribute to the increased incidence of electronic pacemaker implantation reported in veteran athletes.[6, 21]

Despite this evidence of a burden of AV node dysfunction in veteran athletes, there

is very limited study of the underlying mechanisms. AV block in athletes is currently attributed to the autonomic nervous system–a supposed increase in vagal tone induced by training,[22] even though vagal tone has never been directly measured in athletes.[23] Furthermore, previous work in human athletes has demonstrated that AV node dysfunction in trained athletes *versus* sedentary subjects (typified by a prolonged Wenckebach cycle length and AV node effective refractory period, AVERP), persisted even under complete pharmacological block of the autonomic nervous system.[10] This implicates a role for intrinsic training-induced electrophysiological alterations, as we have previously described in the sinus node of human athletes[24] and rodent models.[24, 25] Here, using equine and rodent models of endurance training combined with *in vivo*, *in vitro* and *in silico* approaches, we demonstrate for the first time, a predominant role for intrinsic electrical remodelling in training-induced AV node dysfunction. We go on to show that AV node ion channel expression is under the control of the miR network and test the therapeutic potential of targeting noncoding miRs to rescue AV node dysfunction

METHODS

The data that support the findings of this study are available from the corresponding author upon reasonable request. Detailed methods are given in the Online Supplemental Material. 24-hour Holter recordings were obtained from sedentary, trained and detrained Standardbred trotters. PR intervals were measured in horses at baseline and after complete block of the autonomic nervous system by intravenous injection of 0.04 mg/kg atropine and 0.20 mg/kg propranolol. Right atrial biopsies encompassing the AV node were dissected and the component structures of the equine AV conduction axis identified histologically and by immunolabelling. $Ca_V1.2$ and HCN4 expression were quantified by immunohistochemistry and western blotting. miRs were assessed by qPCR. Training-induced AV node dysfunction was explored further in mice; in the first set of experiments 8 to 10-week-old male C57BL6/j mice were trained by swimming for 20 weeks to model

long-term exercise training in humans. At the end of the training period, in the anaesthetised mouse echocardiography was performed and the electrocardiogram (ECG) was recorded *in vivo* (at baseline and on complete autonomic block achieved by intraperitoneal injection of 0.5 mg/kg atropine and 1 mg/kg propranolol). AV node function was tested *in vivo* (by programmed electrical stimulation) and *ex vivo* (in the isolated, denervated AV node). Right atrial biopsies encompassing the AV node were frozen, cryosectioned and subjected to histology and immunolabelling to enable laser-capture microdissection of AV node and right atrial regions and subsequent qPCR analysis of 96 key mediators of AV node automaticity and conduction. Protein levels of selected ion channels were assessed by immunolabelling, and current density of corresponding ionic currents tested by patch clamp in isolated AV node myocytes. Patch clamp data were incorporated into a biophysically detailed, one-dimensional model of the AV node to simulate the effect of training on AV node conduction. The effect of the funny current (I_f) selective blocker ivabradine on the PR interval in trained and sedentary animals was tested *in vivo*. The role of miRs in training-induced AV node transcriptional remodelling was assessed by profiling the expression levels of 750 miRs. Specific interactions between dysregulated miRs and selected ion channels was verified by luciferase reporter gene assays and site directed mutagenesis. The effect of overexpression of miR-211-5p and miR-432 on endogenous ion channel transcription was tested by qPCR and western blot in embryonic stem (ES) cell-derived myocytes that expressed $Ca_v1.2$ and HCN4.

In the course of the study it was determined that swim-training mice for 60 min, twice per day for four weeks produced analogous prolongation of the PR interval and remodelling of AV node ion channels as observed with the longer training duration described above. In line with the ethical principles of the 3Rs (Replacement, Reduction, Refinement), further studies were carried out in mice trained for this duration, including assessment of (i) training-induced change to I_K and action potential morphology and

duration in isolated myocytes with patch clamp and (ii) the impact of *in vivo* suppression of miR-211-5p and miR-432 on training-induced PR prolongation. The latter was achieved by administering a combination of cholesterol-conjugated antimiRs followed by *in vivo* electrophysiology, Western blot and qPCR to characterise the mice and study $Ca_V1.2$ and HCN4 remodelling. Finally, the effect of detraining on the ECG and transcript expression of $Ca_V1.2$ and HCN4 was assessed following a detraining period of 12 weeks. Statistically significant differences were determined using an appropriate test- See Statistical Analysis Table; $P<0.05$ was regarded as significant.

RESULTS

Evidence of AV node dysfunction and ion channel remodelling in trained racehorses

Experiments were conducted on trained (n=13) and sedentary (n=6) horses, a high fidelity model of the athlete's heart (further explored in the **Discussion**).[26, 27] First, ECGs from trained and sedentary horses were analysed to establish training-induced changes. **Figure 1A** illustrates a typical ECG recording from a sedentary horse. The ECG has a QRS complex following every P wave; in **Figure 1B-D** representative traces from trained racehorses are given, illustrating variations of second-degree AV block, characterised by intermittent conduction block and absent QRS complexes. Note that in this work we did not distinguish between type I and type II second-degree AV block (considered further in the Methods section of the Data Supplement). **Figure 1E** shows the resting heart rate under baseline conditions and, as expected, the heart rate was significantly lower in trained horses. Further analysis revealed that trained racehorses also presented with a significantly longer PR interval **(Figure 1F)** and a trend towards an increase in the number of episodes of second-degree AV block compared to sedentary horses **(Figure 1G).** The effect of detraining on the ECG changes was investigated by comparing trained horses with a separate cohort of horses (n=5) that had been detrained for varying durations between 2 - 60 months. The ECG changes were reversible on detraining: the resting heart

rate increased to that typical of sedentary horses in an exponential manner with a time constant, τ, of 10.3 months (**Figure 1H**; R^2=0.69); the PR interval declined with a τ = 2.5 months (**Figure 1I**; R^2=0.31). These data show that in horses, as in humans, exercise training induces reversible sinus bradycardia and PR prolongation.

24 h Holter recordings were obtained from a further cohort of 5 trained and 5 sedentary horses to study the natural variation of heart rate and the PR interval under resting conditions. Trained horses presented with slower minimal and maximal heart rates (given in beats/min {bpm}; minimum, 30±2 bpm; maximum, 43±2 bpm) compared to sedentary horses (minimum, 32±1 bpm; maximum, 49±2 bpm). Notably, as given in **Figure 1J**, prolongation of the PR interval in trained horses was apparent at both minimum (325.4±11.1 ms *versus* 380.6±27.3 ms) and maximum (297.8±7.1 ms *versus* 326.2±11.8 ms) heart rates. A 2-way ANOVA showed that the PR interval was longer both at slower heart rates ($P=2.1 \times 10^{-3}$) and in trained animals ($P=8.21 \times 10^{-2}$); however, the interaction between heart rate and training status was not significant ($P=1.82 \times 10^{-1}$). This analysis indicates that the difference in the PR interval between sedentary and trained horses in this cohort does not depend upon the underlying heart rate. Importantly, previous characterisation of the intrinsic rate-dependent properties of the AV node have unequivocally demonstrated that a faster basic rate produces an intrinsically longer AV node conduction time.[28-30] Therefore, in this study the intrinsic training-induced slowing of PR conduction cannot be explained by the underlying heart rate difference between sedentary and trained animals.

The training-induced AV node dysfunction could be the result of altered autonomic nerve activity to the heart (for example, increased vagal tone) or a change in the intrinsic properties of the AV node. To test the involvement of the autonomic nervous system, sedentary and trained were subjected to complete autonomic blockade. Autonomic blockade was achieved by intravenous injection of 0.20 mg/kg

propranolol and 0.04 mg/kg atropine. Doses of atropine and propranolol were based on Hamlin *et al*.,[31] who made dose-response measurements in healthy horses and showed complete block for up to 45 min under agonist challenge. **Figure 1K shows** that the prolongation of the PR interval induced by training persisted under complete block of the autonomic nervous system (262.8±6.5 ms in sedentary horses *versus* 274.0±2.0 ms in trained horses) whereas no incidences of high-degree AV block were recorded under conditions of autonomic blockade. We thus conclude that in this study first degree AV block in trained horses under resting conditions cannot be fully attributed to autonomic influences and intrinsic mechanisms must be considered.

Potential intrinsic mechanisms underlying AV node dysfunction were investigated in AV node tissue from sedentary and trained horses. The precise location and structure of the AV node in horses has not been established and Masson's trichrome staining was used to identify key histological features of the horse AV conduction axis. **Figure 1L** shows the compact node, morphologically defined by its position adjacent to the musculature of the AV septum. The small, packed cells of the compact node were interwoven within a matrix of connective tissue and bordered by transitional cells that distinguished it from the longitudinally oriented working atrial myocardium. The serial sections continued inferiorly through the conduction axis illustrating the penetrating bundle of His, the left and right bundle branches and Purkinje fibres that were embedded deep within connective tissue (data not shown). As increased extracellular matrix deposition is commonly invoked as a mechanism underlying slowed AV node conduction,[32] collagen deposition in the AV node was assessed in immunolabelled sections using ZEN Intellesis (Zeiss) - a machine learning-based tool that enabled image segmentation and pixel classification to identify the extracellular matrix. Representative images given in **Online Figure IA-B** demonstrate that the collagen area fraction was not altered in sedentary *versus* trained horses.

Next, the role of ion channel remodelling within the AV node was investigated. Histological identification was further supplemented by immunohistochemical labelling with antibodies against HCN4 to confirm the presence of AV node myocytes (**Figure 1M,** top panels). HCN channels carry I_f, an inward current flowing during diastole that constitutes an important mechanism for phase 4 depolarization and pacemaking.[33] The role of I_f in conduction through the AV node is underappreciated, although several studies suggest that it is involved[34-39] (explored further in the **Discussion**). Intriguingly, image analysis of HCN4 immunolabelled images revealed a reduction in HCN4 protein expression in the compact node of trained (n=7) *versus* sedentary (n=7) horses (**Figure 1M, top panels, and Figure 1N**). The reduction of HCN4 in the trained compact node was confirmed by western blot in biopsies of the compact node from sedentary (n=5) and trained (n=5) horses. A representative blot is shown in **Figure 1O** (top panel). HCN4 protein expression (top band) was normalised to total protein expression (**Figure 1O, lower panel**) and is plotted in **Figure 1P** – there was a reduction in normalised HCN4 band intensity in AV node biopsies from trained *versus* sedentary horses.

The inward current carrying L-type Ca^{2+} channels are known to play a major role in AV node diastolic depolarization, setting excitability and the upstroke of the action potential. $Ca_v1.2$ and $Ca_v1.3$ are important Ca^{2+} channels in the heart and their knockout has been reported to slow or block AV node conduction.[36, 38, 40] Here we investigated protein expression of the key L-type Ca^{2+} channel subunit $Ca_v1.2$ (commercially sourced antibodies against $Ca_v1.3$ lacked specificity and could not be validated in horse tissue). Akin to HCN4, we observed a significant reduction in signal intensity of $Ca_v1.2$ immunolabelling in trained (n=7) *versus* sedentary (n=7) horses (**Figure 1M, bottom panels, Figure 1Q**). Qualitatively similar data were obtained by western blot; the normalised band intensity for $Ca_V1.2$ was reduced in compact node biopsies from trained horses (n=5) compared to sedentary (n=5) horses (**Figure 1R,S**).

Taken together, these data are the first demonstration of *intrinsic* electrical remodelling of the AV node in a large animal model of the athlete's heart and this directly contravenes the commonly accepted mechanisms of high vagal tone or idiopathic fibrosis as primary drivers of training-induced AV node dysfunction.

Swim training in mice induces AV node dysfunction with widespread transcriptional remodelling of ion channels.

Training-induced dysfunction of the AV node was explored further in mice. Mice were swim trained for 20 weeks to recapitulate approximately 10 years of exercise in humans.[41, 42] As expected, at the end of the training period, trained mice (n=15) presented with sinus bradycardia, mild left ventricle hypertrophy evidenced by echocardiography (**Online Table I**) and a significant prolongation of the PR interval (**Figure 2A**) compared to sedentary mice (n=15). Involvement of the autonomic nervous system in mediating training-induced PR interval prolongation was tested by blocking cardiac muscarinic and β receptors (using 1 mg/kg atropine and 1 mg/kg propranolol - justification of doses given by D'Souza *et al.*[43]); as observed in horses (**Figure 1K)**, the PR prolongation in trained animals persisted after complete block of the autonomic nervous system (**Figure 2A**) once again suggesting intrinsic training-induced remodelling of the AV node.

To determine how prolonged exercise training impacts AV node conduction, we performed an *in vivo* electrophysiological study to specifically determine: (i) the pacing cycle length at which Wenckebach conduction occurred and (ii) the AV node effective refractory period. **Figure 2B** shows that the Wenckebach cycle length and the AV node effective refractory period were significantly prolonged in trained mice compared to sedentary mice, further evidence of training-induced impairment of AV node conduction. Recordings obtained during *in vivo* programmed electrical stimulation demonstrating AV Wenckebach block in trained and sedentary mice are shown in **Figure 2C**. There was a

progressive PR prolongation prior to AV block, which developed at a longer cycle length in trained mice (106 ms) compared to sedentary mice (74 ms). Additionally, and consistent with our previous findings, we also observed sinus bradycardia and an increased sinus node recovery time in trained mice compared to sedentary mice (**Online Figure II**). To determine whether longer PR intervals in trained mice were related to the underlying reduction in heart rate, the PR interval was measured under constant pacing cycle lengths of 100 and 120 ms. As given in **Figure 2D**, trained animals still presented with a significantly longer PR interval *versus* sedentary animals under these conditions.

The AV node is supported *in vivo* by neurohumoral influences, and, therefore, experiments were conducted on isolated denervated right atrial preparations encompassing the AV node (**Figure 2E**). From extracellular potential recordings and consistent with **Online Figure II** we confirmed a prolonged sinus node cycle length in trained mouse preparations (**Figure 2F**). Importantly, as given in the representative trace in **Figure 2G** (left panel)**,** trained mice (n=7) had a significantly prolonged atrial-His (A-H) interval compared to sedentary mice (n=8) that was also apparent under a fixed pacing cycle length of 150 ms (**Figure 2G**, right panel). There was also a tendency towards prolongation of the AVERP (trained, 123.7 ± 12.5 ms; sedentary, 110.8 ± 8.8 ms; n=6/6), Wenckebach cycle length (trained, 146.5 ± 12.4 ms; sedentary, 132.8 ± 7.2 ms; n=4/4), and the H-V interval at a fixed pacing cycle length of 150 ms (trained, 19.69 ± 2.02 ms; sedentary, 18.75 ± 0.75 ms) in the isolated AV node, but these parameters did not reach statistical significance (data not shown). Cumulatively, these studies support a role for intrinsic training-induced adaptations to the AV node.

To understand the mechanisms underlying training-induced AV block, we assessed transcriptional changes in key ion channels, connexins, intracellular Ca^{2+}-handling proteins, ion transporters and extracellular matrix components and mediators that are known to be involved in AV node impulse generation and conduction. Transcriptional

profiling of the mouse AV node presents special challenges because of its small size, and the interdigitation of AV node myocytes with the extracellular matrix and 'working' myocytes of the atrial and ventricular septae. To obtain an accurate sample of the AV node, right atrial preparations (representative example given in **Figure 2H**) were first cryosectioned and stained with Masson's trichrome for histological identification of the AV conduction axis (**Figure 2H**). This was followed by immunofluorescent labelling of relevant regions with an anti-HCN4 antibody (**Figure 2H, lower panel**) that guided laser-capture microdissection of HCN4-positive AV node regions such as the compact node (**Figure 2H, inset**).

AV node regions were then processed for medium throughput qPCR assessment of 96 key AV node transcripts using TaqMan Low Density Array Cards. Six reference transcripts were assessed (*Hprt*, *Pgk1, Tbp, Ipo8, Gapdh and 18s* tested) and *Hprt* and *Pgk1* determined to be the optimal combination for normalisation based on stability scores determined by the algorithm GeNorm[44] (**Online Figure III**). Differential expression testing using the non-parametric Limma test followed by Benjamini-Hochberg False Discovery Rate correction set at 5% demonstrated a widespread downregulation of mRNAs for Ca^{2+} channels, intracellular Ca^{2+}-handling molecules, HCN channels, K^+ channels and connexins in the AV node of trained mice (**Figure 2I)**. Na^+ channels, components of the Na^+–K^+ pump and components of the extracellular matrix (**Online Figure IE**) were also reduced by training (**Online Table II and III)**. Remarkably, training-induced remodelling appeared to be restricted to the AV node as none of the transcripts assessed were significantly altered in corresponding right atrial tissue collected by laser capture microdissection from sedentary and trained animals (**Online Figure IV**).

As an aside, pilot studies of Masson's trichrome stained AV conduction axis (n=3 mice per group) indicated unchanged collagen deposition between groups (**Online Figure IC-D**). These data combined with the transcript downregulation in the major

fibrillar collagens (**Online Figure I**) meant that the possibility of a training-induced increase in extracellular matrix deposition was not pursued further as a contributor to AV node dysfunction in mice.

Role for $I_{Ca,L}$, I_f and I_K downregulation in training-induced AV node dysfunction

To decipher how training-induced transcriptional dysregulation of ion channels translates into slowed AV node conduction, protein expression of key dysregulated transcripts was assessed using immunohistochemistry or western blot, techniques limited by the specificity of commercially sourced antibodies. Connexins are responsible for electrical coupling between myocytes and therefore are an important determinant of the conduction velocity of the action potential. Protein levels of connexin 40[45, 46] and connexin 45,[47] previously shown to affect AV node conduction, were tested by immunohistochemistry and western blot respectively and found to be unchanged by training status (**Online Figure V**).

$I_{Ca,T}$, carried in large part by the $Ca_V3.1$ channel in the adult AV node, is a known contributor to the diastolic pacemaker current.[35] However, protein levels of $Ca_V3.1$ were not significantly altered in the trained AV node (**Online Figure V).** Contrastingly, in the case of $Ca_V1.2$, consistent with reduced mRNA levels, there was a significant downregulation of protein in the compact node of trained mice (n=7) *versus* sedentary mice (n=6) (**Figure 3A**). In all preparations the anti-$Ca_V1.2$ antibody produced the classical membrane labelling pattern that was prominent in sedentary animals (**Figure 3A**, top left panel, white arrows). In trained animals the labelling was faint, diffused and frequently absent (**Figure 3A**, top right panel, white arrows). Aggregates of non-specific artefactual labelling were evident in all mouse preparations (**Figure 3A**, top panels, blue arrows) and fluorescence intensity measurements from these structures were excluded from the analysis (see Online Supplemental Methods for further details). A qualitative

reduction in $Ca_V1.2$ protein was also evident from subsequent western blot analysis (cf. **Figure 7F**).

To test directly whether reduced $Ca_V1.2$ expression has consequences for $I_{Ca,L}$, AV node cells were isolated from sedentary and trained animals by enzymatic dispersion and were analysed by patch-clamp in the whole-cell configuration. The density of $I_{Ca,L}$ was recorded in AV node cells from sedentary (n=8 cells from 8 mice) and trained (n=9 cells from 9 mice) mice. Currents recorded in the range −55 to 20 mV were normalised to cell capacitance to obtain current density. The mean cell capacitance was 26.7 pF (n=22) and 27.5 pF (n=24) in sedentary and trained mice, respectively (not significantly different, Student's *t*-test, P>0.05). In **Figure 3B** sample current traces and mean current–voltage (IV) relationships are shown. The $I_{Ca,L}$ density was reduced in trained mice by 30% at the peak value (0 mV).

As a role of I_f in AV node conduction is becoming increasingly evident (see **Discussion**) and we have previously demonstrated a role for I_f remodelling in the trained sinus node,[24, 25] next we investigated the downstream consequences of HCN4 transcriptional remodelling in the AV node. Immunolabelling revealed a significant downregulation of HCN4 protein in trained mice (n=6) *versus* sedentary mice (n=6), especially evident in the penetrating portion of the His bundle (**Figure 3C**). As expected, this was accompanied by a reduction in I_f over a wide potential range in isolated AV node myocytes from trained mice (n=9 cells from 9 mice) compared to sedentary mice (n=8 cells from 8 mice) (**Figure 3D**). Given these findings, the role of I_f in AV node conduction was further assessed *in vivo* by blocking I_f by administration of ivabradine (S16257-2; 6 mg kg^{-1}), which dose-dependently reduces heart rate in humans[48] and animals.[49] Absolute PR intervals before and after block of I_f in anaesthetised mice are shown in **Online Figure VI.** Intriguingly, block of I_f abolished the difference in PR interval in trained (n=7) *versus* sedentary (n=7) mice, consistent with a training-induced

downregulation in HCN channels being involved with or responsible for the difference, and further evidence for an important functional role for I_f in AV conduction.

Next, the functional consequences of the change in expression of mRNAs coding for K^+ channels presented in **Figure 2I** were assessed by patch clamp experiments in a separate cohort of swim-trained animals (n=5) and sedentary control (n=5) animals. A well-known K^+ current in the mouse heart is the rapid delayed rectifier K^+ current $I_{K,r}$ carried by the ERG1 channel. $I_{K,r}$ was recorded in AV node cells during and after depolarizing voltage clamp pulses as E-4031-sensitive current (E-4031 is a specific blocker of $I_{K,r}$). Typical current recordings from AV node cells isolated from sedentary and exercise trained mice are shown in **Figure 4A**. Under control conditions, currents were smaller in exercise trained mice (**Figure 4A**). 1 μM E-4031 was then applied to block $I_{K,r}$. E-4031 blocked some but not all current during the depolarizing pulses and **Figure 4A** shows both the E-41031-insensitive and -sensitive currents. Whereas ERG is responsible for the E-41031-sensitive current, other K^+ channels are presumably responsible for the E-41031-insensitive current; both currents were smaller in exercise-trained mice (**Figure 4A**). Mean data are shown as IV relationships in **Figure 4B,C**. Current at the end of the depolarizing pulses (**Figure 4B**) and the peak tail current after the pulses (**Figure 4C**) was measured. Because $I_{K,r}$ is inactivated during depolarizing pulses (following activation) and this inactivation is rapidly removed on repolarization after the pulses, tail current is arguably the better measure of $I_{K,r}$. **Figure 4B,C** shows current under control conditions as well as the E-4031-insensitive and sensitive currents and **Figure 4D,E** compares E-4031-insensitive and sensitive currents in sedentary and exercise trained mice. Both are smaller in exercise trained mice. The best measure of $I_{K,r}$ (E-4031-sensitive tail current in **Figure 4E**) suggests that $I_{K,r}$ is reduced by ~50% in exercise trained mice and this is consistent with the apparent trend towards downregulation of ERG mRNA (**Figure 2I**). However the difference did not reach statistical significance. Another well-known K^+ current in the heart

is the transient outward K^+ current. It was measured in AV node cells as the 10 μM 4-AP-sensitive current during depolarizing pulses, but the current was undetectable both in sedentary and exercise trained mice (data not shown).

Training-induced reduction in spontaneous firing of isolated AV node myocytes

The combined impact of training-induced reductions in $I_{Ca,L}$ (**Figure 3B)** I_f (**Figure 3D)** and I_K (**Figure 4**) on the spontaneous action potential were tested in AV node myocytes isolated from sedentary and trained animals. Representative recordings from n=5 sedentary mice and n=5 trained mice are shown in **Figure 5A (**left panel) and a sample segment of an action potential recording with time- and voltage-hallmarks used for analysis is given in the right panel. As given in **Figure 5B**, the spontaneous beating rate of isolated AV node myocytes isolated from trained mice was significantly lower than that of sedentary mice, consistent with a reduction in $I_{Ca,L}$ and I_f (**Figure 3B,D)**. Accordingly, the slope of both the linear and exponential phases of diastolic depolarization (SLDD and SEDD) was also significantly reduced in myocytes isolated from trained animals (Figure 5B). There were no discernible differences in the maximum diastolic potential, and action potential threshold, upstroke velocity, amplitude and duration (**Figure 5B)**. The predominant training-induced change to the action potential was the slowing of diastolic depolarization and a longer cycle length - likely explained by $I_{Ca,L}$ and I_f reduction. As the observed changes in I_K did not impact the maximum diastolic potential or action potential duration in trained *versus* sedentary AV node myocytes (**Figure 5B**) and previous studies in mice failed to observe alteration of the PR interval on $I_{K,r}$ suppression with ERG silencing[50] or dofetilide treatment[51] the study then focused on the training-induced reduction in $I_{Ca,L}$ and $I_{f.}$ To test whether the changes in $I_{Ca,L}$ and I_f density could account for training-induced slowing of conduction through the AV node, the observed changes in $I_{Ca,L}$ and I_f density (**Figure 3B,D**) were incorporated into a one-dimensional computational

model of the AV node (**Figure 5C**). To simulate the effect of athletic training, the conductance of I_f in the model was reduced by 60% and the conductance of $I_{Ca,L}$ in the model was reduced by 40%. The simulated I-V relationships of $I_{Ca,L}$ and I_f are shown in right panels in **Figure 5C**. The model predicted a 25% reduction in the conduction velocity of the trained AV node action potential (7.1 cm/s) relative to the sedentary one (9.5 cm/s, **Figure 5C, left panel**).

From these combined *in vivo* (**Figure 2A-D, Online Figure VI**)*, ex vivo* (**Figures 2E-I**, **3, 4 and 5A,B**) and *in silico* (**Figure 5C**) approaches it is concluded that ion channel remodelling of the trained AV node is a primary mechanism underlying first degree AV block in swim-trained mice.

Mechanisms controlling transcriptional remodelling of $Ca_V1.2$ and HCN4 in the trained AV node

What regulates the transcriptional response of the trained AV node, in particular of $Ca_V1.2$ and HCN4? Our previous work has demonstrated that, in the trained sinus node, interplay of miR-423-5p and the transcription factor NKX2.5 controls mRNA expression of HCN4 and sinus bradycardia.[24] Here we investigated, for the first time, the involvement of miRs as potential regulators of ion channel transcription within the AV node. Expression of 750 rodent miRs (and 6 reference transcripts) in the AV node was determined using a TaqMan Array system. Among the 750 miRs measured, 33 miRs were differentially expressed between sedentary (n=7) and trained (n=8) mice, given by the red circles in **Figure 6A** (values given in **Online Table IV**). Interestingly, only 2 out of 31 differentially expressed miRs were downregulated whereas the rest were upregulated by training (**Figure 6A,** red circles). These data are indicative of a repressive miR signature - a potential explanation for the diffuse training-induced downregulation of key pacemaking transcripts observed in **Figure 2I**. As 3′ untranslated region (3′UTR) targeting is acknowledged to be a primary method of miR-based gene silencing,[52] significantly

dysregulated miRs were screened by a dual luciferase assay to identify miRs that directly target the 3′ untranslated region (3′UTR) of *$Ca_V1.2$* (**Figure 6B)** *and HCN4 (***Figure 6C).** In this experiment recombinant plasmids in which a luciferase coding sequence was cloned downstream of the **(i)** $Ca_V1.2$ 3′UTR (split into three contiguous constructs A-C), **(ii)** HCN4 3′UTR and **(iii)** control vector without a 3′UTR (control) were co-transfected individually with 33 (differentially regulated) individual miRs in H9C2 cells. Firefly luciferase was measured and normalised to Renilla luciferase in duplicate experiments in independent batches of cells (**Figure 6B,C**). Based on this initial screen, many of the dysregulated miRs tested appeared to suppress luciferase activity linked to the $Ca_V1.2$ and HCN4 3′UTRs relative to control. However, of the 33 miRs tested, 14 miRs significantly decreased luciferase activity linked to the $Ca_V1.2$ 3′UTR whereas five decreased the luciferase activity linked to the HCN4 3′UTR. Of these miRs, miR-215-5p, miR-211-5p, miR-335-3p, miR-380-5p, miR-1959 and miR-432 were selected for further study as: **(i)** they showed the most obviously inhibitory effects, i.e. >40% reduction in the normalised luciferase signal *versus* control and **(ii)** based on computational predictions by the algorithms Targetscan,[53] RNA22[54] and Sfold,[55] consensus binding sites for these miRs were identified in the 3′UTR of $Ca_V1.2$ and HCN4 (**Online Figure VII)**. The effect of overexpression of these miRs on the $Ca_V1.2$/HCN4 3′UTR linked luciferase expression (**Online Figure VIIA-B,** based on an n=5 replicates in independent batches of cells) demonstrated that miR-215-5p, miR-211, miR-1959 and miR-432 repress the expression of an exogenous reporter gene with a $Ca_V1.2$ 3′UTR (**Online Figure VIIA**) whereas miR-211-5p and miR-432 repress HCN4 3′UTR reporter expression (**Online Figure VIIB**).

A series of *in vitro* experiments were conducted to select miRs for *in vivo* targeting: first, site directed mutagenesis was conducted to verify specificity of predicted miR binding sites on the 3′UTR of $Ca_V1.2$ and HCN4 (wild-type and mutated sequences given in **Online Figure VIID**). In this experiment wild type and mutated 3′UTR sequences were co-

transfected separately with selected miRs and compared to a control vector without a 3′UTR (control). Firefly luciferase was measured and normalised to Renilla luciferase in duplicate experiments in independent batches of cells. Of all miRs tested, only mutations in the binding sequence for miR-211-5p rescued the reduction in the bioluminescent signal for $Ca_V1.2$ (**Figure 6D**), revealing a potential direct binding region for $Ca_v1.2$ targeting by this miR. In the case of HCN4 (**Figure 6E**), mutations in predicted binding sites for miR-211-5p and miR-432 but not miR-335-3p rescued the reduction in the bioluminescent signal for HCN4 indicating two direct binding sites.

Having identified and confirmed functional bindings sites for miR-211-5p and miR-432 we tested whether endogenous $Ca_V1.2$/HCN4 expression can be modulated by these miRs. As primary AV node myocytes are not amenable to cell culture, we used embryonic stem-cell (ES) derived myocytes that natively express $Ca_V1.2$ and HCN4 transcripts.[56] Parallel studies confirmed superior recruitment of HCN4 transcriptional machinery in these cells compared to other relevant cellular systems (HL-1 and neonatal rat ventricular cardiomyocytes tested; data not shown). miR mimics corresponding to miR-211-5p or miR-432 were introduced into embryonic stem cell-derived myocytes and overexpression after 24 h confirmed by qPCR. HCN4 transcript expression was suppressed by both miRs whereas $Ca_v1.2$ mRNA levels were only reduced by miR-211-5p overexpression (**Figure 6F**). Protein expression of HCN4 was also reduced by miR-432 overexpression (**Online Figure VIII**); western blotting for $Ca_V1.2$ protein was technically unfeasible due to diffuse non-specific antibody binding. Nevertheless, based on the combined approaches described above it is concluded that miR-211-5p (increased by 8-fold in the trained AV node) and miR-432 (increased by 70-fold in the trained AV node) are likely transcriptional regulators of $Ca_v1.2$ and HCN4 expression. Interestingly, these miRs demonstrated a trend towards upregulation in AV node biopsies from trained horses (n=5) compared to sedentary horses (n=5) (**Online Figure IX**).

Reversibility of training-induced AV node remodelling with anti-miRs or detraining

In pilot investigations, the impact of combined inhibition of miR-432 and miR-211-5p on training-induced PR interval prolongation was assessed in mice. The prolongation in the PR interval was evident by 21 days of swim-training, and at this time point, miRs were knocked down *in vivo* in swim trained mice (n=6) via 3 systemic (intraperitoneal) injections of 25 mg/kg body weight cholesterol-conjugated antisense oligonucleotides (antimiRs). AntimiR 211-5p and antimiR-432 were custom designed to include a 2′-O-methyl (2′-OMe) backbone linked by phosphodiester and phosphothiorate bonds conjugated to a 5′ cholesterol group. These chemical modifications have been recently optimised to give superior potency, efficacy and *in vivo* stability for miR targeting in the heart, resulting in a dramatic suppression of miRs one-week post administration.[57] Littermate cohorts of sedentary (n=6) and trained mice (n=6) received an equivalent dose of control antimiR (oligonucelotides against *C. elegans* miR-39-5p that do not target mammalian sequences[58]). AntimiRs treatment did not impact overt health status or ability of animals to complete the training regimen. One week after the first administration (Day 28), a significant reduction in AV node levels of miR-432 in antimiR-treated animals was confirmed by qPCR; however, only modest suppression of miR-211-5p was achieved (**Figure 7A**). Unexpectedly, as given in **Figure 7B,** swim-trained mice that received antimiRs presented with a significant reduction in heart rate compared to swim-trained and sedentary mice that received control antimiRs. Despite this reduction in heart rate, trained mice that received the antimiRs did not develop a training induced prolongation of the PR interval observed in trained mice that received control antimiR (**Figure 7C**). To dissociate changes in the PR interval from the alterations to baseline heart rate, the PR interval was measured during fixed S1-S1 pacing starting at 120 ms. At this cycle length, trained animals receiving control antimiR demonstrated Wenckebach conduction. Therefore S1-S1 pacing at 130 ms was attempted. **Figure 7D** shows that at a fixed pacing cycle length

of 130 ms, the PR interval was longer in trained animals and that this effect was abolished by antimiRs targeting $Ca_V1.2$ and HCN4. Representative recordings obtained during *in vivo* programmed electrical stimulation demonstrating the effect of systemic antimiRs suppression on the PR interval under fixed S1S1 pacing are given in **Figure 7E**. To test whether reversal of PR prolongation in the antimiRs-treated trained animals was accompanied by a restoration of $Ca_V1.2$ and HCN4 to pretraining levels, AV node biopsies (n=3/group/protein) were harvested for western blotting. As shown by representative western blots (**Figure 7F,G**), there was a reduction in $Ca_V1.2$ (**Figure 7F,** right panel) and especially HCN4 levels (**Figure 7G,** right panel) in the trained AV node accompanied by restoration in the antimiRs-treated group. In both cases there was a heterogeneity in the individual response to antimiR treatment but this was not investigated further. Nevertheless, in both instances there was no longer a significant difference in the expression levels of $Ca_V1.2$ and HCN4 between sedentary animals and trained animals receiving antimiRs. Finally, the impact of detraining was investigated. As given in **Figure 7H,I**, 12 weeks of detraining restored training-induced sinus bradycardia and PR prolongation *in vivo*. Intriguingly, only HCN4 expression was de-repressed in detrained animals (**Figure 7K**); the reduction in $Ca_V1.2$ persisted (**Figure 7J**). It is concluded that either miR suppression or detraining rescues training-induced AV node dysfunction by (at least) partial reversal of electrical remodelling.

DISCUSSION

This study shows that dysfunction of the AV node in response to sustained endurance exercise cannot be fully attributed to changes in autonomic tone as commonly accepted, and is likely to be due in part to transcriptional remodelling of ion channels. Based on data collected in two animal models of endurance exercise, we ascribe particular importance to a downregulation of $Ca_V1.2$ and HCN4 and a consequent decrease in the density of $I_{Ca,L}$ and I_f as a new molecular mechanism underlying AV block in athletes.

We also identify miR-211-5p and miR-432 as potential new regulators of electrical remodelling within the trained AV node.

Horse as a high-fidelity model for training-induced rhythm disturbances

To our knowledge, this is the first exploration of training-induced arrhythmia in a large animal model. To date, all studies concerning the effect of long-term exercise on cardiac function have been conducted in human athletes (primarily in non-invasive studies) or, when mechanisms such as fibrosis, inflammation and vagal influence are studied, in rodents.[24, 25, 41, 42, 59] The cardiac adaptation to long-term physical training in racehorses is identical to the changes observed in human athletes leading to the development of comparable phenotypic characteristics of the 'Athlete's Heart' such as ventricular hypertrophy, and reduced fractional shortening and diastolic function after exercise.[26, 27, 60] Sinus arrhythmia, sinus node exit block, wandering pacemaker, and AV block have been reported in horses.[61] Remarkably, second-degree AV block is the most common arrhythmia, reported to occur in up to 40% of horses.[61] These characteristics make the racehorse uniquely suited for modelling the effect of sustained exercise on the cardiac conduction system. Correlations between detraining time, the heart rate and PR interval were studied (**Figure 1H-I**). Exponential analysis showed that the rate of reversibility of sinus node remodelling (τ = 10.3 months) was slower than that of AV node remodelling (PR interval, τ = 2.5 months). Literature on reversibility of AV node dysfunction in human athletes is sparse but our findings in both racehorses (**Figure 1H**) and in mice (**Figure 7I**) corroborate a recent study reporting that prolongation of the PR interval induced by 12 weeks of moderate-intensity aerobic exercise in postmenopausal women was lost after five months of detraining.[62]

Role of intrinsic *versus* autonomic mechanisms underlying AV block in athletes

Autonomic innervation of the AV junction modulates conduction of the action potential, the sympathetic nerves facilitating and parasympathetic nerves impeding conduction. On the

basis of heart rate variability measurements, AV block in athletes is currently attributed to increased vagal tone,[22] even though many studies in humans and animal models show no evidence of high vagal tone (reviewed by D'Souza and Boyett[23, 63, 64]). Furthermore, our recent work has shown from an analysis of the underlying biophysics of pacemaking that heart rate variability is primarily determined (in an exponential-like manner) by heart rate, and the increase in heart rate variability in athletes is attributed to the resting bradycardia rather than any increase in vagal tone.[65] The results of this study add further weight to the evidence against high vagal tone in training-induced AV node dysfunction. In horses (**Figure 1K**) and mice (**Figure 2A**), the PR interval was prolonged in the trained animals both under baseline conditions and after administration of atropine and propranolol to block the autonomic nervous system. These data corroborate previous observations in human athletes by Stein *et al.*[10] in which the Wenckebach cycle length and anterograde AVERP were prolonged in athletes, regardless of the presence of autonomic blockade. Similarly, in a study investigating second-degree AV block in horses, Yamaya *et al.*[66] reported that slower AV conduction, prolonged Wenckebach conduction and higher refractoriness in horses with AV block (*versus* horses without AV block) was still maintained under complete autonomic block. Furthermore, experiments in the isolated, denervated mouse AV node demonstrated that conduction slowing was intrinsic to the node (**Figure 2G**), further reiterated in the observed slowing of the spontaneous cycle length in isolated AV node myocytes from trained *versus* sedentary mice (**Figure 5A-B**). From all these lines of evidence - ranging from the intact animal(s) to the isolated myocyte - we propose a predominant role for intrinsic electrical remodelling of the AV node in explaining first-degree AV block in athletes.

Ion channel remodelling in the trained AV node

This study presents for the first time a comprehensive transcriptional and electrophysiological analysis of the known key players underlying action potential

generation and conduction in the mouse AV node and its dysregulation in the setting of prolonged exercise training (**Figure 2I; Online Table II**). To avoid contamination of the AV node tissue samples by the neighbouring atrial and connective tissues, laser capture microdissection (**Figure 2H**) was used; our AV node transcriptional profile provides a benchmark for other investigators studying mouse AV node physiology and transcriptional remodelling. The striking and selective downregulation of ion channel and related transcripts in the AV node but not in the surrounding right atrial muscle (**Online Figure IV**), led us to investigate the role of miRs in this process, given their capacity to regulate the levels of multiple genes simultaneously. Accordingly, in this study we demonstrate, for the first time, that AV node ion channels are under the control of the miR network. As primary mouse AV node myocytes are not amenable to culture, mouse ES-derived myocytes that natively express $Ca_V1.2$ and HCN4 transcripts were used in this study as an intermediate step in the selection of miRs for *in vivo* targeting (based on the efficacy of miR-mediated knockdown). However, under standard culture conditions these cells appeared quiescent, precluding the assessment of miR-mediated electrophysiological alterations. Nevertheless, we identified and validated direct binding regions for miR-211-5p/miR-432 mediated targeting of $Ca_V1.2$ and HCN4 (**Figure 6**) and on the basis of these findings tested the therapeutic efficacy of targeting noncoding miRs to rescue AV node dysfunction *in vivo*. Our study provides first proof-of-concept that *in vivo* suppression of miR-211-5p and miR-432 rescues the training induced prolongation of the PR interval with restoration of HCN4 protein to pre-training levels (**Figure 7**). However, given the unexplained preferential suppression of miR-432 *versus* miR-211-5p and a lower heart rate in antimiRs-treated animals in this pilot miR study, we conclude that major challenges of specificity and delivery remain for development of oligonucleotide-based therapeutics for AV block. Adeno-associated virus-based antimiRs gene delivery engineered to enhance transduction specificity to nodal myocytes holds promise in this regard.

In this work we report that endurance exercise in mice results in diminished $I_{Ca,L}$, I_f and I_K density. In particular, we associate remodelling of the inward currents, $I_{Ca,L}$ and I_f, with the decrease in the spontaneous rate and slowed diastolic depolarisation seen in isolated AV node myocytes from trained *versus* sedentary mice (**Figure 5A-B**).

While this study is the first to associate $Ca_V1.2$ downregulation (and consequently $I_{Ca,L}$ downregulation) with exercise-induced AV block (**Figure 3A-B**), the relationship between AV block and L-type Ca^{2+} channel remodelling is not new and has been demonstrated in both acquired and inherited pathological states. For example, mutations in the L-type Ca^{2+} channel have been identified in humans with syndromic AV block[67] and congenital AV block has been associated with maternal antibodies targeting the L-type Ca^{2+} channel in infants.[68] We have previously reported that downregulation of L-type Ca^{2+} channels contributes to AV node dysfunction following pulmonary hypertension.[38] Given the role of $I_{Ca,L}$ in underlying the slow phase 0 upstroke of the action potential in the slow conducting pathway of the AV node,[30] these findings are expected. A number of commercially available antibodies were tested to assess $Ca_V1.2$ remodelling in mice – all of which produced labelling artefact that could be excluded by automated image analysis from immunolabelling. Future mass spectrometry-based analysis may be required to arrive at a definitive conclusion but the small size (~30 µg of protein/mouse AV node) precluded this assessment in the present study. Nevertheless, the overall trend in $Ca_V1.2$ downregulation remained consistent between techniques, experiments and species (**Figures 1R-S, 3A** and **7F**).

In contrast to $I_{Ca,L}$, the link between I_f downregulation (**Figure 3C-D**) and AV block is less well established. HCN channels and I_f have mainly been considered in relation to sinus node pacemaking, but there is now substantial evidence that I_f may play a significant role in AV node conduction: The results of this study (**Online Table II**) and others from our laboratory[37, 38] have demonstrated high levels of HCN4 in the AV node. HCN4 mutations

have been associated with AV block in humans[69] and, in the same vein, Baruscotti *et al*.[34] demonstrated that inducible cardiac-specific knockout of HCN4 in mice is lethal because of the development of complete AV block. Consistent with the work by Baruscotti *et al*.,[34] it has been shown that mice carrying conditional time-controlled and heart specific genetic silencing of I_f present with a high incidence of type 1 and 2 second-degree AV block, an observation which correlates with strong reduction of automaticity of AV node myocytes recorded in this model.[39] In addition, PR prolongation induced by the I_f blocker ivabradine (**Online Figure VI**) observed in this study is in agreement with previous mouse studies in which I_f block reduced AV node automaticity.[36, 39, 70] Similarly, the I_f blocking agent, zatebradine, has been shown to increase the A-H interval, AVERP, and Wenckebach cycle length in humans.[71] We have also recently shown that in young rats, I_f block significantly prolongs the A-H interval, AVERP and Wenckebach cycle length.[37] We posit that downregulation of I_f may slow AV node conduction by decreasing cell excitability. In this work, reversal of HCN4 but not $Ca_V1.2$ transcriptional remodelling with detraining (**Figure 7J-K**) coupled with the findings that acute I_f block abolishes training-induced PR prolongation (**Online Figure VI**) suggest that HCN remodelling may be the predominant effector of AV block in trained mice. Detailed pharmacological dissection of the individual contribution of these channels towards the observed phenotype was not within the study aims but merits further investigation.

Concluding remarks

In conclusion, this study has uncovered fundamental ionic and transcriptional changes that set the electrophysiological milieu of the trained AV node. These findings provide new insight into the molecular mechanisms underlying a common rhythm disturbance in athletes. Follow-on studies investigating AV node-specific delivery of miR-211-5p and miR-432 may be an important first step towards the development of small molecule therapies for AV block seen in some veteran athletes.

SOURCES OF FUNDING

Work supported by a British Heart Foundation Intermediate Basic Science Research Fellowship to AD (FS/19/1/34035) and British Heart Foundation grants to MRB and AD (PG/14/24/30626, RG/11/18/29257, PG/13/99/30233). Work within the IGF research group was funded by the LabEx “Ion Channel Science and Therapeutics” supported by a grant from ANR (ANR-11-LABX-0015), the *Fondation pour la Recherche Medicale* "Physiopathologie Cardiovasculaire" (DPC20171138970 to M.E.M.), the *Agence Nationale de Recherche* (ANR-15-CE14-0004-01 to M.E.M) and the *Fondation Leducq* TNE FANTASY (19CV03 to MEM and MRB). JSPS KAKENHI (JP18K15017), the Naito Foundation (Grant for Studying Overseas 2014) and the Nakatomi Foundation (Research Grant for Study Oversea 2014) also supported this study (SN).

ACKNOWLEDGMENTS

The IGF group thanks the Réseau d’Animaleries de Montpellier (RAM) of Biocampus facility for the management of mouse lines. We thank all the personnel of the PCEA mouse breeding facility in Montpellier and of the iExplore platform for help in managing the training regimen of mice.

DISCLOSURES

None

LIST OF SUPPLEMENTAL MATERIALS

1. Expanded Materials and Methods
2. Online Tables I - IV
3. Online Figures I – IX
4. References 72-79

REFERENCES

1. Andersen K, Farahmand B, Ahlbom A, Held C, Ljunghall S, Michaelsson K, Sundstrom J. Risk of arrhythmias in 52 755 long-distance cross-country skiers: A cohort study. *Eur Heart J*. 2013;34:3624-3631
2. Calvo N, Ramos P, Montserrat S, Guasch E, Coll-Vinent B, Domenech M, Bisbal F, Hevia S, Vidorreta S, Borras R, Falces C, Embid C, Montserrat JM, Berruezo A, Coca A, Sitges M, Brugada J, Mont L. Emerging risk factors and the dose-response relationship between physical activity and lone atrial fibrillation: A prospective case-control study. *EP Europace*. 2016;18:57-63
3. Karjalainen J, Kujala UM, Kaprio J, Sarna S, Viitasalo M. Lone atrial fibrillation in vigorously exercising middle aged men: Case-control study. *BMJ*. 1998;316:1784-1785

4. Mont L, Sambola A, Brugada J, Vacca M, Marrugat J, Elosua R, Pare C, Azqueta M, Sanz G. Long-lasting sport practice and lone atrial fibrillation. *Eur Heart J*. 2002;23:477-482
5. Myrstad M, Nystad W, Graff-Iversen S, Thelle DS, Stigum H, Aaronaes M, Ranhoff AH. Effect of years of endurance exercise on risk of atrial fibrillation and atrial flutter. *Am J Cardiol*. 2014;114:1229-1233
6. Baldesberger S, Bauersfeld U, Candinas R, Seifert B, Zuber M, Ritter M, Jenni R, Oechslin E, Luthi P, Scharf C, Marti B, Attenhofer Jost CH. Sinus node disease and arrhythmias in the long-term follow-up of former professional cyclists. *Eur Heart J*. 2008;29:71-78
7. Northcote RJ, Canning GP, Ballantyne D. Electrocardiographic findings in male veteran endurance athletes. *Br Heart J*. 1989;61:155-160
8. Northcote RJ, Rankin AC, Scullion R, Logan W. Is severe bradycardia in veteran athletes an indication for a permanent pacemaker? *Br Med J*. 1989;298:231-232
9. Senturk T, Xu H, Puppala K, Krishnan B, Sakaguchi S, Chen LY, Karim R, Dickinson O, Benditt DG. Cardiac pauses in competitive athletes: A systematic review examining the basis of current practice recommendations. *EP Europace*. 2016;18:1873-1879
10. Stein R, Medeiros CM, Rosito GA, Zimerman LI, Ribeiro JP. Intrinsic sinus and atrioventricular node electrophysiologic adaptations in endurance athletes. *J Am Coll Cardiol*. 2002;39:1033-1038
11. Viitasalo MT, Kala R, Eisalo A. Ambulatory electrocardiographic recording in endurance athletes. *Br Heart J*. 1982;47:213-220
12. Crouse SF, Meade T, Hansen BE, Green JS, Martin SE. Electrocardiograms of collegiate football athletes. *Clin Cardiol*. 2009;32:37-42
13. Hoogsteen J, Bennekers JH, van der Wall EE, van Hemel NM, Wilde AA, Crijns HJ, Gorgels AP, Smeets JL, Hauer RN, Jordaens JL, Schalij MJ. Recommendations and cardiological evaluation of athletes with arrhythmias: Part 1. *Neth Heart J*. 2004;12:157-164
14. Talan DA, Bauernfeind RA, Ashley WW, Kanakis C, Jr., Rosen KM. Twenty-four hour continuous ecg recordings in long-distance runners. *Chest*. 1982;82:19-24
15. Hiss RG, Lamb LE. Electrocardiographic findings in 122,043 individuals. *Circulation*. 1962;25:947-961
16. Ector H, Bourgois J, Verlinden M, Hermans L, Vanden Eynde E, Fagard R, De Geest H. Bradycardia, ventricular pauses, syncope, and sports. *Lancet*. 1984;2:591-594
17. Coumbe AG, Naksuk N, Newell MC, Somasundaram PE, Benditt DG, Adabag S. Long-term follow-up of older patients with mobitz type i second degree atrioventricular block. *Heart*. 2013;99:334-338
18. Cheng S, Keyes MJ, Larson MG, McCabe EL, Newton-Cheh C, Levy D, Benjamin EJ, Vasan RS, Wang TJ. Long-term outcomes in individuals with prolonged pr interval or first-degree atrioventricular block. *JAMA*. 2009;301:2571-2577
19. Magnani JW, Wang N, Nelson KP, Connelly S, Deo R, Rodondi N, Schelbert EB, Garcia ME, Phillips CL, Shlipak MG, Harris TB, Ellinor PT, Benjamin EJ. Electrocardiographic pr interval and adverse outcomes in older adults: The health, aging, and body composition study. *Circ Arrhythm Electrophysiol*. 2013;6:84-90
20. Hilgard J, Ezri MD, Denes P. Significance of ventricular pauses of three seconds or more detected on twenty-four-hour holter recordings. *Am J Cardiol*. 1985;55:1005-1008
21. Hood S, Northcote RJ. Cardiac assessment of veteran endurance athletes: A 12 year follow up study. *Br J Sports Med*. 1999;33:239-243
22. Maron BJ, Pelliccia A. The heart of trained athletes: Cardiac remodeling and the risks of sports, including sudden death. *Circulation*. 2006;114:1633-1644
23. D'Souza A, Sharma S, Boyett MR. Crosstalk opposing view: Bradycardia in the trained athlete is attributable to a downregulation of a pacemaker channel in the sinus node. *J Physiol*. 2015;593:1749-1751
24. D'Souza A, Pearman CM, Wang Y, Nakao S, Logantha S, Cox C, Bennett H, Zhang Y, Johnsen AB, Linscheid N, Poulsen PC, Elliott J, Coulson J, McPhee J, Robertson A, da Costa Martins PA, Kitmitto A, Wisloff U, Cartwright EJ, Monfredi O, Lundby A, Dobrzynski H, Oceandy D, Morris GM, Boyett MR. Targeting mir-423-5p reverses exercise training-induced hcn4 channel remodeling and sinus bradycardia. *Circ Res*. 2017;121:1058-1068
25. D'Souza A, Bucchi A, Johnsen AB, Logantha SJ, Monfredi O, Yanni J, Prehar S, Hart G, Cartwright E, Wisloff U, Dobryznski H, DiFrancesco D, Morris GM, Boyett MR. Exercise

training reduces resting heart rate via downregulation of the funny channel hcn4. *Nat Commun*. 2014;5:3775
26. Buhl R, Ersboll AK, Eriksen L, Koch J. Changes over time in echocardiographic measurements in young standardbred racehorses undergoing training and racing and association with racing performance. *J Am Vet Med Assoc*. 2005;226:1881-1887
27. Buhl R, Ersboll AK. Echocardiographic evaluation of changes in left ventricular size and valvular regurgitation associated with physical training during and after maturity in standardbred trotters. *J Am Vet Med Assoc*. 2012;240:205-212
28. Boyet MR, Jewell BR. Analysis of the effects of changes in rate and rhythm upon electrical activity in the heart. *Prog Biophys Mol Biol*. 1981;36:1-52
29. Nayebpour M, Talajic M, Nattel S. Quantitation of dynamic av nodal properties and application to predict rate-dependent av conduction. *Am J Physiol*. 1991;261:H292-300
30. Tadros R, Billette J. Rate-dependent av nodal function: Closely bound conduction and refractory properties. *J Cardiovasc Electrophysiol*. 2012;23:302-308
31. Hamlin RL, Klepinger WL, Gilpin KW, Smith CR. Autonomic control of heart rate in the horse. *Am J Physiol*. 1972;222:976-978
32. Barra SN, Providencia R, Paiva L, Nascimento J, Marques AL. A review on advanced atrioventricular block in young or middle-aged adults. *Pacing Clin Electrophysiol*. 2012;35:1395-1405
33. DiFrancesco D. The role of the funny current in pacemaker activity. *Circ Res*. 2010;106:434-446
34. Baruscotti M, Bucchi A, Viscomi C, Mandelli G, Consalez G, Gnecchi-Rusconi T, Montano N, Casali KR, Micheloni S, Barbuti A, DiFrancesco D. Deep bradycardia and heart block caused by inducible cardiac-specific knockout of the pacemaker channel gene hcn4. *Proc Natl Acad Sci U S A*. 2011;108:1705-1710
35. Mangoni ME, Traboulsie A, Leoni AL, Couette B, Marger L, Le Quang K, Kupfer E, Cohen-Solal A, Vilar J, Shin HS, Escande D, Charpentier F, Nargeot J, Lory P. Bradycardia and slowing of the atrioventricular conduction in mice lacking cav3.1/alpha1g t-type calcium channels. *Circ Res*. 2006;98:1422-1430
36. Marger L, Mesirca P, Alig J, Torrente A, Dubel S, Engeland B, Kanani S, Fontanaud P, Striessnig J, Shin HS, Isbrandt D, Ehmke H, Nargeot J, Mangoni ME. Functional roles of Ca(v)1.3, Ca(v)3.1 and Hcn channels in automaticity of mouse atrioventricular cells: Insights into the atrioventricular pacemaker mechanism. *Channels*. 2011;5:251-261
37. Saeed Y, Temple IP, Borbas Z, Atkinson A, Yanni J, Maczewski M, Mackiewicz U, Aly M, Logantha S, Garratt CJ, Dobrzynski H. Structural and functional remodeling of the atrioventricular node with aging in rats: The role of hyperpolarization-activated cyclic nucleotide-gated and ryanodine 2 channels. *Heart Rhythm*. 2018;15:752-760
38. Temple IP, Logantha SJ, Absi M, Zhang Y, Pervolaraki E, Yanni J, Atkinson A, Petkova M, Quigley GM, Castro S, Drinkhill M, Schneider H, Monfredi O, Cartwright E, Zi M, Yamanushi TT, Mahadevan VS, Gurney AM, White E, Zhang H, Hart G, Boyett MR, Dobrzynski H. Atrioventricular node dysfunction and ion channel transcriptome in pulmonary hypertension. *Circ Arrhythm Electrophysiol*. 2016;9
39. Mesirca P, Alig J, Torrente AG, Müller JC, Marger L, Rollin A, Marquilly C, Vincent A, Dubel S, Bidaud I, Fernandez A, Seniuk A, Engeland B, Singh J, Miquerol L, Ehmke H, Eschenhagen T, Nargeot J, Wickman K, Isbrandt D, Mangoni ME. Cardiac arrhythmia induced by genetic silencing of 'funny' (f) channels is rescued by girk4 inactivation. *Nat Commun*. 2014;5:4664
40. Zhang Z, Yanfang X, Song H, Rodriguez J, Tuteja D, Namkung Y, Shin H-S, Chiamvimonvat N. Functional roles of cav1.3 (α1d) calcium channel in sinoatrial nodes. Insight gained using gene-targeted null mutant mice. *Circ Res*. 2002;90:981-987
41. Guasch E, Benito B, Qi X, Cifelli C, Naud P, Shi Y, Mighiu A, Tardif JC, Tadevosyan A, Chen Y, Gillis MA, Iwasaki YK, Dobrev D, Mont L, Heximer S, Nattel S. Atrial fibrillation promotion by endurance exercise: Demonstration and mechanistic exploration in an animal model. *J Am Coll Cardiol*. 2013;62:68-77
42. Benito B, Gay-Jordi G, Serrano-Mollar A, Guasch E, Shi Y, Tardif JC, Brugada J, Nattel S, Mont L. Cardiac arrhythmogenic remodeling in a rat model of long-term intensive exercise training. *Circulation*. 2011;123:13-22

43. D'Souza A, Wang Y, Anderson C, Bucchi A, Baruscotti M, Olieslagers S, Mesirca P, Johnsen AB, Mastitskaya S, Ni H, Zhang Y, Black N, Cox C, Wegner S, Bano-Otalora B, C. P, Gill E, Logantha SJ, Dobryznski H, Ashton N, Hart G, Zhang R, Zhang H, Cartwright E, Wisloff U, Mangoni ME, da Costa Martins PA, Piggins H, DiFrancesco D, Boyett MR. A circadian clock in the sinus node mediates day-night rhythms in Hcn4 and heart rate. *Heart Rhythm*. 2020;In press
44. St-Pierre J, Grégoire J-C, Vaillancourt C. A simple method to assess group difference in rt-qpcr reference gene selection using genorm: The case of the placental sex. *Sci Rep*. 2017;7:16923
45. Gourdie RG, Severs NJ, Green CR, Rothery S, Germroth P, Thompson RP. The spatial distribution and relative abundance of gap-junctional connexin40 and connexin43 correlate to functional properties of components of the cardiac atrioventricular conduction system. *J Cell Sci*. 1993;105 (Pt 4):985-991
46. Temple IP, Inada S, Dobrzynski H, Boyett MR. Connexins and the atrioventricular node. *Heart Rhythm*. 2013;10:297-304
47. Frank M, Wirth A, Andrie RP, Kreuzberg MM, Dobrowolski R, Seifert G, Offermanns S, Nickenig G, Willecke K, Schrickel JW. Connexin45 provides optimal atrioventricular nodal conduction in the adult mouse heart. *Circ Res*. 2012;111:1528-1538
48. Ragueneau I, Laveille C, Jochemsen R, Resplandy G, Funck-Brentano C, Jaillon P. Pharmacokinetic-pharmacodynamic modeling of the effects of ivabradine, a direct sinus node inhibitor, on heart rate in healthy volunteers. *Clin Pharmacol Ther*. 1998;64:192-203
49. Bucchi A, Baruscotti M, DiFrancesco D. Current-dependent block of rabbit sino-atrial node i(f) channels by ivabradine. *Journal of General Physiology*. 2002;120:1-13
50. Lees-Miller JP, Guo J, Somers JR, Roach DE, Sheldon RS, Rancourt DE, Duff HJ. Selective knockout of mouse erg1 b potassium channel eliminates i(kr) in adult ventricular myocytes and elicits episodes of abrupt sinus bradycardia. *Mol Cell Biol*. 2003;23:1856-1862
51. Wang L, Swirp S, Duff H. Age-dependent response of the electrocardiogram to k(+) channel blockers in mice. *Am J Physiol Cell Physiol*. 2000;278:C73-80
52. Huntzinger E, Izaurralde E. Gene silencing by micrornas: Contributions of translational repression and mrna decay. *Nat Rev Genet*. 2011;12:99-110
53. Agarwal V, Bell GW, Nam JW, Bartel DP. Predicting effective microrna target sites in mammalian mrnas. *Elife*. 2015;4
54. Miranda KC, Huynh T, Tay Y, Ang YS, Tam WL, Thomson AM, Lim B, Rigoutsos I. A pattern-based method for the identification of microrna binding sites and their corresponding heteroduplexes. *Cell*. 2006;126:1203-1217
55. Ding Y, Lawrence CE. A statistical sampling algorithm for rna secondary structure prediction. *Nucleic Acids Res*. 2003;31:7280-7301
56. Hashem SI, Claycomb WC. Genetic isolation of stem cell-derived pacemaker-nodal cardiac myocytes. *Mol Cell Biochem*. 2013;383:161-171
57. Duygu B, Juni R, Ottaviani L, Bitsch N, Wit JBM, de Windt LJ, da Costa Martins PA. Comparison of different chemically modified inhibitors of mir-199b in vivo. *Biochem Pharmacol*. 2019;159:106-115
58. Dirkx E, Gladka MM, Philippen LE, Armand AS, Kinet V, Leptidis S, El Azzouzi H, Salic K, Bourajjaj M, da Silva GJ, Olieslagers S, van der Nagel R, de Weger R, Bitsch N, Kisters N, Seyen S, Morikawa Y, Chanoine C, Heymans S, Volders PG, Thum T, Dimmeler S, Cserjesi P, Eschenhagen T, da Costa Martins PA, De Windt LJ. Nfat and mir-25 cooperate to reactivate the transcription factor hand2 in heart failure. *Nat Cell Biol*. 2013;15:1282-1293
59. Aschar-Sobbi R, Izaddoustdar F, Korogyi AS, Wang Q, Farman GP, Yang F, Yang W, Dorian D, Simpson JA, Tuomi JM, Jones DL, Nanthakumar K, Cox B, Wehrens XH, Dorian P, Backx PH. Increased atrial arrhythmia susceptibility induced by intense endurance exercise in mice requires tnfalpha. *Nat Commun*. 2015;6:6018
60. Flethoj M, Schwarzwald CC, Haugaard MM, Carstensen H, Kanters JK, Olsen LH, Buhl R. Left ventricular function after prolonged exercise in equine endurance athletes. *J Vet Intern Med*. 2016;30:1260-1269

61. Raekallio M. Long term ecg recording with holter monitoring in clinically healthy horses. *Acta Vet Scand*. 1992;33:71-75
62. Tartibian B, Afsargharehbagh R, Malandish A, Z S. Assessment of electrocardiogram indices in postmenopausal women: Effects of aerobic exercise and detraining. *Int J Basic Sci Med*. 2018;3:38-45
63. Boyett MR, Wang Y, Nakao S, Ariyaratnam J, Hart G, Monfredi O, D'Souza A. Point: Exercise training-induced bradycardia is caused by changes in intrinsic sinus node function. *J Appl Physiol*. 2017;123:684-685
64. D'Souza A, Trussell T, Morris GM, Dobrzynski H, Boyett MR. Supraventricular arrhythmias in athletes: Basic mechanisms and new directions. *Physiology*. 2019;34:314-326
65. Monfredi O, Lyashkov AE, Johnsen AB, Inada S, Schneider H, Wang R, Nirmalan M, Wisloff U, Maltsev VA, Lakatta EG, Zhang H, Boyett MR. Biophysical characterization of the underappreciated and important relationship between heart rate variability and heart rate. *Hypertension*. 2014;64:1334-1343
66. Yamaya Y, Kubo K, Amada A, Sato K. Intrinsic atrioventricular conductive function in horses with a second degree atrioventricular block. *J Vet Med Sci*. 1997;59:149-151
67. Zhang Q, Chen J, Qin Y, Wang J, Zhou L. Mutations in voltage-gated l-type calcium channel: Implications in cardiac arrhythmia. *Channels (Austin)*. 2018;12:201-218
68. Karnabi E, Qu Y, Yue Y, Boutjdir M. Calreticulin negatively regulates the surface expression of cav1.3 l-type calcium channel. *Biochem Biophys Res Commun*. 2013;437:497-501
69. Zhou J, Ding WG, Makiyama T, Miyamoto A, Matsumoto Y, Kimura H, Tarutani Y, Zhao J, Wu J, Zang WJ, Matsuura H, Horie M. A novel hcn4 mutation, g1097w, is associated with atrioventricular block. *Circ J*. 2014;78:938-942
70. Liu J, Noble PJ, Xiao G, Abdelrahman M, Dobrzynski H, Boyett MR, Lei M, Noble D. Role of pacemaking current in cardiac nodes: Insights from a comparative study of sinoatrial node and atrioventricular node. *Prog Biophys Mol Biol*. 2008;96:294-304
71. Chiamvimonvat V, Newman D, Tang A, Green M, Mitchell J, Wulffhart Z, Dorian P. A double-blind placebo-controlled evaluation of the human electrophysiologic effects of zatebradine, a sinus node inhibitor. *J Cardiovasc Pharmacol*. 1998;32:516-520
72. Haugaard MM, Pehrson S, Carstensen H, Flethoj M, Hesselkilde EZ, Praestegaard KF, Diness JG, Grunnet M, Jespersen T and Buhl R. Antiarrhythmic and electrophysiologic effects of flecainide on acutely induced atrial fibrillation in healthy horses. *J Vet Intern Med*. 2015;29:339-47.
73. Barold SS and Padeletti L. Mobitz type II second-degree atrioventricular block in athletes: true or false? *Br J Sports Med*. 2011;45:687-90.
74. Barold SS and Hayes DL. Second-degree atrioventricular block: a reappraisal. *Mayo Clin Proc*. 2001;76:44-57.
75. Duygu B, Juni R, Ottaviani L, Bitsch N, Wit JBM, de Windt LJ and da Costa Martins PA. Comparison of different chemically modified inhibitors of miR-199b *in vivo*. *Biochem Pharmacol*. 2019;159:106-115.
76. Mohamed TM, Abou-Leisa R, Stafford N, Maqsood A, Zi M, Prehar S, Baudoin-Stanley F, Wang X, Neyses L, Cartwright EJ and Oceandy D. The plasma membrane calcium ATPase 4 signalling in cardiac fibroblasts mediates cardiomyocyte hypertrophy. *Nat Commun*. 2016;7:11074.
77. Hagendorff A, Schumacher B, Kirchhoff S, Luderitz B and Willecke K. Conduction disturbances and increased atrial vulnerability in Connexin40-deficient mice analyzed by transesophageal stimulation. *Circulation*. 1999;99:1508-15.
78. Jeanmougin M, de Reynies A, Marisa L, Paccard C, Nuel G and Guedj M. Should we abandon the t-test in the analysis of gene expression microarray data: a comparison of variance modeling strategies. *PloS one*. 2010;5:e12336.
79. Inada S, Hancox JC, Zhang H and Boyett MR. One-dimensional mathematical model of the atrioventricular node including atrio-nodal, nodal, and nodal-his cells. *Biophys J*. 2009;97:2117-27.

FIGURE LEGENDS

Figure 1. AV block and AV node intrinsic electrical remodelling in racehorses. A-D, Representative ECG recordings obtained during 24 h radiotelemetry in sedentary (n=6) and trained (n=13) horses. PR intervals (ms) are highlighted in red. **A**, Typical sinus rhythm in a sedentary horse. **B**, Example of type 1 second-degree AV block in a trained horse characterised by irregular PR intervals preceding a dropped QRS complex. **C**, Example of 'Wenckebach phenomenon' observed in trained horses characterised by lengthening PR intervals preceding a dropped QRS complex. **D**, Example of second-degree AV block in a trained racehorse that does not meet the criteria for type 1 second-degree AV block. **E-G,** Heart rate, PR interval and incidence of second-degree AV block in sedentary (n=6) and trained (n=13) horses (*P<0.05, Student's *t* test; statistical significance for incidence of second-degree block tested using Mann-Whitney test). **H,** Relationship between heart rate and duration of detraining. **I**, Relationship between PR interval and duration of detraining. Data in H-I fit by exponential decay curves; best fit curves, R^2 and τ values shown. Red circles denote trained horses and blue circles denote detrained horses. **J**, PR intervals measured in 10 beat epochs corresponding to the minimum and maximum heart rate from 24 h radiotelemetry recordings in sedentary (n=5) and trained (n=5) horses. **K**, PR intervals measured at baseline and on complete pharmacological autonomic blockade in sedentary (n=6 at baseline and n=4 for autonomic block) and trained (n=5 at baseline and n=5 for autonomic block) horses (*P<0.05, Mann-Whitney test). **L**, Masson's trichrome staining of horse AV node demonstrating the location of the compact node (red square). Right panel shows the compact node at a magnified scale. **M**, Representative HCN4 (green signal; top panels) and $Ca_V1.2$ (red signal; lower panels) immunostaining in the compact AV node from sedentary and trained horses. Scale bar = 10 µm. **N**, Signal intensity of HCN4 immunolabelling in sedentary (n= 3 slides/horse from 7 horses) and trained (n= 3 slides/horse from 7 horses) horse AV nodes. Data pooled from two sets of independent experiments and protein expression is normalised to sedentary value (set at 100%) (P value shown, Student's *t* test). **O**, Representative HCN4 western blot from AV node biopsies from sedentary (n=4) and trained (n=5) horses. Corresponding stain-free total protein membrane used for quantification shown in lower panel. **P**, HCN4 protein expression from western blot (n=5/5, P value shown, Student's *t* test)**.** **Q**, Signal intensity of $Ca_V1.2$ immunostaining in sedentary (n=7) and trained (n=7) horse AV node. Data pooled from two sets of independent experiments and protein expression is normalised to sedentary value (set at 100%) (*P<0.05, Student's *t* test). **R**, Representative $Ca_V1.2$ western blot from AV node biopsies from sedentary (n=4) and trained (n=4) horses. Corresponding stain-free total protein membrane used for quantification shown in lower panel. **S**, $Ca_V1.2$ protein expression from western blot (n=5/5, *P<0.05, Student's *t* test)**.**

Figure 2: Long-term training induces AV node dysfunction and transcriptomic remodelling. **A**, PR interval obtained from anaesthetised sedentary and trained mice at baseline (n=6 sedentary/11 trained) and on complete autonomic blockade (n=14 sedentary /13 trained), at cessation of 20 weeks swim training (*P<0.05, 2-way ANOVA with Sidak's multiple comparisons test). **B**, Pacing cycle lengths at which Wenckebach conduction (WCL) occurred and AVERP at 100 ms pacing frequency in sedentary (n=14 for WCL and n =13 for AVERP) and trained (n=11) mice (*P<0.05, Student's *t* test). **C**, Representative recordings obtained during *in vivo* S1-S1 pacing in sedentary (black trace, pacing cycle length 74 ms) and trained (red trace, pacing cycle length 106 ms) mice illustrating the prolongation of the Wenckebach cycle length in trained mice. S, stimulus artifact; V, ventricular deflection. S-V interval is given in ms. **D**, PR interval during *in vivo* S1-S1 pacing at fixed cycle lengths of 100 and 120 ms (n=13 sedentary and 10 trained mice; *P<0.05, 2-way ANOVA with Sidak's multiple comparisons test). **E**, Example of AV node preparation used for extracellular action potential recording. Red circles indicate electrode positions. CS, coronary sinus; FO, fossa ovalis; IVC, inferior vena cava; RAA, right atrial appendage; SVC, superior vena cava. Scale bar = 2 mm. **F**, Spontaneous cycle length of sedentary (n=8) and trained (n=7) AV node preparations. *P<0.05, Student's *t* test. **G** (left panel), Representative spontaneous extracellular potential recordings from sedentary (black trace) and trained (red trace) preparations demonstrating atrial (A) and His (H) signals (marked by vertical lines). **G** (right panel), Spontaneous and paced (at a 150 ms cycle length) A-H intervals obtained

from extracellular potential recordings from sedentary (n=8 for spontaneous and n=4 for paced) and trained (n=7 for spontaneous and n=4 for paced) mice. *P<0.05, 2-way ANOVA with Sidak's multiple comparisons test). **H (top panel)**, Masson's trichrome staining of a 20 µm cryosection of the mouse AV node, demonstrating the location of the AV conduction axis (red square). Scale bar = 500 µm. Inset shows the compact node (circled) at a magnified scale as a compact, ovoid bundle of loosely packed cells distinguishable from the inferior ventricular myocardium (stained purple) by the central fibrous body, a band of connective tissue (stained royal blue). Scale bar = 100 µm. **H (lower panel)**, Laser capture micro-dissection of the AV node tissue from a mouse heart. Left lower panel, HCN4-immunolabelled mouse AV junction corresponding to the boxed area in the lower middle panel. Lower middle panel, 10 µm cryosectioned AV junction of a mouse heart stained with cresyl violet and mounted on a membrane slide for laser capture microdissection. Right panel, the same slide after laser capture microdissection. Scale bars = 200 µm. **I,** mRNA expression of Ca^{2+} channels, Ca^{2+} handling molecules, HCN channels, K^{+} channels and connexins in laser-capture microdissected AV node samples from sedentary (n=5-7) and trained mice (n=5-7) normalised to the expression of *Hprt* and *Pgk1* (*P<0.05, limma test followed by Benjamini-Hochberg false discovery rate correction). See tables S2 and S3 for n numbers for respective transcripts.

Figure 3: Reduced $I_{Ca,L}$ and I_f density in trained mice. A (top panel), Representative $Ca_v1.2$ (red signal) immunostaining in the compact AV node from sedentary and trained mice. Scale bar = 10 μm. White arrows denote specific membrane labelling of $Ca_v1.2$. Blue arrows indicate examples of labelling artefact that was not included in the image analysis. **A (lower panel)** Summarised signal intensity of $Ca_v1.2$ immunolabelling in sedentary (n=6) and trained (n=7) mouse compact AV node (significance assessed by Student's *t* test with Welch's correction for unequal variance). **B**, Representative examples of $I_{Ca,L}$ from single AV node cells isolated from sedentary (left) and trained (right) mice. The inset shows the voltage clamp protocol used. Bottom, $I_{Ca,L}$ IV relationships recorded from sedentary (n= 11 cells from 5 mice) and trained (n= 13 cells from 6) mice. Significance was assessed using a mixed effects linear model on log-transformed data. Sidak's multiple comparisons test was applied for multiple testing correction. P values shown were computed on the geometric mean; density of $I_{Ca,L}$ is shown. **C (top panel)**, Representative HCN4 (green signal) immunolabelling in the penetrating bundle from sedentary and trained mice. The nodal cells lie within the dashed white lines. Scale bar = 200 μm. **C (lower panel)**, Summarised signal intensity of HCN4 immunolabelling in sedentary and trained mouse penetrating bundle (n=6 per group, significance assessed by Student's *t* test). **D,** Representative examples of I_f from single AV cells isolated from sedentary (left) and trained (right) mice. The inset shows the voltage clamp protocol used. Bottom, I_f IV relationships recorded from sedentary (n= 9 cells from 4 mice) and trained (n= 8 cells from 4 mice) mice. Significance was assessed using a mixed effects linear model on log-transformed data. Sidak's multiple comparisons test was applied for multiple testing correction. P values shown were computed on the geometric mean; density of I_f is shown.

Figure 4. **Training effect on $I_{K,r}$ density. A**, Typical examples of ionic currents in AV node cells isolated from sedentary (top panels) and exercise trained (bottom panels) animals under control conditions and after perfusion of 1μM E-4031. E-4031 sensitive current (calculated as 'Control' minus 'E-4031-insensitive' current) in sedentary and trained cells is shown in the right panel. **B,** IV relationships of I_K in AV node cells of sedentary (left, n=15 cells from 4 mice) and exercise trained (right, n=17 cells from 5 mice) animals measured at the end of the depolarizing step before (black circles) and after (blue circles) 1 μM E-4031 application. In red is shown the E-4031-sensitive current density. **C**, same as panel B, but current density was measured just after the pulse (peak tail current). **D**, IV curve for E-4031-insensitive (left, blue circles) and E-4031-sensitive (right, red circles) current measured at the end of the depolarizing step in sedentary (filled symbols) and exercise trained (empty symbols) animals. **E**, same as in D but with peak tail current values. Significance was assessed using a mixed effects linear model on log-transformed data. Sidak's multiple comparisons test was applied for multiple testing correction. P values shown were computed on the geometric mean.

Figure 5. Training-induced reduction in spontaneous firing of AV node myocytes due to $I_{Ca,L}$ and I_f underlies slowing of AV node conduction. A (left panel), Representative action potential recordings from AV node myocytes isolated from sedentary (from n = 9 cells from 4 mice) and trained (from n= 11 cells from 5 mice) animals. The dotted line indicates 0 mV. **A (right panel)**, Action potential recording with time- and voltage-hallmarks used for analysis. **B**, Table summarising AV node action potential parameters recorded from sedentary and trained mice. MDP, maximum diastolic potential; SLDD, slope of the linear phase of diastolic depolarisation; SEDD, slope of the exponential phase of diastolic depolarisation; dV/dt, action potential upstroke velocity; APD, action potential duration. Significance was assessed using a mixed effects linear

model. Sidak's multiple comparisons test was applied for multiple testing correction. P value for SLDD was computed on the geometric mean.**C**, Computational simulation of the effect of the observed changes in $I_{Ca,L}$ and I_f density on AV node conduction. Top, diagram of the one-dimensional model used to simulate conduction through the AV node. The left end of the string of cells was stimulated, and the action potential was recorded at two sites separated by 2 mm in the centre of the string as the action potential propagated along the string. The interval between the two action potentials recorded is longer the slower the conduction velocity. Left, AV node action potentials recorded at the two sites in simulations of the AV node of sedentary and trained mice. The interval between the two action potentials is longer in the case of the simulation of the AV node of the trained mouse; this corresponds to a slower conduction velocity. Right, simulated IV relationships of $I_{Ca,L}$ and I_f in sedentary and trained AV node cells (based on the data in Figure 3B,D).

Figure 6: miRs repress $Ca_V1.2$/HCN4 expression by 3′UTR targeting. A, Expression of 750 miRs in the AV node measured using TaqMan TLDA cards in the AV node of mice. Ratio of miR expression in trained mice (n=8) to expression in sedentary mice (n=7) shown on a logarithmic scale. Red circles indicate significant varying miRs (P<0.05, Limma test with Benjamini-Hochberg false discovery rate correction). **B and C**, Luciferase reporter assay screen for candidate miRs that target the 3′UTR of $Ca_V1.2$ (B) and HCN4 (C). Ratio of Luciferase to Renilla activity was measured in H9C2 cells 24 h after miR cotransfection and compared to control reporter plasmid (no 3′UTR) in H9C2 cells. Error bars indicate range of duplicates in two independent batches of cells. **D and E,** Luciferase/Renilla activity of wild-type or mutant 3′UTR of $Ca_V1.2$ (D) and HCN4 (E) after 24 h miR co-transfection (n=3 replicates in three independent batches of cells; *P<0.05 *versus* control, one-way ANOVA with Holm-Sidak's multiple comparisons test). **F**, Effect of miR overexpression on $Ca_V1.2$ and HCN4 (transcript levels measured 24 h after transfection in ES-derived myocytes). mRNA expression normalised to expression of *Ipo8* and *Hprt.* Data from n=3 independent batches of cells run in triplicate (*P<0.05, one-way ANOVA with Dunnett's multiple comparisons test). For data in figures 6D-6F normality was assumed by the central limit theorem.

Figure 7: Reversal of training-induced PR interval prolongation by miR suppression or detraining. A, Expression of miR-211-5p and miR-432 in the AV node of control or antimiR-treated sedentary and trained mice (n=6/6/6). Transcript expression is normalised to *Snord61* and *Snord95*. Significance assessed by Kruskal-Wallis test with Dunn's multiple comparisons test. **B-D,** Mean heart rate (B), PR interval (C) and PR interval under a constant S1-S1 pacing cycle length of 130 ms (D) measured in anaesthetised antimiRs-treated sedentary and trained mice (n=6/6/6). Significance assessed by Kruskal-Wallis test with Dunn's multiple comparisons test (**B**) or one-way ANOVA with Dunnett's multiple comparisons test (**C-D**). **E**, Representative recordings obtained during *in vivo* S1-S1 pacing in sedentary (black trace, from n=6) trained (red trace, from n=6) mice illustrating the restoration of PR interval to sedentary values with antimiR-432 and antimiR-211-5p (blue trace, from n=6). Downward deflection indicates stimulus artefact; P and R waves labelled. **F (left panel)**, Representative $Ca_V1.2$ western blot using AV node biopsies from control or antimiR-treated sedentary and trained mice. Corresponding stain-free total protein membrane used for quantification shown in lower panel. **F (right panel)**, $Ca_V1.2$ protein expression (normalised to total protein) from western blot (n=3/3/3 run in duplicate). **G (left panel)**, Representative HCN4 western blot (normalised to total protein) using AV node biopsies from control or antimiR-treated sedentary and trained mice. Corresponding stain-free total protein membrane used for quantification shown in lower panel. **G (right panel)**, HCN4 protein expression from western blot (n=3/3/3 run in duplicate. *P<0.05, one-way ANOVA with Holm-Sidak's multiple comparisons test. **H and**

I, Mean heart rate (H) and PR interval (I) obtained in conscious (n=8/8/8 for heart rate and 7/7/7 for PR interval) and anaesthetised (n=8/7/8 for both heart rate and PR interval) sedentary, trained and de-trained mice. **J and K,** mRNA expression of $Ca_V1.2$ (J) and HCN4 (K) measured in AV node biopsies from sedentary (n=7), trained (n=7) and detrained (n=7) mice. Transcript expression normalised to *Ipo8*, *Hprt* and *Tbp1*. Significance for H-K assessed by one-way ANOVA with Tukey's multiple comparisons test with the exception of the anaesthetised group in H where significance was assessed by Kruskal-Wallis test with Dunn's multiple comparisons test.

NOVELTY AND SIGNIFICANCE

What is known

· Endurance athletes can present with dysfunction of the atrioventricular node (AV node), manifesting as first-or second-degree AV block.

· This phenomenon is widely attributed to high vagal tone, even though vagal tone has never been directly measured in athletes.

What new information does this article contribute

· In mice trained by swimming as well as racehorses, we demonstrate intrinsic training-induced electrophysiological remodelling of the AV node, characterised by downregulation of $Ca_v1.2$ and HCN4 and a corresponding decrease in $I_{Ca,L}$ and I_f in isolated AV node myocytes.

· In mice, training-induced AV block could be partially suppressed by combined *in vivo* targeting of microRNA-432 and microRNA-211-5p, determined in this study to be direct regulators of $Ca_v1.2$ and HCN4 expression.

AV block is well tolerated by the young athlete but there is evidence that it can become pathological in the long term: veteran athletes have a higher incidence of bradyarrhythmias and pacemaker implantation. This study is the first mechanistic exploration of training-induced AV block. Using equine and murine models of endurance exercise, we present evidence that training-induced AV node dysfunction is intrinsic to the heart and cannot be attributed to high vagal tone. We instead uncover a predominant role for intrinsic electrical remodelling of AV node myocytes characterised by transcriptional and functional downregulation of key ion channels (notably $Ca_v1.2$ and HCN4 and their corresponding ionic currents) responsible for action potential generation and conduction. We show that the transcriptional remodelling of the AV node ion channels is linked to a repressive microRNA signature; this is the first study to link microRNAs to AV node dysfunction. In proof-of-concept studies, we demonstrate the utility of *in vivo* microRNA suppression for reversing AV node dysfunction. Taken together, these data offer new fundamental insight into a common rhythm disturbance in athletes.

FIGURE 1

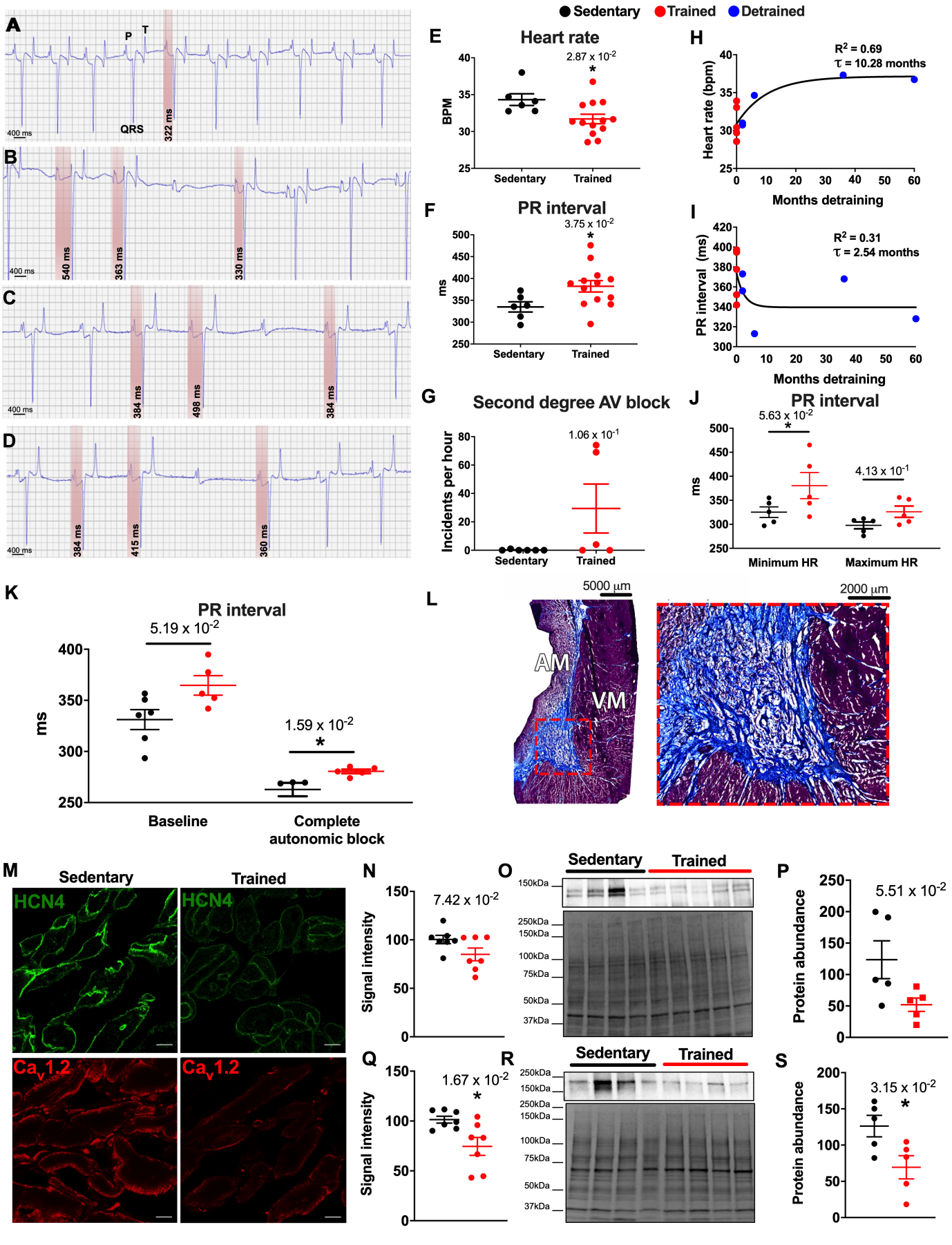
A
P
T
QRS
322 ms
400 ms
B
540 ms
363 ms
330 ms
C
384 ms
498 ms
384 ms
D
384 ms
415 ms
360 ms
Sedentary
Trained
Detrained
E
Heart rate
2.87 x 10-2
BPM
F
PR interval
3.75 x 10-2
ms
G
Second degree AV block
1.06 x 10-1
Incidents per hour
H
R2 = 0.69
τ = 10.28 months
Heart rate (bpm)
Months detraining
I
R2 = 0.31
τ = 2.54 months
PR interval (ms)
Months detraining
J
PR interval
5.63 x 10-2
4.13 x 10-1
ms
Minimum HR
Maximum HR
K
PR interval
5.19 x 10-2
1.59 x 10-2
ms
Baseline
Complete autonomic block
L
5000 µm
2000 µm
AM
VM
M
Sedentary
Trained
HCN4
HCN4
Cav1.2
Cav1.2
N
7.42 x 10-2
Signal intensity
O
Sedentary
Trained
150kDa
250kDa
150kDa
100kDa
75kDa
50kDa
37kDa
P
5.51 x 10-2
Protein abundance
Q
1.67 x 10-2
Signal intensity
R
Sedentary
Trained
250kDa
150kDa
250kDa
150kDa
100kDa
75kDa
50kDa
37kDa
S
3.15 x 10-2
Protein abundance

FIGURE 2

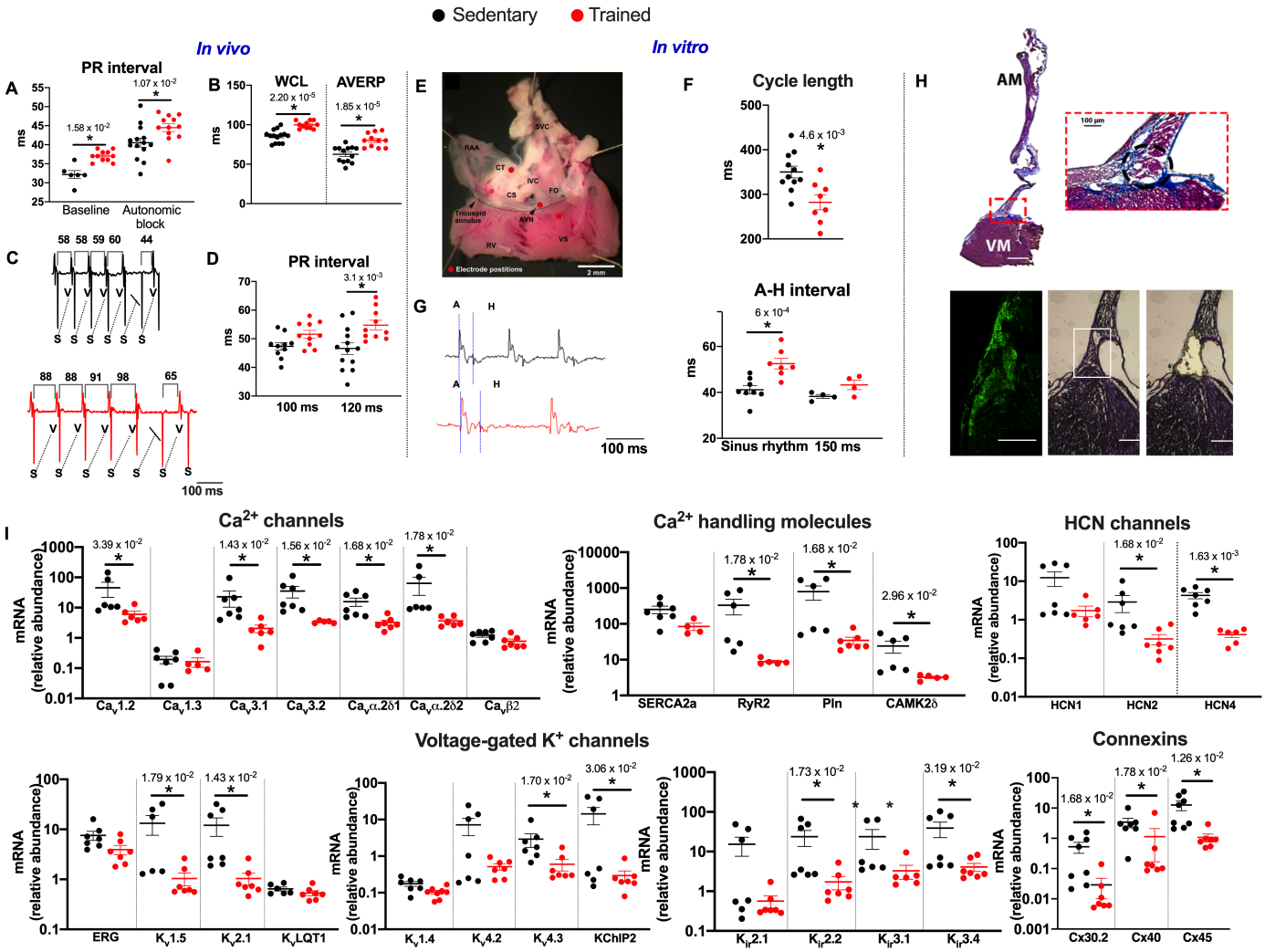
Sedentary
Trained
In vivo
In vitro
A
PR interval
ms
Baseline
Autonomic block
1.58 x 10-2
1.07 x 10-2
B
WCL
AVERP
2.20 x 10-5
1.85 x 10-5
C
D
PR interval
100 ms
120 ms
3.1 x 10-3
E
Electrode positions
2 mm
G
100 ms
F
Cycle length
4.6 x 10-3
A-H interval
6 x 10-4
Sinus rhythm 150 ms
H
AM
VM
100 µm
I
Ca2+ channels
Cav1.2
Cav1.3
Cav3.1
Cav3.2
Cavα.2δ1
Cavα.2δ2
Cavβ2
Ca2+ handling molecules
SERCA2a
RyR2
Pln
CAMK2δ
HCN channels
HCN1
HCN2
HCN4
Voltage-gated K+ channels
ERG
KV1.5
KV2.1
KVLQT1
KV1.4
KV4.2
KV4.3
KChIP2
Kir2.1
Kir2.2
Kir3.1
Kir3.4
Connexins
Cx30.2
Cx40
Cx45
mRNA (relative abundance)

FIGURE 3

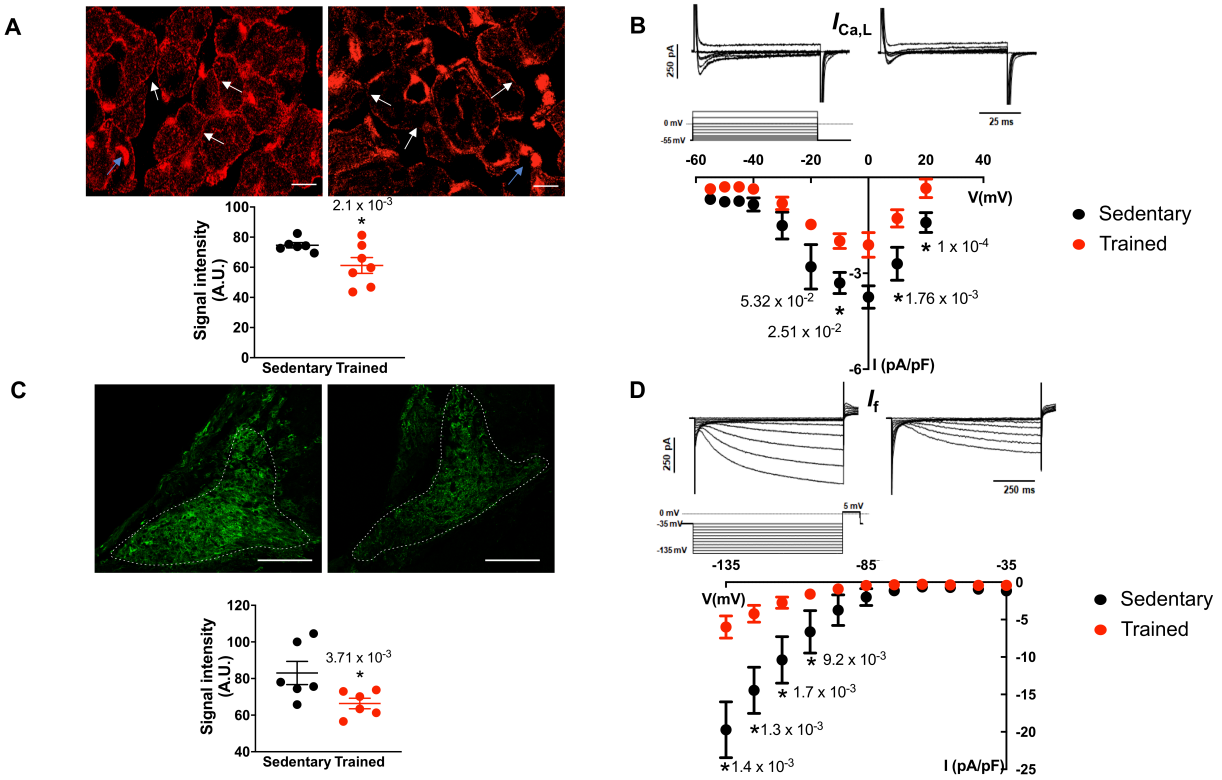
A
2.1 x 10-3
Signal intensity (A.U.)
Sedentary Trained
B
ICa,L
250 pA
25 ms
0 mV
-55 mV
-60 -40 -20 0 20 40
V(mV)
* 1 x 10-4
5.32 x 10-2
2.51 x 10-2
*1.76 x 10-3
I (pA/pF)
Sedentary
Trained
C
3.71 x 10-3
Signal intensity (A.U.)
Sedentary Trained
D
If
250 pA
250 ms
0 mV
-35 mV
-135 mV
5 mV
-135 -85 -35
V(mV)
* 9.2 x 10-3
* 1.7 x 10-3
*1.3 x 10-3
*1.4 x 10-3
I (pA/pF)
Sedentary
Trained

FIGURE 4

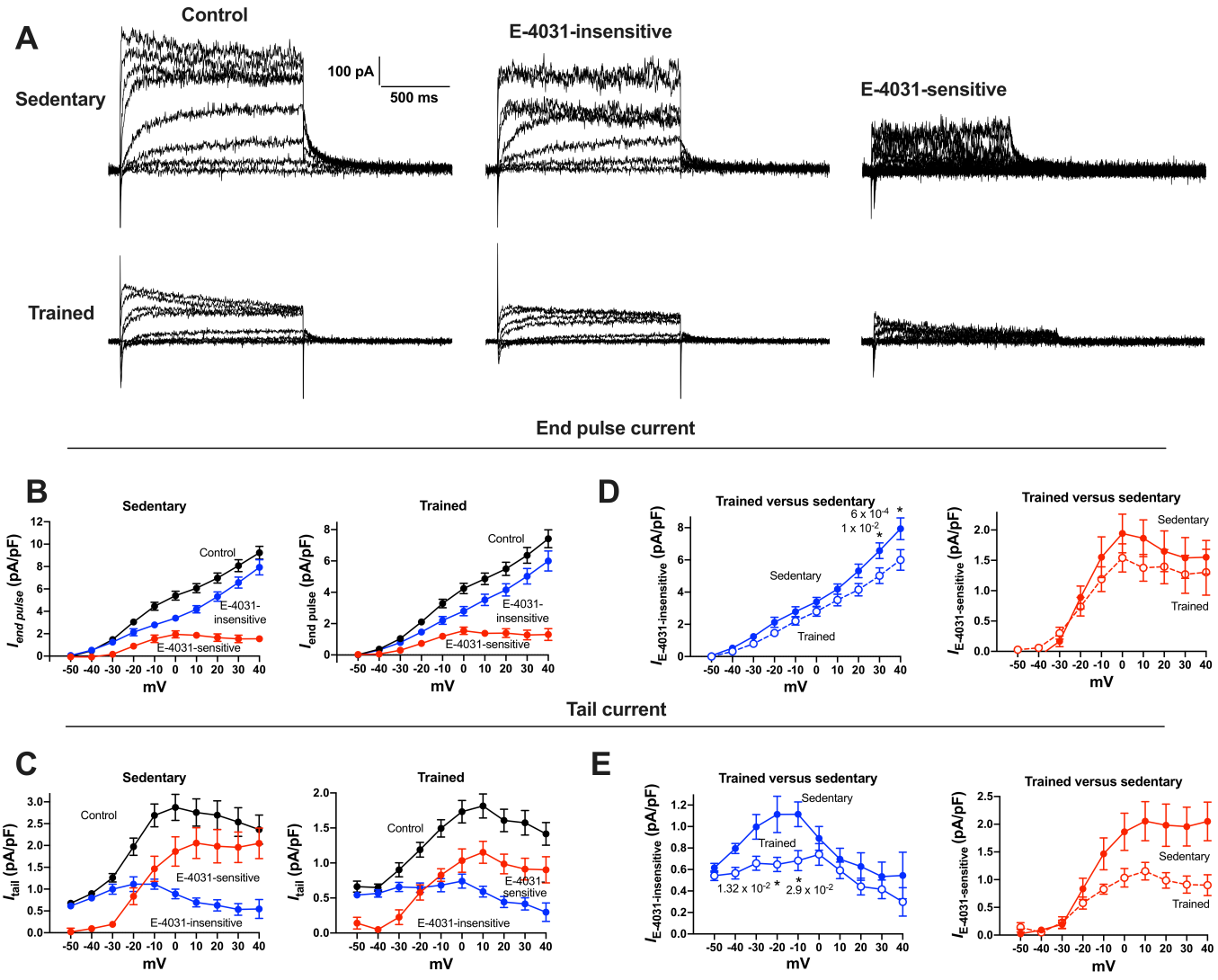
A
Control
E-4031-insensitive
E-4031-sensitive
Sedentary
Trained
100 pA
500 ms
End pulse current
B
Sedentary
Trained
Control
E-4031-insensitive
E-4031-sensitive
mV
D
Trained versus sedentary
6 x 10-4 *
1 x 10-2 *
Sedentary
Trained
Tail current
C
E-4031-insensitive
E
1.32 x 10-2 *
2.9 x 10-2

FIGURE 5

A

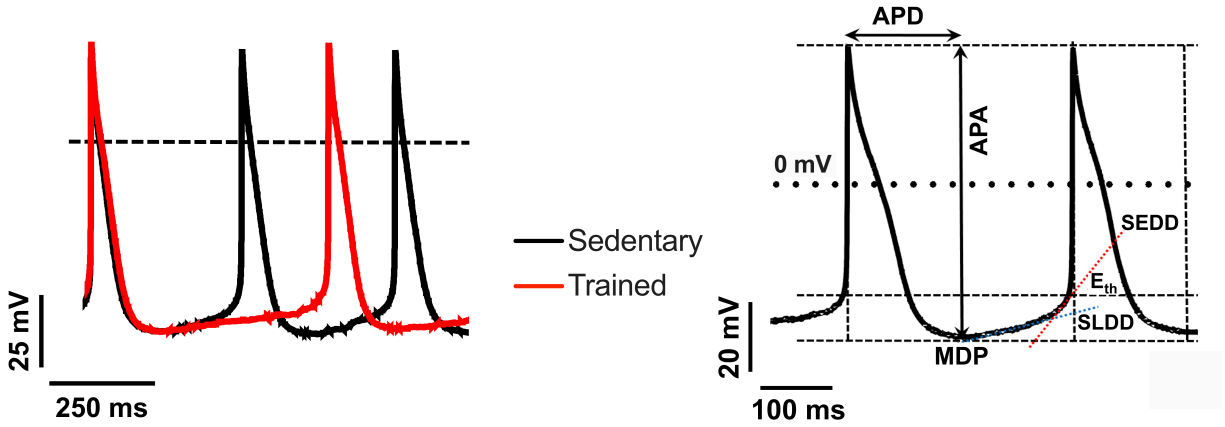

B

	Sedentary	Trained
Rate (bpm)	182 ± 17	127 ± 8* 4.05×10^{-2}
MDP (mV)	-58 ± 1	-54 ± 2
E_{th} (mV)	-37 ± 1	-37 ± 1
SLDD (mV/ms)	0.06 ± 0.01	0.03 ± 0.01* 8.1×10^{-3}
SEDD (mV/ms)	0.26 ± 0.03	0.17 ± 0.01* 1.3×10^{-2}
APA (mV)	87 ± 4	85 ± 5
dV/dt (mV/ms)	19 ± 4	13 ± 5
APD30 (ms)	28 ± 4	32 ± 4
APD50 (ms)	43 ± 6	46 ± 4
APD70 (ms)	59 ± 6	61 ± 5
APD90 (ms)	83 ± 8	83 ± 6

C

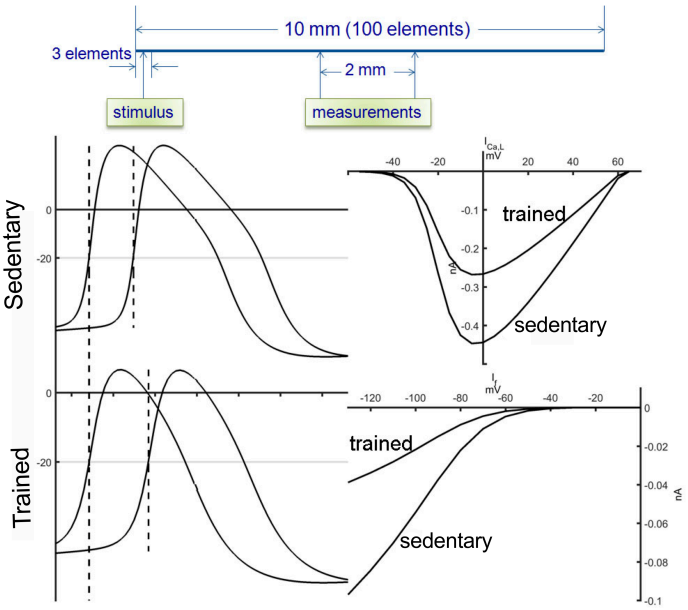

FIGURE 6

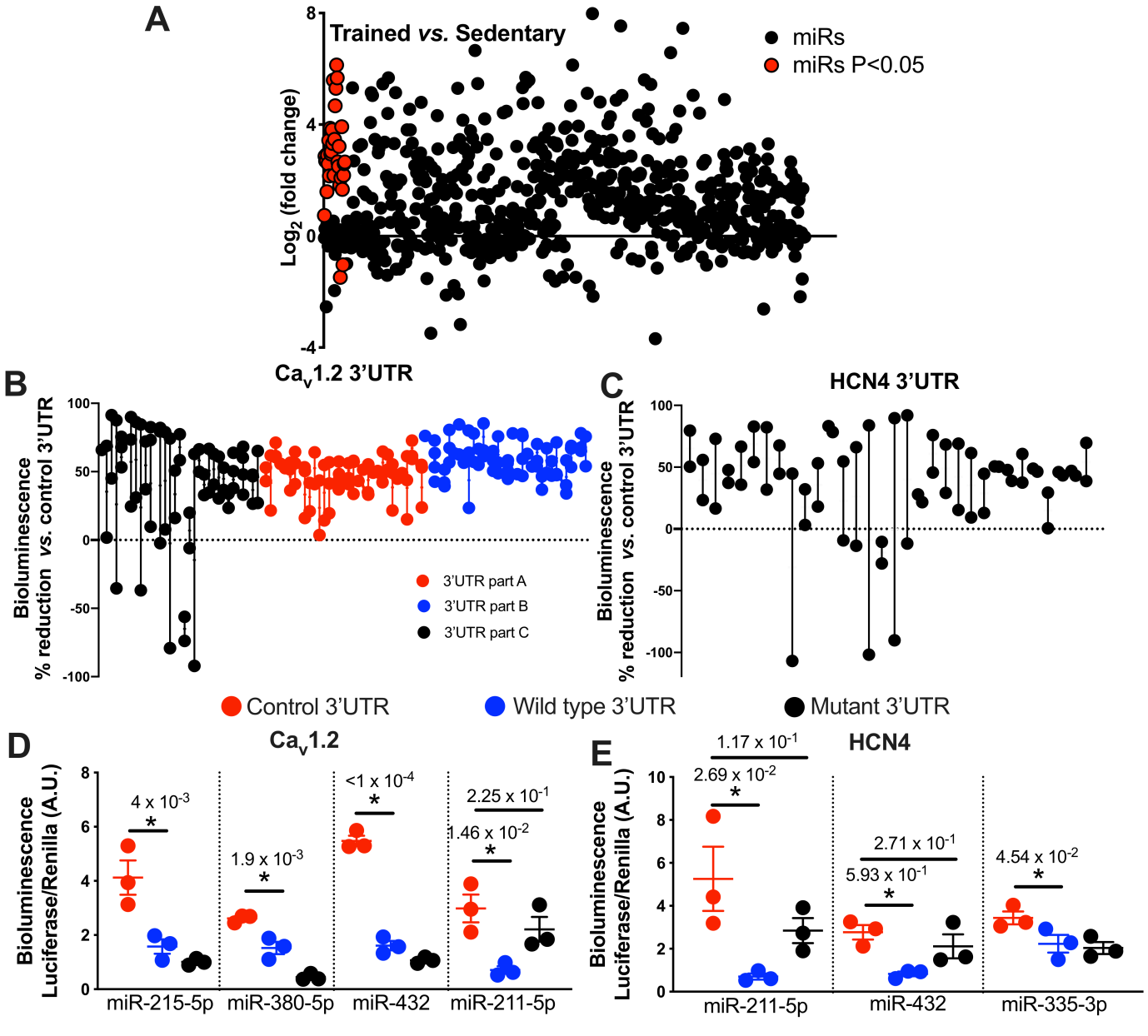

Embryonic stem cell derived $Ca_V1.2$/HCN4 expressing myocytes

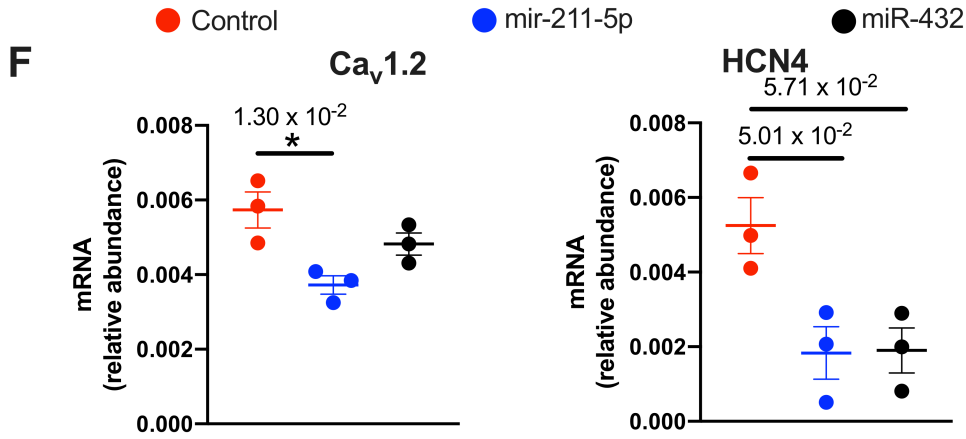

FIGURE 7

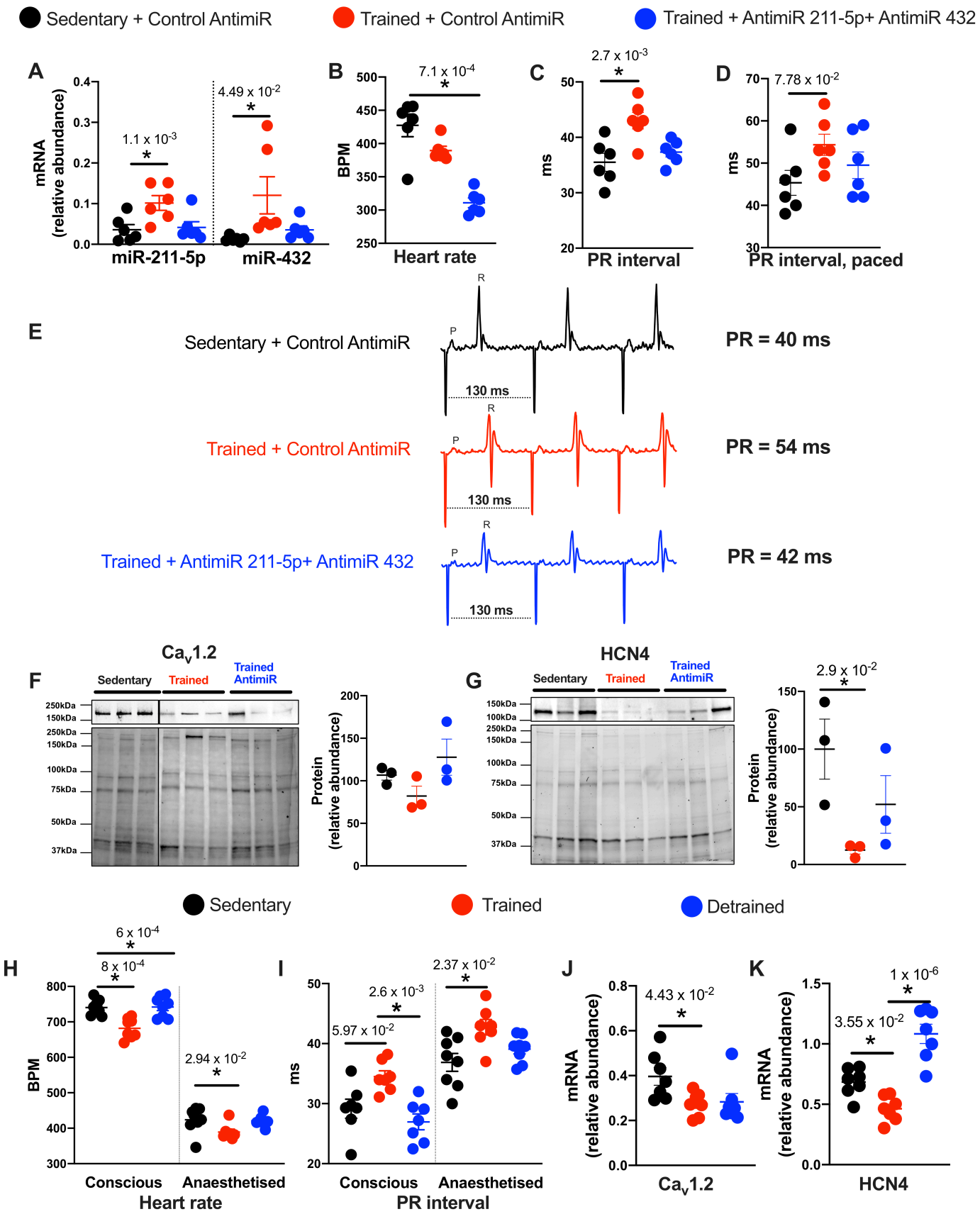
Sedentary + Control AntimiR
Trained + Control AntimiR
Trained + AntimiR 211-5p+ AntimiR 432
A
mRNA (relative abundance)
1.1 x 10-3
4.49 x 10-2
miR-211-5p
miR-432
B
7.1 x 10-4
BPM
Heart rate
C
2.7 x 10-3
ms
PR interval
D
7.78 x 10-2
ms
PR interval, paced
E
Sedentary + Control AntimiR
PR = 40 ms
Trained + Control AntimiR
PR = 54 ms
Trained + AntimiR 211-5p+ AntimiR 432
PR = 42 ms
130 ms
F
Cav1.2
Sedentary
Trained
Trained AntimiR
Protein (relative abundance)
G
HCN4
2.9 x 10-2
Sedentary
Trained
Detrained
H
6 x 10-4
8 x 10-4
2.94 x 10-2
BPM
Conscious
Anaesthetised
Heart rate
I
2.37 x 10-2
2.6 x 10-3
5.97 x 10-2
ms
PR interval
J
4.43 x 10-2
mRNA (relative abundance)
Cav1.2
K
1 x 10-6
3.55 x 10-2
HCN4

SUPPLEMENTAL MATERIAL

EXPANDED MATERIALS AND METHODS

Horse model

Horses

The study was approved by the local ethical committee at the Department of Veterinary Clinical Sciences, University of Copenhagen and the Danish Animal Experiments Inspectorate, and was performed in accordance with the European Commission Directive 86/609/EEC. Sedentary, trained and detrained Standardbred trotters stabled in equine facilities at the University of Copenhagen were studied; sedentary and trained groups had two and three castrated males (geldings) respectively whereas the remaining horses were mares (sedentary = 6 ± 0.57 years of age; trained = 6.2 ± 0.57 years of age; detrained = 7.4 ± 1.28 years of age, no significant age differences between groups, $P>0.05$, one-way ANOVA).

Out of 6 horses allocated to the sedentary group, 5 horses had never participated in a race whereas one horse had participated in one race over 4 years prior to enrolment in the study but had not trained since. Sedentary horses were allowed to walk in a pasture daily. All horses in the trained group were in full training for at least 3 consecutive years. The horses were 'race fit' at the time of enrolment in the study and had competed at professional races within the same month of purchase. The training regimes varied according to trainer-preferences, but in general involved exhaustive training 3-5 times a week. The training typically involved 1 h sessions of either long runs in heavy soil, interval training or sprint sessions. Trained horses were also subjected to 'loosening' exercise in a walker. Horses in the detrained group were retired racehorses that were housed in the equine facility at the University of Copenhagen and had been retired from training for varying durations (2–60 months). It was not possible to perform randomization, allocation concealment or blinding in horse studies as animals were procured based on their training history.

ECG recording

As a part of the clinical examination for enrolment in the study, all horses had a Holter ECG performed at rest in the stall over a 24 h period using a Holter unit with 2 separate channels and bipolar leads as previously described.[72] Electrodes were placed in a modified base-apex lead and secured by adhesive foam pads. Based on clinical and echocardiographic examination, horses were considered clinically healthy with no apparent cardiovascular diseases. For data presented in Figure 1E-G, ECG recordings were obtained between the hours of 14:00-17:00 on a separate occasion within 2 weeks from enrolment.

Autonomic block

Horses were instrumented for Holter ECG recording as described above and the baseline ECG recorded for 15 min at 8:00 am. Complete autonomic blockade was achieved by simultaneous intravenous injection of propranolol 0.20 mg/kg followed by atropine 0.04 mg/kg. The ECG was continuously recorded for 1 h after atropine injection.

Analysis of ECG data

To compute the 24 h variation in heart rate and PR interval the RR intervals from the 24 h Holter recordings were exported to HRV Premium 3.1.0 software (Kubios) from which the average heart rate from 30 min bins over a 24 h period were obtained. PR intervals were manually measured from 10 consecutive beats from ECG segments corresponding to the minimal and maximal heart rate. For all other panels in Figure 1, ECG recordings were imported into LabChart 7 (v7.3.8, ADInstruments). Heart rate and PR intervals were measured over 100 consecutive beats. Beats that included an episode of AV block were not included in these measurements (as the PR interval could not be measured) and the next full waveform was substituted. ECG data were manually analysed for absent QRS complexes, which were categorized as second degree AV block (**Figure 1G**) without differentiating between Type I and Type II second degree AV block, because, generally, type II second-degree AV block is rare in athletes and difficult to diagnose, and its incidence is most commonly due to the misdiagnosis of type I second-degree AV block.[73] In humans, transient sympathetic and parasympathetic surges can cause type I second-degree AV

block to appear as type II second-degree AV block on ECG.[74] Additionally, the infranodal dysfunction of type II second-degree AV block is typically accompanied by a widened QRS complex, which was not seen in any horse. Third degree AV block was not observed in any recording.

Mouse model

Mice

Care and use of laboratory animals conformed to the United Kingdom Animals (Scientific Procedures) Act 198, and European (86/609/CEE) regulations and guidelines. Ethical approval for all experimental procedures was granted by the University of Manchester. Eight-week-old male C57BL/6j mice (Harlan Laboratories; initial body weight, 20–25 g) were randomly assigned to either sedentary or trained groups. Only male mice were used as in our previous experience they are more amenable to swim training. Allocation concealment and blinding was not possible except in the case of echocardiography experiments due to the limited number of trained personnel available to perform techniques. Mice were housed five per cage in a temperature-controlled room (22°C) with a 12 h:12 h light:dark lighting regime and free access to food and water. No animals were excluded from analyses

Anaesthesia

For echocardiography, ECG recording and *in vivo* programmed electrical stimulation, anaesthesia was induced with 2% isoflurane in 100% O_2 with a flow rate of 1 l/min and maintained with 1.5% isoflurane in 100% O_2 with a flow rate of 1 l/min.

Swim training

Mice were subjected to a swimming programme described previously.[24,25] Mice were swim-trained in a tank with a surface area of 32,500 cm^2, depth of 35 cm and water temperature of 32 °C. In the first set of experiments, mice were trained for 10 min day^{-1} and the duration of exercise was extended in daily increments of 10 min until finally reaching 60 min. This duration of exercise was maintained for 20 weeks, which approximates to >10 years of endurance training in humans.[42] In the second set of experiments, mice were trained for 60 min day^{-1} for 4 weeks. Both training protocols produced a prolongation of the PR interval evidenced by ECG recording as described below. In a further cohort of mice, after the last training session (4 weeks), mice were submitted to detraining for 12 weeks in which physical activity was restricted to the space of the cage. All mice were able to complete the training protocol. Age- and weight-matched sedentary littermates served as controls for all experimental conditions and were handled daily.

AntimiR treatment

AntimiR design and dosing was based on previous studies where optimal chemistry for cardiac delivery and knockdown efficiency was determined.[75] Sequences used were as follows:

miR-211-5p antimiR: 5′-Chol-*A*G*GCAAAGGAUGACAAAGG*G*A*A-3’

miR-432 AntimiR: 5′-Chol-*C*U*GCCCACUGAUCUACUCCA*A*G*A-3’

Control AntimiR: 5′-Chol-*A*A*G GCAAGCUGACCCUGA A*G*U* U-3'

where * denotes a phosphothiorate and 5′-Chol-*oligonuleotide denotes a 5′-cholesterol modification. AntimiRs were diluted in sterile saline and administered via intraperitoneal injection on three consecutive days (25 mg/kg body weight). Animals were randomly allocated to injection groups

Echocardiography

At the end of the training period, transthoracic echocardiography was conducted in sedentary and trained mice under anaesthesia (1.5% isoflurane in 100 O_2 with a flow rate of 1 l/min) as described previously.[76] Briefly, an Acuson Sequoia C256 ultrasound system fitted with a 14-MHz transducer (Siemens) was used to image the heart in the two-dimensional short-axis view. Left ventricular end diastolic diameter, left ventricular end systolic diameter, and diastolic posterior wall and interventricular septal thicknesses in diastole were assessed by M-mode echocardiography. Measurements were obtained

using the leading-edge method over a minimum period of three cardiac cycles, with the researcher blinded to treatment groups.

Unconscious ECG recordings

At termination of the experiment, ECGs were recorded under isofluorane anaesthesia as described previously.[24] In separate cohorts of mice, the effect on heart rate and the PR interval of (i) complete autonomic block using a combination of 0.5 mg kg^{-1} atropine and 1 mg kg^{-1} propranolol and (ii) 6 mg kg^{-1} ivabradine were determined as previously described.[24]

***In vivo* programmed electrical stimulation**

Animals were terminally anaesthetised (1.5% isoflurane in 100% O_2 with a flow rate of 1 l /min) and ventilated with a respirator, following which the right atrium was accessed by thoracotomy and an EPR-800 catheter (Millar Instruments) introduced. Electrical stimulation was delivered via a DS3 isolated constant-current stimulator (Digitimer Ltd.) interfacing with a CED Micro3-1401 data acquisition system and controlled by Spike software (Cambridge Electronic Design). Pacing protocols were performed to measure sinus node recovery time, AV node effective refractory period and Wenckebach cycle length as given previously.[38,77] Briefly, the threshold was determined using a fixed S1-S1 protocol with an interval 10 ms below the spontaneous cycle length. A square pulse of duration 2 ms was gradually increased from 0 and the minimum voltage required to capture the atrium was determined. The stimulating voltage was set at 0.5 V higher than the threshold and the output was kept constant for all subsequent pacing protocols. Sinus node recovery time (SNRT) was determined using a S1-S1 protocol with a cycle length of 100 ms, 120 ms and 130 ms. The time taken for the first spontaneous atrial beat after cessation of pacing was defined as the SNRT. Corrected SNRT (cSNRT) was calculated by subtracting the RR interval from the SNRT. Wenckebach cycle length was determined by pacing the atrium for 30 s, starting at a cycle length 10 ms below the spontaneous cycle length, and then a progressively shortened cycle length until Wenckebach conduction was seen between the atrium and the ventricle (Figure 2B). A further set of 30 s S1-S1 pacing protocols was undertaken starting at 11 ms longer than the cycle length at which Wenckebach conduction had occurred. If 1:1 atrial to ventricular conduction occurred the protocol was repeated with a 1 ms reduction in the cycle length of the S1-S1 protocol. The cycle length at which 1:1 atrial to ventricular conduction failed and Wenckebach conduction occurred using 1 ms reductions in cycle length was recorded as the Wenckebach cycle length. AVERP was determined using an S1-S2 protocol. There was an initial drive train of S1 beats (S1-S1, 100 ms) for 8 beats. The initial S1-S2 coupling interval was 100 ms. If the extrastimuli captured the atrium and was conducted to the ventricle the protocol was repeated with a 10 ms reduction in the S1-S2 coupling interval. This was repeated until AV conduction was lost. A new set of protocols was run again with the S1-S2 coupling interval starting at 10 ms greater than the S1-S2 coupling interval at which AV node conduction had failed. If this extrastimulus was conducted successfully from the atrium to the ventricle the protocol was repeated with the S1-S2 coupling interval reduced by 1 ms until AV conduction was lost. The greatest S1-S2 coupling interval that did not conduct after a 1 ms decrement was defined as the AVERP.

General

Histology and immunohistochemistry

Horses were humanely killed and right atrial biopsies (~ 7 cm) encompassing the AV conduction axis were rapidly excised and frozen. In mice, following humane culling under terminal anaesthesia, right atrial preparations encompassing the AV node were rapidly dissected and frozen. To map the location of the AV node, 5 x 30 µm serial cryosections (in the sagittal plane) per mm of the whole preparation were obtained from horse preparations and 5 x10 µm serial cryosections (in the sagittal plane) per 200 µm of the whole preparation were obtained from mouse preparations. Cryosections were first subjected to Masson's trichrome staining for morphological identification of regions of interest within the AV conduction. Trichrome Stain (Masson) Light Green Stain Kit (TCS Biosciences, HS773LG) was used following manufacturers instructions and sections were imaged with light microscopy on a Leica LMD6000 using Axiovision (Carl Zeiss Microscopy).

Once the component structures of the AV conduction axis were identified, corresponding cryosections were immunolabelled. In brief, serial sections were fixed in 10% neutral buffered formalin for 30 min and then washed in phosphate buffered saline (PBS) (Sigma-Aldrich, Cat. No. P3813, Lot No. SLBF4171V) 3 times (10 min each). Following this, sections were permeabilised with 0.1% Triton X-100 (Sigma-Aldrich, Cat. No. X-100) for 30 min and washed in PBS again before being blocked with 1% bovine serum albumin (BSA) (Sigma-Aldrich) for 1 h. Sections were incubated with a primary antibody diluted in 1% BSA (HCN4, Alomone Labs, Cat No. APC-052; $Ca_v1.2$, Alomone Labs, Cat No. ACC-003) at 4°C for 12 h. Sections were washed in PBS once more before being incubated in an appropriate fluorescein isothiocyanate (ThermoFisher A11008) or Cy3-conjugated IgG secondary antibody (Sigma-Aldrich, AP187C) diluted in 1% BSA at room temperature for 90 min. Antibody concentrations were optimised beforehand. After a final 3 washes in PBS, sections were mounted in VECTASHIELD Antifade Mounting Medium (Novus, Cat. No. H-1000). For each batch of slides, a set of slides were processed identically for optimisation of confocal settings and without primary antibody as a negative control for autofluorescence/background correction.

Confocal imaging of immunofluorescence and data analysis

In the first set of experiments, analysis was based on previously described methods.[24] Briefly, images were acquired on a Zeiss LCM PASCAL 5 confocal microscope equipped with x10/1.00 Plan Apochromatic objective, x20/1.00 Plan Apochromatic objective and x63/1.00 Plan Apochromatic oil immersion objective. Appropriate lasers (Argon, Cy3 or mercury lamp) and filters (Rhodamine or FITC) were used to excite the fluorophore-conjugated secondary antibodies and images were captured using an Axiocam HRc camera. The confocal parameters were kept identical throughout each experiment for quantification purposes. Three high power images were taken per section. Immunofluorescence was quantified using Volocity cellular imaging software (Quorum Technologies). In all mouse preparations, the anti-$Ca_v1.2$ antibody produced aggregates of non-specific high pixel intensity labelling artefact. Fluorescence intensity measurements from these structures were excluded from the analysis based on the 'exclude-by-intensity' feature, which successfully identified all aggregates. The sum pixel intensity (in arbitrary units) for the HCN4/$Ca_v1.2$-stained area was divided by the area to give a measurement of intensity per unit area. For immunohistochemistry in the horse, fluorescent intensity was quantified on Z-stacks with a total Z-distance of ~40 µm.

Immunofluorescence imaging in additional horses

Three sections from each horse AV node were prepared for immunohistochemical staining and imaging. One extra preparation was created for negative control. Images were acquired using a Zeiss AxioImager Z1 widefield microscope coupled to a HXP-120 light source and equipped with an AxioCam 506 mono – 6 Mpx camera, using a Plan Apo 20x/0.5 NA objective with a 570-640 emission filter. To cover the entire nodal area 156 tiles making up ~5x7 mm of sampled field were stitched together. Microscopic settings were kept identical for all samples. Scanned images were analysed using ZEN 2.3 Blue edition (Zeiss, 2011) in combination with the extension software ZEN Intellesis (Zeiss; 2017) - a machine learning-based, pixel classifier tool that was used for image segmentation. The model enabled extraction of 128 pixel-features, allowing for color- and shape-based segmentation of three distinctly defined classes: "Nodal tissue", "Background" and "Collagen". The training of the models was performed on sections labelled with both primary antibodies against HCN4 and $Ca_v1.2$, generating a model for each. HCN4 positive regions were analysed by drawing around this area using the interactive analysis tool in ZEN 2.3 Blue edition (Zeiss). For $Ca_v1.2$ the area was located based on morphological characters and by projecting the HCN4 positive region from the preceding slide. Intensity mean value of channel Cy3 was extracted from the analysis. Staining and imaging was done in batches of 10 slides (all animals represented in each batch). To incorporate data from the two horse cohorts, statistical testing on data presented in Figure 1N,Q was carried out on the average fluorescent intensity per animal calculated from n=3 AV node sections/horse from 7 sedentary horses and n=3 AV node sections/horse from 7 trained horses. To incorporate data from the two

separate cohorts, the trained values have been normalised to corresponding sedentary values set at 100%.

Western blot

Western blotting was carried out on AV node biopsies (made up of the HCN4-positive compact node) from horses and mice as well as ES-derived nodal cells following overexpression with miR-211-5p and miR-432. Western blotting was carried out as described previously.[43] Primary antibodies were the same as described for immunolabelling with the exception of Connexin 45 (Alomone Labs, Cat no. ACC-205). HRP-linked anti-rabbit IgG (Cell Signalling 7074S) was used as a secondary antibody. Protein abundance was normalised to total protein on blots.

Laser-capture microdissection

Mouse AV node preparations were dissected, frozen and cryosectioned as given above. 20 µm sections 200 µm apart were subjected to immunolabelling with HCN4 antibody to determine the location and extent of component structures of the AV conduction axis. Based on immunolabelled images, sections were selected and stained with Cresyl Violet to enable visualisation of tissue with light microscopy. In this process, sections were placed in 100% ethanol (3 min), stained with 0.1% Cresyl Violet (4 min), rinsed in tap water, placed in 70% ethanol (2 min), and finally placed in 100% ethanol until laser capture microdissection. Guided by HCN4-positive labelling, the inferior nodal extension, compact node and penetrating bundle were sampled from each preparation using a Leica LMD6000 system and coupled together to represent the entire AV node. Approximately 15 slides per heart were sampled and hearts were not pooled. No obvious variation in the histology or fibrous composition between preparations was noted.

qPCR

Gene expression was assessed using Taqman low density array cards for medium throughput profiling of 96 mRNAs or 750 miRs and by single assay SYBR green qPCR.

Taqman Low Density Array cards

Total RNA from microdissected samples was isolated using the mirVana RNA Isolation Kit (ThermoFisher Scientific), then quantified using a spectrophotometer, the Nanodrop ND-1000 (NanoDrop Technologies, Wilmington, DE, USA). Samples were diluted such that 50 ng of total RNA were used in reverse transcription with SuperScript VILO (ThermoFisher Scientific). 96 target transcripts were simultaneously measured from preamplified cDNA using custom-designed TaqMan Low Density Array microfluidic cards (Applied Biosystems, Cat. No. 2549025; format 96A) on an ABI Prism 7900 HT Sequence Detection System (Applied Biosystem Foster City, CA, USA) as described in detail elsewhere.[4] Amplification plots were analysed using RQ manager (Life Technologies). Ct values were exported to the RealTime Statminer (Integromics) data analysis package that enabled advanced filtering of outlier genes, geNorm-based selection of the optimal endogenous control genes *Hprt* and *Pgk1* (*Hprt*, *Pgk1, Tbp, Ipo8, Gapdh and 18s* tested), and differential expression testing using the non-parametric Limma test[78] followed by Benjamini-Hochberg False Discovery Rate correction. Transcript expression levels were calculated using the ΔCt method. **miR profiling**: 65 ng of total RNA from individual AV node samples was reverse-transcribed using TaqMan miR Reverse Transcription Kit (Cat. No. 4366597) and the product (2.5 µl) was preamplified using Megaplex PreAmp Primers Pool A and B (which is a set of pre-defined pools of 380 stem-looped reverse transcription primers) and TaqMan PreAmp Master Mix (Applied Biosystems) in a 25 µl PCR reaction. The preamplification cycling conditions were 95°C for 10 min, 55°C for 2 min and 75°C for 2 min followed by 12 cycles of 95°C for 15 s and 60°C for 4 min. The preamplified cDNA was diluted with 0.1× TE (pH 8.0) to 100 µl and then 10 µl of diluted cDNA was analysed on a TaqMan Array Card run on the ABI Prism 7900 HT Sequence Detection System. qPCR was performed using TaqMan Array Rodent MiR A+B Cards Set v3.0 (ThermoFisher Scientific). Included on each array were three TaqMan miR assay endogenous controls to allow data normalisation and one TaqMan miR assay not related to rodent as a negative control (ath-miR-159a). Results were analysed using RQ manager (Applied Biosystems) and RealTimeStatMiner (Integromics).

Data analysis was conducted as described for mRNAs above. A combination of snoRNA135, snoRNA202 and U6 was used for normalisation.

Single assay qPCR

cDNA was generated from total RNA extracted using the Qiagen RNeasy Micro Kit from unpooled AV node samples using the miScript II RT kit (Qiagen) and manufacturer's instructions. Primers were obtained from Qiagen GeneGlobe as follows:
Hcn4: QT01053514; $Ca_v1.2$: QT00150752; 18s: QT00291977; Ip08: QT00291977; Hprt: QT00166768; Tbp: QT00198443; miR-211-5p: MS00001897 (mouse and horse); miR-432:MS00017451 (mouse), MS00031850 (horse); Snord61: MS00033705; Snord95 : MS00033726; Rnu62 - MS00033740; Rnu1a1 - YP00203909.
Reference gene combinations for individual experiments were determined using geNorm as given in Online Figure III and are given in accompanying figure legends. Cycling conditions were as follows: mRNA = 95°C for 10 min; 40 cycles of 95°C for 15 s; 60°C for 1 min.
miR = 95°C for 15 min; 40 cycles of 94° C for 15; 55°C for 30 s; 70°C for 30 s. Melt curve analysis was performed at the end of both protocols at the following conditions 95°C 15 s, 60°C for 1 min and 95°C for 15 s. mRNA expression for transcripts was calculated by the ΔCt method.

Ex vivo electrophysiology

AV node function was measured in the isolated AV node using extracellular electrodes. AV node preparations were rapidly dissected while being constantly superfused with oxygenated Tyrode's solution (100 mM NaCl, 4 mM KCl, 1.2 mM $MgSO_2$, 1.2 mM KH_2PO_4, 1.2 mM $CaCl_2$, 25 mM $NaHCO_3$ and 11 mM glucose bubbled with 95% O_2 and 5% CO_2 to give a pH of 7.4.). The preparation was placed in a perfusion bath with oxygenated Tyrode's solution at 36.5°C. Custom designed bipolar electrodes were used to record signals in the atrium and at the His bundle. The A-H interval was measured as the interval from the peak of an atrial signal to the peak of the following His signal. Wenckebach cycle length and AVERP were assessed using pacing protocols as given above for *in vivo* pacing.

Myocyte isolation and patch clamp

Mice were killed by cervical dislocation under general anesthesia with 2% isoflurane in O_2 and beating hearts were quickly removed. The AV node region was excised in warmed (35°C) Tyrode's solution containing (in mM): NaCl, 140; KCl, 5.4; $CaCl_2$, 1.8; $MgCl_2$, 1; Hepes-NaOH, 5; and D-glucose, 5.5 (adjusted to pH 7.4 with NaOH). AV node tissue strips were then transferred into a "low-Ca^{2+}-low-Mg^{2+}" solution containing (in mM): NaCl, 140; KCl, 5.4; $MgCl_2$, 0.5; $CaCl_2$, 0.2; KH_2PO_4, 1.2; taurine, 50; D-glucose, 5.5; bovine serum albumin (BSA), 1 mg/ml; Hepes-NaOH, 5 (adjusted to pH 6.9 with NaOH). Tissue were digested by adding Liberase TM (0.15 mg/ml, Roche Diagnostics GmbH, Mannheim, Germany), elastase (1.9 U/ml, Worthington, Lakewood, USA). Digestion was carried out for a variable time of 15–18 minutes at 35°C. Tissue strips were then washed and transferred into a modified "Kraftbrühe" (KB) medium containing (in mM): L-glutamic acid, 70; KCl, 20; KOH, 80; (±)D-b-OH-butyric acid, 10; KH_2PO_4, 10; taurine, 10; BSA, 1 mg/ml; and Hepes-KOH, 10 (adjusted to pH 7.4 with KOH). Single AV node cells were isolated by manual agitation in KB solution at 35°C for 30–50 s. Cellular automaticity was recovered by re-adapting the cells to a physiological extracellular Ca^{2+} concentration by addition of a solution containing (in mM): NaCl, 10, $CaCl_2$, 1.8 and normal Tyrode solution containing BSA (1 mg/ml). The final storage solution contained (mM): NaCl, 100; KCl, 35; $CaCl_2$,1.3; $MgCl_2$, 0.7; L-glutamic acid, 14; (±)D-b-OH-butyric acid, 2; KH_2PO_4; 2; taurine, 2; BSA 1 mg/ml (pH=7.4).

Patch clamp recording from AV node cells

For electrophysiological recordings, aliquots of the cell suspension were harvested in a 3.5 mm diameter Petri dish and mounted on the stage of an inverted microscope and perfused with normal Tyrode's solution. The recording temperature was 36°C. The whole-cell variation of the patch-clamp technique was used to record cellular ionic currents and cell automaticity, by employing an Axopatch 200A or 700B (Axon Instruments Inc., Foster USA) patch clamp amplifier. Recording electrodes were fabricated from borosilicate glass, by employing a Narishige PC 830 gravity microelectrode puller (Narishige Group, Tokyo, Japan) or a DMZ-Universal-Electrode-Puller (Zeitz-Instruments Vertriebs GmbH, Martinsried, Germany).

Cellular automaticity, $I_{K,r}$ and I_f were recorded under the standard whole-cell configuration during perfusion of standard Tyrode's solution (for I_f recordings, 2 mM $BaCl_2$ was added to Tyrode's solution to block $I_{K,1}$) Patch pipettes were filled with an intracellular solution containing (in mM): KCl 130, NaCl 10, EGTA 1, ATP (Na salt) 2, $MgCl_2$ 0.5 and HEPES 5 (pH adjusted to 7.2 with KOH). For $I_{Ca,L}$, pipette solution contained (in mM): 125 CsOH, 20 tetraethylammonium chloride (TEA-Cl), 1.2 $CaCl_2$, 5 Mg-ATP, 0.1 Li_2-GTP, 5 EGTA and 10 HEPES (pH adjusted to 7.2 with aspartate). 30 μM tetrodotoxin (Latoxan, Portes lès Valence, France) was added to external standard Tyrode solution to block I_{Na}. Electrodes had a resistance of ~3 MΩ. Seal resistances were in the range of 2–5 GΩ. All electrophysiological data were recorded using pCLAMP 8 (Molecular Devices, Sunnyvale, CA, USA). Data were analysed off-line using Clampfit 9.2 (Molecular Devices, Sunnyvale, CA, USA). GraphPad Prism 7.02 (Graphpad Software, La Jolla, USA) and SAS v9.4 (SAS Institute). Data were analysed by initially establishing whether a transformation was required to ensure all assumptions were valid. Examination of residual diagnostics indicated that a log transformation was required. The analysis used a mixed effects linear model, with fixed effects of activity level (sedentary or trained), and voltage (mV) or action potential parameter. The interaction between these two effects was also included. The nested random effects in the model were the 'animal' and 'myocyte within animal ID'. A variance components structure was assumed. Components of variance were estimated from the model of residual variability (unexplained by the model), between myocytes within animal variability and additional variability between animals. The percentage of total variability accounted for by each of the components was also calculated. Note that for action potential measurements there is only one observation for each cell (for each parameter type), the between cells (within animal variability) and the residual variability are inseparable – labelled residual.

The following variability component estimates were obtained:

	Between animals		**Between myocytes (within animal)**		**Residual**		**Total Variability (σ^2)**
	Log	**%**	**Log**	**%**	**Log**	**%**	
$I_{Ca,L}$ (Figure 3B)	0.016	16.5%	0.0069	7.1%	0.0742	76.4%	0.0971
I_f (Figure 3D)	0.065	46.4%	0.0187	13.3%	0.0565	40.3%	0.1402
I_K (Figure 4D,E)	0	0.0%	0.028	57.7%	0.0205	42.3%	0.0485

Action potential parameters (Figure 5B)	**Residual**		**Between animals**		**Total Variability (σ^2)**
	Log	**%**	**Log**	**%**	
Rate	1558	100%	0	0.0%	1558
SLDD	0.0225	100.0%	0	0.0%	0.0225
SEDD	0.0033	100.0%	0	0.0%	0.0033

This analysis showed that for I_K and action potential parameters all the variability was between cells, within animals. We conclude, for these data, that there is no correlation between measurements that are made on the same animal. Therefore, comparisons reported in Figures 4B,D and Figure 5B) are based on a mixed effects linear model where activity status (sedentary or trained), voltage or action potential parameter were designated as fixed effects and myocytes were specified as random effects. For $I_{Ca,L}$ and I_f (Figures 3B

and 3D) activity status and voltage were fixed effects and animals specified as random effects in a mixed effects linear model. For all datasets, the model included the interaction between factors to determine interdependence. Comparisons were conducted using a 2-sided 5% test, and applying a Sidak multiple comparison adjustment.

Computer modelling

To simulate the AV node action potential, the model of the rabbit AV node action potential (N-type) from Inada *et al.*[79] was used. General equations are:

$$\frac{dV}{dt} = \frac{I_{total}}{C_m} \quad (1)$$

$$I_{total} = I_{Ca,L} + I_{K,r} + I_f + I_{st} + I_p + I_{NaCa} + I_b \quad (2)$$

where V (mV) is the membrane potential, t (ms) is the time, I_{total} (pA) is the total membrane current, and C_m (pF) is the membrane capacitance. The total membrane current is the sum of seven ionic currents, which are shown in equation (2). A one-dimensional (1D) model was used to simulate conduction in the AV node. The model includes 100 elements and each element is 100 μm in length. The reaction-diffusion equation used was:

$$\frac{\partial V}{\partial T} = \frac{I_{total}}{C_m} + D\frac{\partial^2 y}{\partial x^2} \quad (3)$$

where D is the diffusion coefficient. D was set to 0.001 μS mm^2. One end of the model (elements 1 to 3) was stimulated at 3 Hz. The conduction velocity was calculated from the times of arrival of the action potential at the 41st and 61st elements to avoid the influence of the boundaries. To simulate the effect of athletic training, the conductance of I_f in the model was reduced by 60% and the conductance of $I_{Ca,L}$ in the model was reduced by 40% based on the patch clamp recordings in isolated AV node myocytes as given above.

Computational prediction of miR targets

Previously validated target prediction algorithms RNA22, miRDB and Sfold were used to investigate whether differentially expressed miRs identified by TLDA card profiling had predicted binding sites in the 3′UTR of $Ca_v1.2$ and HCN4 (**Supplementary Table S5**). 3′UTR sequences were obtained from UCSC Genome Browser.

Luciferase reporter gene assays

miR mimics were purchased from Dharmacon. The following 3′UTR luciferase reporter constructs (GeneCopoeia) were used:

p*m*Hcn4-3′UTR-Luc - MmT100218-MT06
p*m*Cav1.2-3′UTR-Luc - MmiT077219a-MT06 (part A), MmiT077219b-MT06 (part B) and MmiT077219c-MT06 (part C)
p*m*NegCtrl-3′UTR-Luc - Negative control 3′UTR plasmid, CmiT000001-MT06

All plasmids contained reporters for both firefly and renilla luciferase. 24 h prior to transfection, 10^5 H9C2 cells were plated in 48 well plates. Cells were transfected with 0.25 μg wild-type or mutated 3′UTR plasmid and 25 nM of miR mimic, using 1.25 μl of Lipofectamine 2000. Firefly and renilla luciferase were measured at 24 h post-transfection using the Dual-Luciferase Reporter Assay on the GloMax Explorer System (both Promega) according to the manufacturer's instructions. The luminescence intensity of firefly luciferase was normalised to that of Renilla luciferase.

Site directed mutagenesis

Site directed mutagenesis was carried out using the PCR based Quick Change site directed mutagenesis protocol (Stratagene). Primers were designed to make the appropriate

mutations as given in Online Figure VII. Reaction mixtures of 50 µl contained 20 ng of template DNA, 125 ng of both forward and reverse mutagenic primers, 1x Pfu PCR buffer, 240 µM dNTPs and 2.5 units *PfuTurbo* DNA polymerase. These reactions were subjected to an initial denaturation at 95 for 30 s, followed by 12 PCR cycles of 95˚C for 30 s, 45˚C for 1 min and 65˚C for 2 min/kb of plasmid. Completed reactions were treated with 10 units *Dpn I* at 37˚C for 2 h to digest the methylated parental DNA after which 5 µl was used to transform chemically competent XL1-Blue strain of *E. coli* (Agilent) by heat shock. Presence of desired mutations was confirmed by Sanger sequencing. A fragment of the plasmid containing the 3′UTR mutations was excised with appropriate restriction endonucleases and subcloned into appropriate vectors for transfection as given above.

SDM Primers		
Name	**Forward primer sequence 5′-3′***	**3′UTR site mutated (bp)**
HCN4 SDM miR-211-5p and miR-335-3p†	GAGGGAGAGAGGGAGGCTGGGTGGGTGGGGGGAGCAGACAAG†	219-229
HCN4 SDM miR-432	TCCCTCTTCTTTTTCTTGGTCGTTTGTTCCTTCAGGTTTAACTGTG	30-39
$Ca_v1.2$ SDM miR-211-5p	CTTCCTCTACAAACCCAGTCAACCGTACAGAGGTGAAAGGAACTC	4645-4653
$Ca_v1.2$ SDM miR-380-5p	GCTTTGAGGAAAATAAGACTGAAGCAATCGCTCAGATTTTGCCTACG	2319-2326
$Ca_v1.2$ SDM miR-432	CTGGATTTCAAAAGAGCTAGACGAACCCCACGGAAGCTGATGTTAAG	3985-3993
$Ca_v1.2$ SDM miR-215-5p	AGAGGGGTGGGGAGTGAGGAAACGAGAAGCCTTAAACCCCACCACCAC	4102-4108

*Reverse primers were the reverse complement of the forwards sequence. †This primer was designed to mutate 4 overlapping miR binding sites: 3 sites for miR-211-5p and 1 site for miR-335-3p.

miR overexpression studies in ES-derived myocytes

ES-derived myocytes (Shox2, ATCC® CRL3256™) were maintained in mouse embryonic stem cell basal medium (ATCC) supplemented with 15% fetal bovine serum, 1% penicillin-streptomycin and 0.05 mM β-mercaptoethanol. Cells were passaged using Accutase dissociation reagent (Sigma). For miR overexpression, $1.0x10^5$ cells/well were plated in 24 well plates 24 h prior to transfection with 25 nM miR mimic (Dharmacon). Lipofectamine 2000 (Invitrogen) was used for transfections and cells were incubated for 24 h with Lipofectamine-miR complexes, prior to collection in TRIzol reagent (Invitrogen). RNA was

extracted using the PureLink RNA Mini kit (ThermoFisher) according to the manufacturer's instructions. cDNA was generated using the miScript II RT kit (Qiagen), using the HiFlex buffer option, to allow analysis of miRs and mRNAs in the same cDNA sample. The miScript SYBR green PCR kit was used to measure miR expression. The reaction comprised 1 µl cDNA, 1× miScript universal primer, 1× miScript miR assay, 1× Quantitect SYBR green and DNAse-free water. All samples were run in duplicate. Reaction conditions: denaturation step of 95°C for 15 min followed by 40 cycles of amplification and quantification steps of 94°C for 15 s, 55°C for 30 s and 70°C for 30 s. miR expression was calculated by the ΔCt method with normalisation to expression of *Rnu6-2*, *Snord65* and *Snord91*.

Statistical analysis

Animal numbers were estimated *a priori* (while obtaining ethical approval and funding for the studies). This was based on power calculations estimated using StatMate (GraphPad Software, Inc) with 80% power and 95% confidence interval using standard deviation values from our previously published work on cardiac electrophysiological and molecular alterations in swim-trained mice*.* [24,25]

Statistical analysis of experimental data was carried out using GraphPad Prism 8 (GraphPad Software, Inc.) and SAS v 9.4 (SAS Institute). Details of individual statistical tests applied are given in the Statistical Analysis table. For all experiments, Residual diagnostics were examined and a Shapiro-Wilk test for normal distribution applied to confirm that the assumptions for the analysis to be valid were applicable. Where data were not normally distributed and/or the number of observations was <7 a non-parametric test (Mann-Whitney test or Kruskal-Wallis test) was used. If data were normally distributed an unpaired Student's *t* test (two sided) was used to analyse differences between two groups. When the null hypothesis of equal variance was rejected, an unpaired t-test with Welch's correction was used. To compare multiple normally distributed groups, an ANOVA (one- or two-way) was used. Dunnett's, Holm-Sidak, Sidak or Tukey's test were applied for multiple testing correction, automated by the software package used. $P<0.05$ was regarded as significant. In figures, means±SEM are given in dot plots; asterisks indicate significance. Statistical tests for qPCR data and electrophysiological recordings in isolated AV node myocytes are detailed in the relevant sections above. A limitation of the statistical analysis in this work is that multiple testing correction was only conducted on high-throughput qPCR data (presented in Supplemental tables S2-S4 and in Online Figures I(E) and IV) but not across the entire dataset.

Online Table I: Echocardiography parameters of sedentary mice and mice trained for 5 months and statistical significance of any difference assessed by Student's *t* test. (Normality was assessed by Shapiro Wilk test and by examination of residual diagnostics on a Normal Quantile plot). LVDd, left ventricular diastolic diameter; BW, body weight; LVDs, left ventricular systolic diameter; dIVS, left ventricle septal wall thickess; dPW, left ventricular posterior wall thickness.

	Sedentary mice (n=15)	**Trained mice (n=15)**	**P value**
LVDd/BW (cm/g)	0.13	0.14	2.87×10^{-4}
LVDs/BW (cm/kg)	0.09	0.08	5×10^{-3}
LV Mass/BW	4.14	3.67	2.3×10^{-1}
Relative wall thickness	0.37	0.39	2.2×10^{-1}
dIVS/LVDd	32.58	30.97	3.9×10^{-1}
dPW/LVDd	19.37	18.6	4.5×10^{-1}
Stroke volume (µl)	55.2	59.88	1.6×10^{-1}
Ejection fraction (%)	72.74	71.91	7.6×10^{-1}
Fractional shortening (%)	34.93	35.48	7.4×10^{-1}
Heart rate (beats/min)	543.21	488.13	47.6×10^{-3}

Online Table II: mRNAs in the mouse AV node that change significantly in response to training. Expression normalised to *Hprt* and *Pgk1* in sedentary and trained mice, statistical significance of the difference, ratio of expression in trained mice:sedentary mice, and n numbers shown.

mRNA	Sedentary mice (mean±SEM)	Trained mice (mean±SEM)	FDR adjusted P value	Trained/sedentary (%)	n
HCN channels					
HCN2	2.9 ± 1.4	0.32 ± 0.1	0.017	11%	7/7
HCN4	4.3 ± 0.8	0.41 ± 0.1	0.002	10%	7/6
Na^+ channels					
$Na_v1.5$	13.1 ± 6.19	2.1 ± 1.3	0.018	16%	6/7
SCN1B	8.7 ± 3.2	0.7 ± 0.1	0.009	8%	7/7
Ca^{2+} channels					
$Ca_v1.2$	45.2 ± 23.4	6.1 ± 1.5	0.034	13%	6/6
$Ca_v3.1$	22.8 ± 12.5	2.1 ± 0.6	0.014	9%	7/6
$Ca_v3.2$	35.4 ± 14.6	3.4 ± 0.2	0.016	10%	7/5
$Ca_vα2δ1$	15.8 ± 4.8	3.2 ± 0.6	0.017	21%	7/7
$Ca_vα2δ2$	63.3 ± 38.0	3.6 ± 0.6	0.018	6%	6/6
Transient outward K^+ channels					
KChIP2	14.2 ± 7.1	0.3 ± 0.1	0.047	2%	7/7
$K_v4.3$	2.9 ± 1.2	0.6 ± 0.2	0.017	21%	7/7
Delayed rectifier K^+ channels					
$K_v1.2$	2.0 ± 0.9	0.2 ± 0.1	0.017	9%	7/7
$K_v1.5$	13.2 ± 5.6	1.0 ± 0.3	0.018	8%	6/7
$K_v2.1$	12.1 ± 4.8	1.0 ± 0.3	0.014	9%	7/7
Inward rectifier K^+ channels					
$K_{ir}2.2$	23.7 ± 10.3	1.7 ± 0.6	0.017	7%	7/7
$K_{ir}3.4$	38.9 ± 16.4	4.1 ± 0.9	0.022	11%	7/7
$K_{ir}6.1$	3.7 ± 1.7	0.3 ± 0.1	0.017	7%	7/7
SUR2	10.4 ± 4.1	1.3 ± 0.2	0.018	12%	7/6
Miscellaneous K^+ channels					
SK1	2.8 ± 1.3	0.16 ± 0.04	0.032	6%	7/7
SK2	0.8 ± 0.3	0.11 ± 0.03	0.022	13%	7/6
SK3	0.9 ± 0.3	0.11 ± 0.03	0.008	12%	7/7
TWIK-1	0.3 ± 0.1	0.02 ± 0.01	0.008	7%	6/7
Cl^- channels					
Chloride channel 2	1.4 ± 0.6	0.12 ± 0.04	0.019	9%	6/7
Chloride channel 3	20.8 ± 9.5	1.0 ± 0.1	0.019	5%	6/7
Gap junction channel					
Cx30.2	0.5 ± 0.2	0.03 ± 0.02	0.017	5%	7/7
Cx40	3.4 ± 1.2	1.1 ± 1.0	0.018	33%	7/7
Cx45	12.7 ± 5.1	1.1 ± 0.3	0.013	8%	7/7
Na^+-K^+ Pump					
Na^+-K^+ pump α1 subunit	162.6 ± 82.6	22.5 ± 4.1	0.031	14%	6/6
Na^+-K^+ pump α2 subunit	121.9 ± 53.9	4.5 ± 0.6	0.016	4%	7/7
Na^+-K^+ pump α3 subunit	0.3 ± 0.1	0.05 ± 0.01	0.019	19%	6/7
Intracellular Ca^{2+}-handling					
Phospholamban	697.5 ± 306.0	34.5 ± 7.8	0.017	5%	7/7
Calsequestrin 2	83.6 ± 37.0	8.9 ± 1.5	0.044	11%	7/4
RYR2	286.9 ± 138.0	8.8 ± 0.8	0.018	3%	7/5
SLC8A1	295.1 ± 135.4	12.7 ± 2.9	0.018	4%	7/7
Ca^{2+}/calmodulin-dependent protein kinase II	21.5 ± 7.9	3.2 ± 0.2	0.007	15%	7/5
Extracellular matrix components					
Collagen type 1 a	68.1 ± 25.2	11.4 ± 3.1	0.021	17%	7/6
Fibronectin-1	32.0 ± 12.3	3.3 ± 1.1	0.008	10%	7/7
Interleukin-1β	0.15 ± 0.08	0.007 ± 0.004	0.013	4%	7/7
MMP2	11.4 ± 4.6	1.1 ± 0.3	0.018	10%	7/7
MMP9	2.3 ± 1.0	0.1 ± 0.03	0.014	4%	7/7
TGFβ1	17.9 ± 10.2	0.4 ± 0.1	0.018	2%	7/6
TIMP4	6.4 ± 2.7	0.4 ± 0.1	0.018	6%	7/7
Vimentin	781.3 ± 463.0	27.5 ± 8.8	0.030	4%	7/7
Transcription factors					
GATA4	22.5 ± 7.6	4.6 ± 0.9	0.018	20%	7/6
IRX3	1.7 ± 0.8	0.1 ± 0.01	0.003	6%	7/7
KLF4	6.2 ± 2.1	1.5 ± 0.2	0.017	24%	7/6
MEF2C	3.4 ± 1.3	0.3 ± 0.1	0.014	10%	7/6
NFκβ	50.6 ± 23.7	1.5 ± 0.2	0.019	3%	7/7
NKX2-5	128.0 ± 58.7	3.9 ± 1.1	0.030	3%	7/6
REST	12.7 ± 6.1	0.5 ± 0.1	0.018	4%	7/7
SP1	18.4 ± 7.8	2.0 ± 0.3	0.042	11%	7/7
TBP	26.6 ± 13.1	0.3 ± 0.1	0.026	1%	7/7
TBX18	7.1 ± 3.8	0.4 ± 0.1	0.042	6%	7/7
TBX3	8.9 ± 3.5	1.2 ± 0.4	0.008	13%	7/7
Miscellaneous					
BMP2	12.2 ± 7.8	1.4 ± 0.4	0.017	8%	7/7

Online Table III: mRNAs in the mouse AV node that do not change significantly in response to training. Expression normalised to *Hprt* and *Pgk1* in sedentary and trained mice, P value of the difference, and n numbers shown.

mRNA	Sedentary mice (mean±SEM)	Trained mice (mean±SEM)	FDR adjusted P value	n
HCN channels				
HCN1	12.3 ± 5.1	1.8 ± 0.5	0.075	7/6
Na^+ channels				
$Na_v1.1$	0.01 ± 0.009	0.002 ± 0.001	0.118	5/5
Ca^{2+} channels				
$Ca_v1.3$	0.022 ± 0.012	0.004 ± 0.001	0.923	7/5
$Ca_v\beta2$	1.2 ± 0.2	0.8 ± 0.1	0.157	7/7
Transient outward K^+ channels				
$K_v1.4$	0.2 ± 0.03	0.1 ± 0.01	0.139	7/7
$K_v4.2$	7.2 ± 3.6	0.5 ± 0.1	0.138	7/7
K_vLQT1	0.6 ± 0.1	0.5 ± 0.1	0.518	6/7
ERG-1	7.6 ± 1.6	3.9 ± 0.8	0.083	7/7
Inward rectifier K^+ channels				
$K_{ir}2.1$	15.3 ± 7.7	0.6 ± 0.2	0.077	7/7
$K_{ir}3.1$	23.7 ± 12.3	3.3 ± 1.3	0.056	6/6
$K_{ir}6.2$	4.9 ± 2.2	1.1 ± 0.3	0.054	6/7
SUR1	6.1 ± 2.4	1.5 ± 0.8	0.163	7/5
Miscellaneous K^+ channels				
TASK1	15.8 ± 6.5	5.3 ± 1.5	0.095	7/6
TRPC6	0.006 ± 0.002	0.003 ± 0.001	0.060	6/7
Connexins				
Cx43	5.9 ± 3.4	0.8 ± 0.1	0.611	7/7
Intracellular Ca^{2+}-handling				
SERCA2	251.8 ± 60.5	84.8 ± 28.0	0.101	7/3
IP_3 receptor 2	4.1 ± 1.7	0.5 ± 0.05	0.090	7/5
PMCA1	1.6 ± 0.5	0.8 ± 0.2	0.101	7/6
PMCA4	7.4 ± 3.4	0.8 ± 0.1	0.090	7/7
Sarcolipin	331.6 ± 157.3	40.8 ± 29.6	0.151	7/5
Extracellular matrix components				
Collagen type 3 a	31.8 ± 18.6	3.9 ± 1.0	0.054	7/6
CTGF	3.9 ± 0.5	3.8 ± 1.0	0.704	7/6
Elastin	34.6 ± 14.5	4.2 ± 1.1	0.051	7/7
TIMP1	4.4 ± 1.9	0.4 ± 0.1	0.067	7/6
TNF	0.03 ± 0.01	0.01 ± 0.003	0.163	7/7
Transcription factors				
KLF15	1.6 ± 0.4	1.0 ± 0.4	0.222	7/6
SHOX2	0.11 ± 0.05	0.06 ± 0.05	0.052	7/7
Miscellaneous				
Atrial natriuretic peptide precursor	1702.1 ± 817.2	41.2 ± 14.0	0.121	6/5
Brain natriuretic peptide precursor	10.1 ± 3.1	9.1 ± 6.9	0.188	7/7

Online Table IV: miRs in the mouse AV node that change significantly in response to training. Expression normalised to *snoRNA135*, *snoRNA202* and *U6* in sedentary and trained mice, n numbers, statistical significance of the difference, and fold change (expression in trained mice/expression in sedentary mice) shown.

miR	Sedentary mice (mean±SEM)	Trained mice (mean±SEM)	n S/T	P	Fold change
mmu-miR-432	0.005 ± 0.003	0.4 ± 0.2	6/8	0.0339	70.42
mmu-miR-452-5p	0.17 ± 0.1	8.8 ± 5.1	6/8	0.0022	51.09
mmu-miR-325-3p	1.1 ± 0.6	53.7 ± 27.3	6/8	0.0373	48.30
mmu-miR-380-5p	0.02 ± 0.01	1.0 ± 0.5	6/8	0.0288	39.47
mmu-miR-374-5p	1.8 ± 1.1	46.6 ± 21.2	6/8	0.0298	25.53
mmu-miR-592-5p	4.1 ± 1.7	61.7 ± 20.4	6/8	0.0078	15.18
mmu-miR-1964-3p	2.2 ± 1.6	31.9 ± 14.9	6/8	0.0053	14.57
mmu-miR-215-5p	2.1 ± 1.1	30.0 ± 8.8	6/8	0.0038	14.02
mmu-miR-335-3p	1.8 ± 1.5	19.5 ± 10.9	6/8	0.0176	11.07
mmu-miR-1958	19.5 ± 7.0	211.7 ± 91.7	6/8	0.0335	10.83
mmu-miR-298-5p	1.55 ± 1.4	15.5 ± 6.8	6/8	0.0026	10.02
mmu-miR-503-5p	1.4 ± 1.3	12.9 ± 5.8	6/7	0.0135	9.29
mmu-miR-211-5p	0.2 ± 0.1	1.6 ± 1.1	6/8	0.0110	8.17
mmu-miR-208b-3p	66.5 ± 34.8	512.0 ± 220.0	6/8	0.0205	7.70
mmu-miR-1931	33.5 ± 14.1	250.5 ± 86.4	6/7	0.0219	7.47
mmu-miR-1193-3p	22.4 ± 19.0	163.6 ± 112.9	6/7	0.0371	7.28
mmu-miR-142-3p	0.003 ± 0.001	0.02 ± 0.01	6/8	0.0386	6.48
mmu-miR-16-1-3p	7.2 ± 4.6	46.4 ± 19.7	6/8	0.0271	6.45
mmu-miR-463-5p	0.0006 ± 0.0001	0.004 ± 0.002	6/8	0.0256	6.32
mmu-miR-881-3p	2.7 ± 2.1	17.3 ± 7.3	6/7	0.0406	6.30
mmu-miR-743b-5p	5.9 ± 3.4	36.0 ± 11.5	6/8	0.0346	6.07
mmu-miR-1947-3p	15.5 ± 15.0	93.3 ± 85.3	6/8	0.0348	6.00
mmu-miR-467e	17.9 ± 11.0	101.4 ± 48.6	6/8	0.0296	5.65
mmu-miR-707	6.3 ± 3.5	28.5 ± 10.4	5/6	0.0065	4.53
mmu-miR-327	0.005 ± 0.002	0.024 ± 0.008	6/8	0.0364	4.53
mmu-miR-1959	0.0008 ± 0.0002	0.004 ± 0.001	6/8	0.0291	4.46
mmu-miR-544-3p	0.003 ± 0.001	0.012 ± 0.003	6/8	0.0054	4.24
mmu-miR-540-5p	36.2 ± 28.5	127.7 ± 39.0	6/8	0.0214	3.53
mmu-miR-615-3p	39.8 ± 39.8	127.3 ± 43.1	4/8	0.0209	3.19
mmu-miR-1897-3p	0.0002 ± 0.0001	0.0006 ± 0.0001	6/8	0.0312	3.008
mmu-miR-105	83.8 ± 66.9	140.2 ± 50.1	5/8	0.0377	1.67
mmu-miR-693-5p	121.1 ± 61.8	59.2 ± 43.1	4/8	0.0193	0.48
mmu-miR-541-5p	0.03 ± 0.01	0.012 ± 0.006	6/8	0.0462	0.358

SUPPLEMENTAL FIGURES

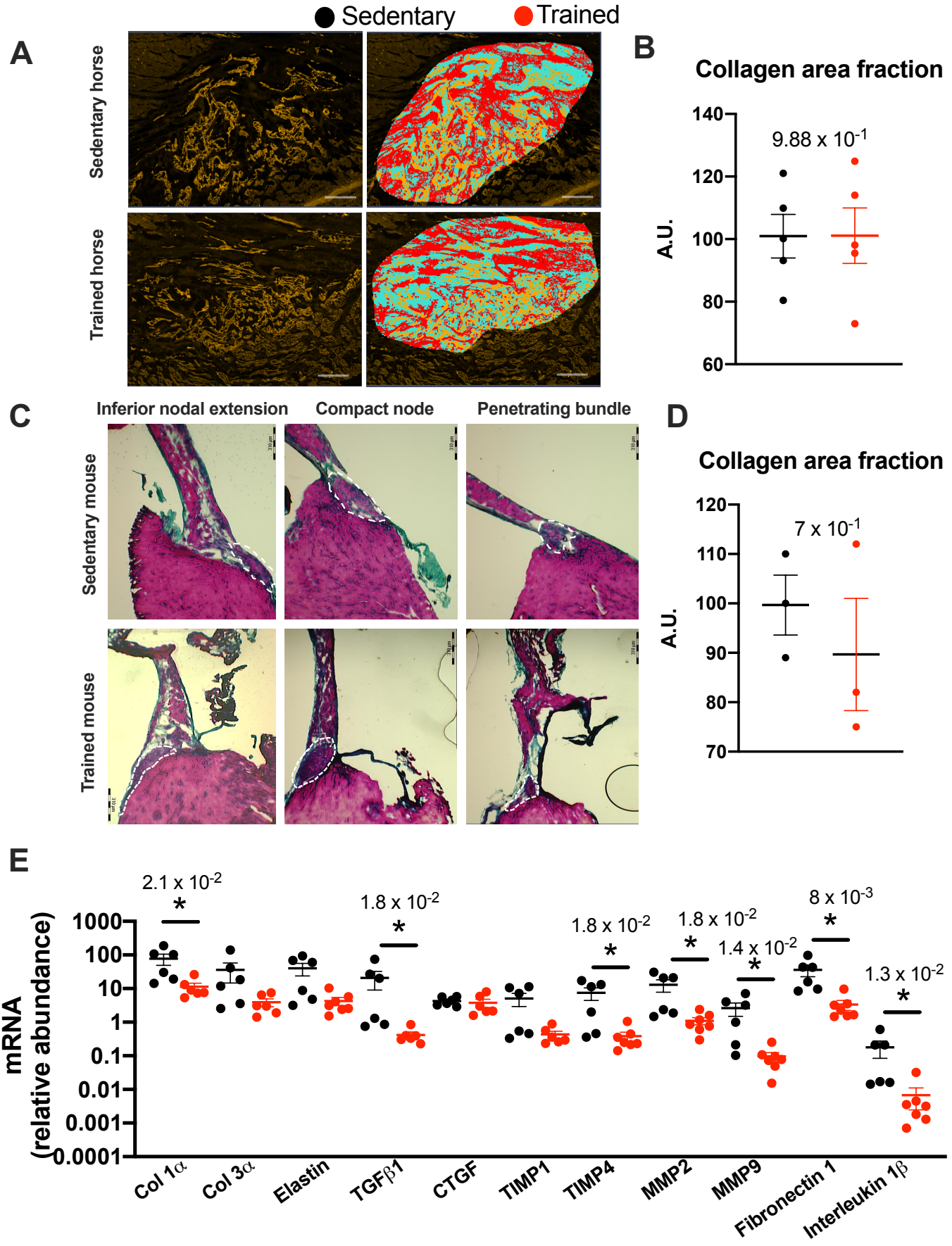

Online Figure I. No evidence of a training-induced increase in AV node collagen deposition in horses and mice. A (left panel), Representative images of the compact node identified in sedentary and trained racehorses by HCN4 immunolabelling in cryosections of AV node biopsies. **A (right panel)**, Segmented images of cryosections corresponding to those given in (A) subjected to pixel classification

using Zen Intellesis (Zeiss) allowing for colour- and shape-based segmentation of nodal cells (yellow), background (blue) and collagen (red). Scale bar =1000 μm. **B**, Collagen area fraction (arbitrary units, AU) in the compact node from sedentary (n=5) and trained (n=5) horses. Significance tested by Student's *t* test. Change from sedentary values set at 100 shown. **C,** Representative images of the mouse AV conduction axis (circled by dashed white line) identified using Masson's trichrome staining. Inferior nodal extension, compact node and penetrating bundle shown. Scale bar=310 μm. **D**, Collagen area fraction in the AV conduction axis from sedentary (n=3) and trained (n=3) mice from Image J analysis of images like those in C. Change from sedentary values set at 100 shown. Significance tested by Mann-Whitney test. **E,** Abundance of transcripts for extracellular matrix components and mediators measured using TaqMan Low Density Array Cards in the AV node of sedentary and trained mice normalised to the expression of *Hprt* and *Pgk1*. *P<0.05, Limma test followed by Benjamini-Hochberg false discovery rate correction. See tables S2 and S3 for n numbers for respective transcripts.

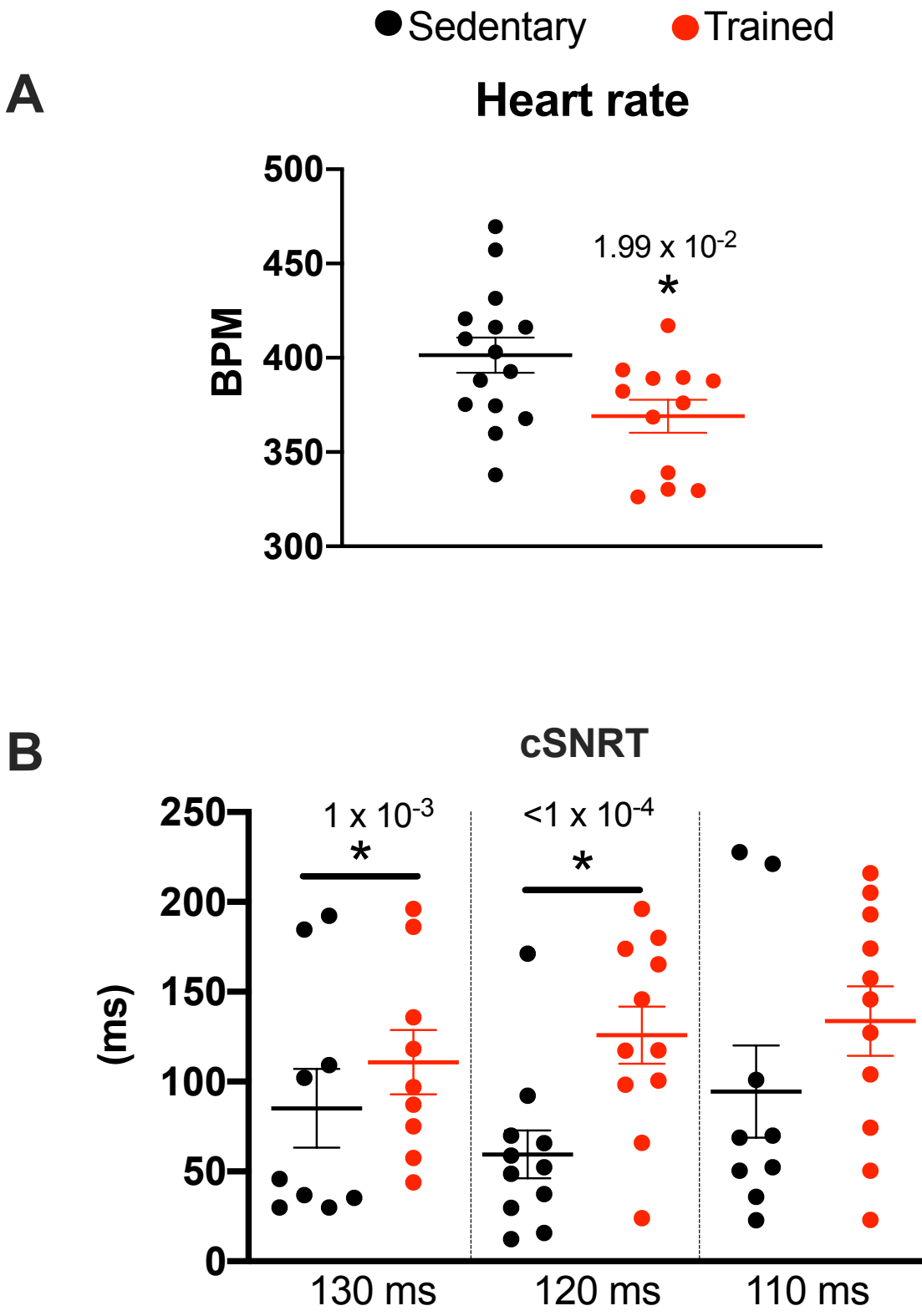

Online Figure II. Swim training induces sinus bradycardia and prolongs the corrected sinus node recovery time in mice. **A**, Heart rate in anaesthetised sedentary (n=14) and trained (n=12) mice (P<0.05, Student's *t* test). **B**, Corrected sinus node recovery time (cSNRT) at three pacing cycle lengths measured during *in vivo* S1-S1 pacing in sedentary and trained mice. *P<0.05, 2-way ANOVA with Sidak's multiple comparisons test.

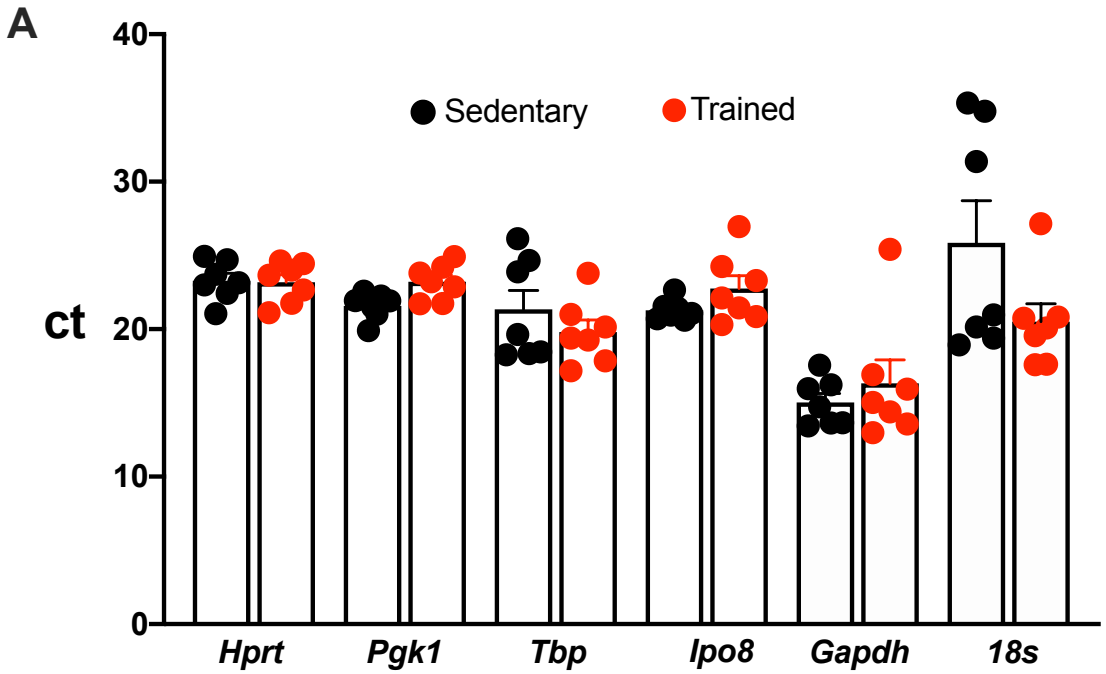

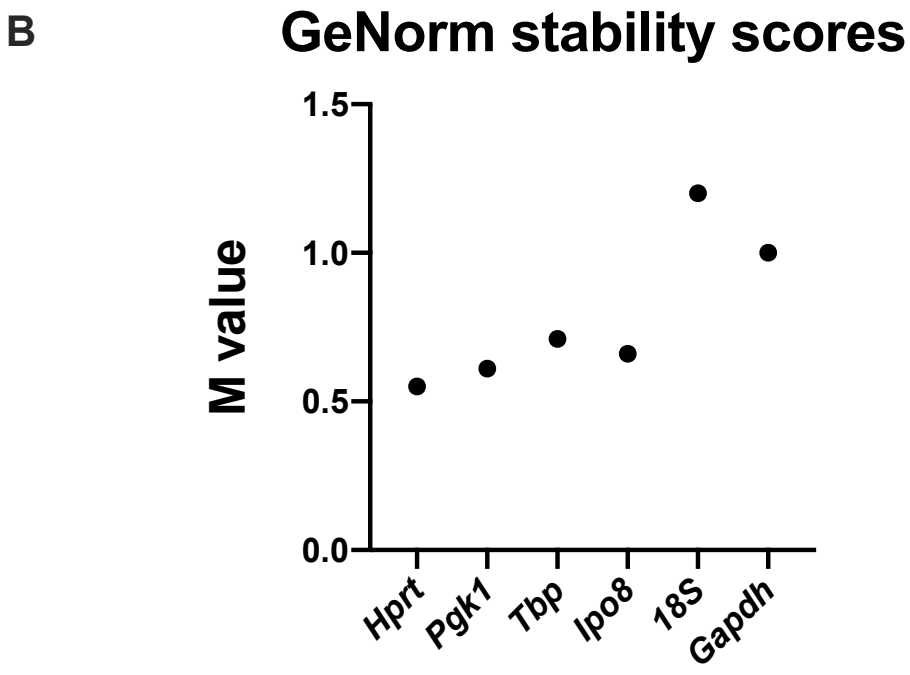

Online Figure III. **Selection of optimal reference genes for transcriptional profiling of the AV node**. **A**, Abundance of six reference transcripts in microdissected AV node samples from sedentary (n=7) and trained animals (n=7); Ct values shown. **B**, M values from GeNorm for the three reference transcripts computed from data presented in A. A lower M value is indicative of greater transcript stability between groups.

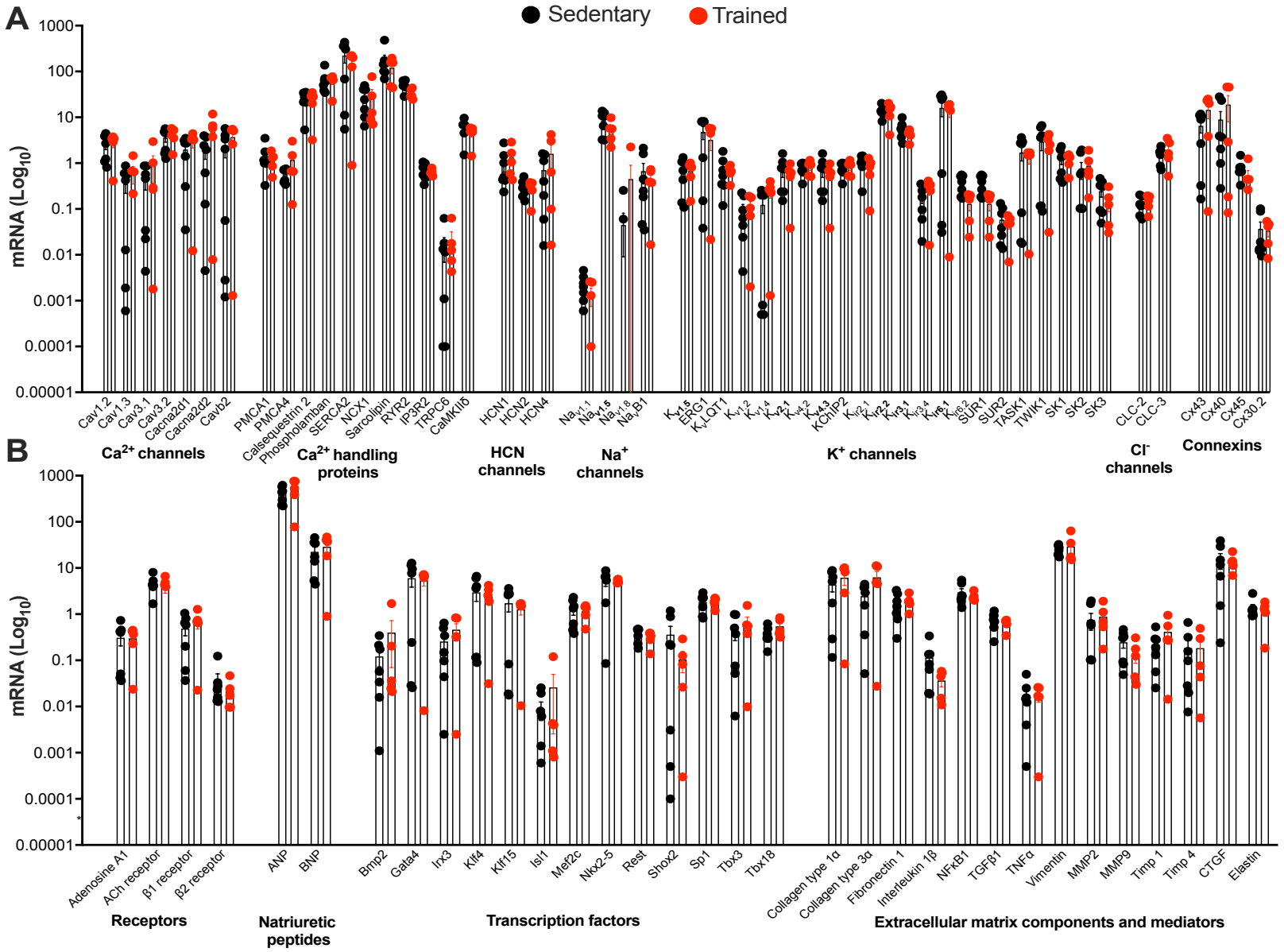

Online Figure IV. **No evidence of training-induced transcriptional remodelling in the right atrium. A**,**B** mRNA expression of selected transcripts in laser-capture microdissected right atrial samples from sedentary (n=7) and trained (n=5) mice normalised to the expression of *Ipo8 and Tbp* (determined by GeNorm stability scoring in right atrial samples).

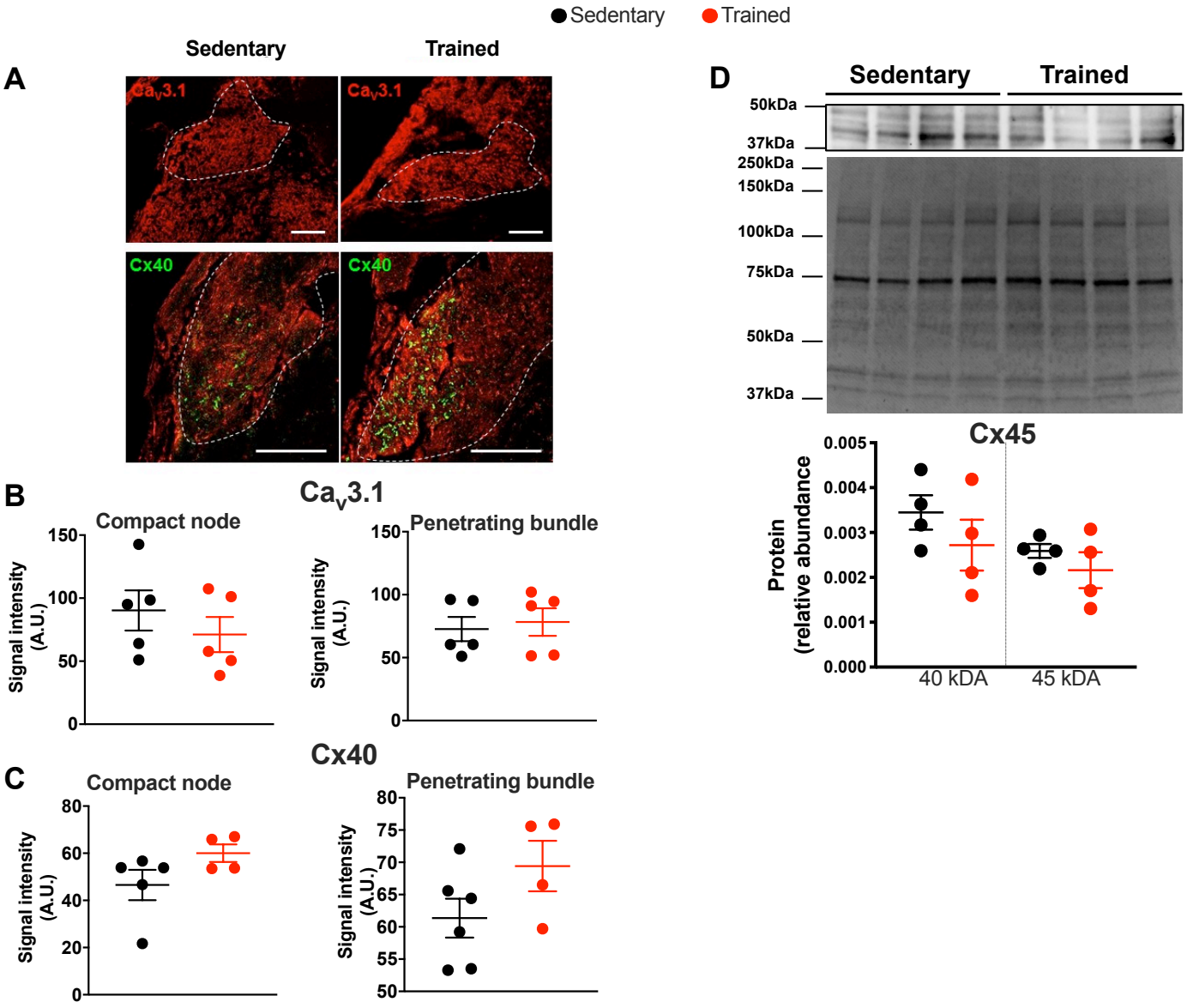

Online Figure V. Exercise training does not impact protein levels of $Ca_V3.1$, Cx40 or Cx45 in the AV node. A, Representative $Ca_V3.1$ (red labelling within circle) and Cx40 (green) immunostaining from sedentary and trained mice. Scale bar = 200 µm. **B and C**, Fluorescent intensity of $Ca_V3.1$ (B) and Cx40 (C) quantified from compact node and penetrating bundle of sedentary and trained mice. (n= 5 mice per group for $Ca_V3.1$ labelling in the compact node and the penetrating bundle. n=5 sedentary and 4 trained mice per group for Cx40 and in the penetrating bundle.) **D**, Representative Cx45 western blot from AV node biopsies from sedentary (n=4) and trained (n=5) mice. Corresponding stain-free total protein gel used for quantification of bands at both 40 kDa and 45 kDa shown in lower panel.

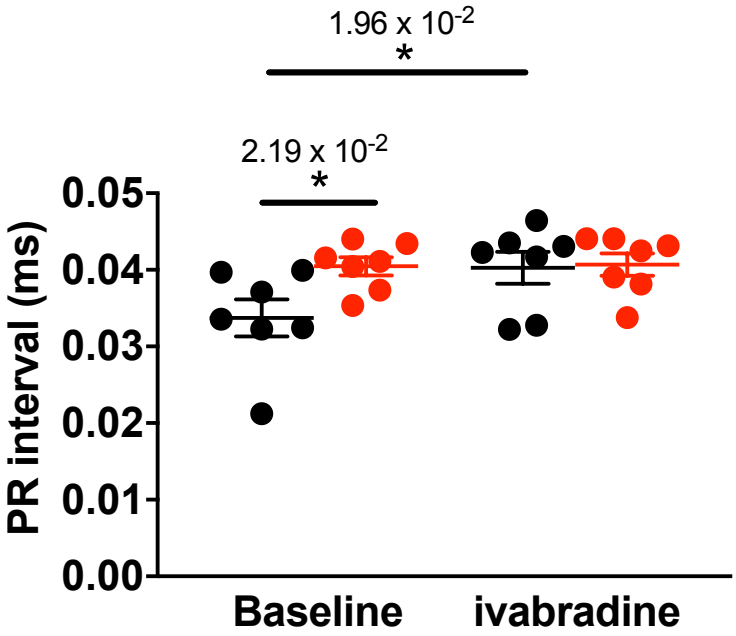

Online Figure VI. I_f block suppresses training-induced PR prolongation in mice. PR interval of anaesthetised sedentary (n=7) and trained mice (n=7) at baseline and after I_f block with ivabradine (*P<0.05, 2-way ANOVA with Sidak's multiple comparisons test). Black points = sedentary mice; red points = trained mice.

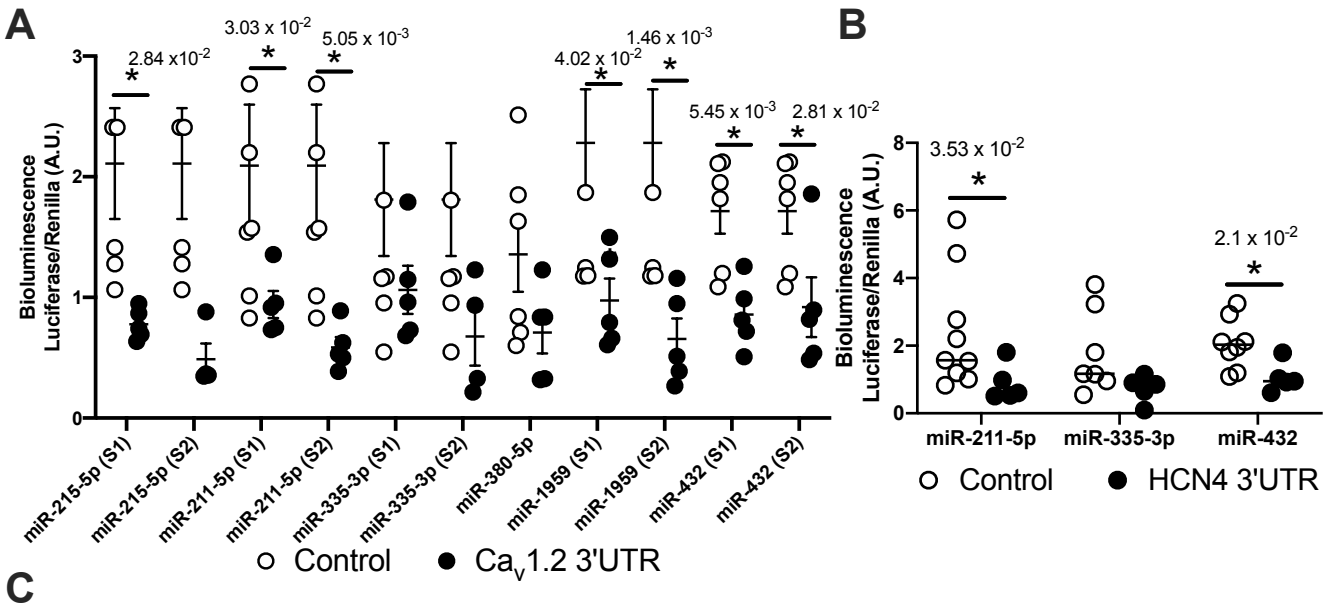

C

Mouse Cav1.2 3'UTR						
miR	**Mature sequence**	**RNA 22**	**miRDB**	**Sfold**	**Luciferase signal (% decrease)**	**Mutagenesis restoration effect (Fig 6D-E)**
mmu-miR-211-5p	UUCCCUUUGUCAUCCUUUGCCU	2128, 3943, 4063	1335, 2624, 4630, 6498	278, 1352, 2641, 3255, 3802, 4647, 4463	38.64 (part b) 43.34 (part c)	Yes
mmu-miR-215-5p	AUGACCUAUGAUUUGACAGAC			1452,1826, 2255, 4102, 4130	50.92 (part a) 45.03 (part b)	No
mmu-miR-335-3p	UUUUUCAUUAUUGCUCCUGACC	495		3435, 1995, 2288, 2180	54.22 (part a) 47.93 (part b)	No
mmu-miR-380-5p	AUGGUUGACCAUAGAACAUGCG	2373		3626, 2319, 4882	38.86 (part b)	No
mmu-miR-1959	GGGGAUGUAGCUCAGUGGAG	789, 773, 1936, 2832, 2867, 3593, 3682, 3854, 4034, 4123, 4500, 6269, 6470, 6537		1900, 2852, 4573	60.70 (part a) 34.24 (part b)	Mutagenesis unsuccessful
mmu-miR-432	UCUUGGAGUAGAUCAGUGGGCAG	2921, 3201, 3971, 6379, 6484		3871, 3987, 3370	45.03 (part b) 45.90 (part c)	No
Mouse HCN4 3'UTR						
miR	**Mature sequence**	**RNA 22**	**miRDB**	**Sfold**	**Luciferase signal (% decrease)**	
mmu-miR-211-5p	UUCCCUUUGUCAUCCUUUGCCU	226, 233			52.83	Yes
mmu-miR-335-3p	UUUUUCAUUAUUGCUCCUGACC	234			47.93	No
mmu-miR-432	UCUUGGAGUAGAUCAGUGGGCAG	49			48.67	Yes

D

4645-4653 nt

```
Cav1.2 : 5′-CUCUACAAACCCAGUGAAGGGAAC-3′
                 | ||      :::|||||||
miR-211-5p: 3′-UCCGU-UUCCUACUGUUUCCCUU-5′
                 | ||      :: ||  | |
Mut :  5′-CUCUACAAACCCAGUCAACCGUAC-3′
```

4102-4108 nt

```
Cav1.2 : 5′-GGGUGGGGAGUGAGGAAAGGUCAA-3′
                ||  |:|  |    ||||||
miR-215-5p: 3′-CAGACAGUUUAGU---AUCCAGUA-5′
                ||  |:|  |    | |  |
Mut :  5′-GGGUGGGGAGUGAGGAAACGAGAA-3′
```

2319-2326 nt

```
Cav1.2 : 5′-GC----UUUGAGGAAAAUAAGACUCAACCAUU-3′
              ||    |:|: ||          ||||||||
miR-380-5p: 3′-GCGUACAAGAUACC----------AGUUGGUA-5′
              ||    |:|: ||          | || ||
Mut :  5′-GC----UUUGAGGAAAAUAAGACUGAAGCAAU-3′
```

3985-3993 nt

```
Cav1.2 : 5′-GAUUUCAAAAGAGCUACUCCAAGC-3′
                ::||   || ||||||||||
miR-432 : 3′-GACGGGU-GACUAGAUGAGGUUCU-5′
                ::||   || |||  | ||
Mut :  5′-GAUUUCAAAAGAGCUAGACGAACC-3′
```

219-229 nt

```
Hcn4: 5′-GGGAGAGAGGGAGGGAGGGAGGGAG-3′
          :||   :|:|||  || ::||||||:
miR-211-5p: 3′-UCC--GUUUCCU-ACUGUUUCCCUU-5′
          :||   :|:|||     :: ||| :
Mut: 5′-GGGAGAGAGGGAGGCUGGGUGGGUG-3′
```

219-229 nt

```
Hcn4: 5′-GGGAGGGAGGGA--GGGAGGGG-3′
          ||  :|||| :|    ||::::
miR 335-3p: 3′-CCAGUCCUCGUUAUUACUUUUU-5′
          ||  :|  | :     | ::::
Mut: 5′-GGGAGGCUGGGU--GGGUGGGG-3′
```

30-39 nt

```
Hcn4: 5′-UUGCUC-CU-UUCUUCCUUCAGGU-3′
          |||:| ||  |||  ||:||:|
miR 432: 3′-GACGGGUGACUAGA-UGAGGUUCU-5′
          || :|  |  | |  ||:||:|
Mut: 5′-UUGGUC-GU-UUGUUCCUUCAGGU-3′
```

Online Figure VII. **miRs dysregulated by training in the AV node target the 3′UTR of $Ca_V1.2$ and HCN4. A,B** Luciferase/Renilla activity of wild type 3′UTR of $Ca_V1.2$ (A) and HCN4 (B) after 24 h miR co-transfection (See Statistical Analysis table for full n numbers and statistical analysis per group. *P<0.05). **C**, Table summarising: bioinformatically predicted binding sites in the 3′UTR of $Ca_V1.2$/HCN4 for selected miRs; the corresponding change in the $Ca_V1.2$/HCN4 3′UTR luciferase signal *versus* control with miR overexpression; and the success of rescuing of this effect with site directed mutagenesis. **D**, Sites selected for mutagenesis experiments with corresponding substitutions underlined in red. Numbers in red denote 3′UTR position with respect to start of 3′UTR.

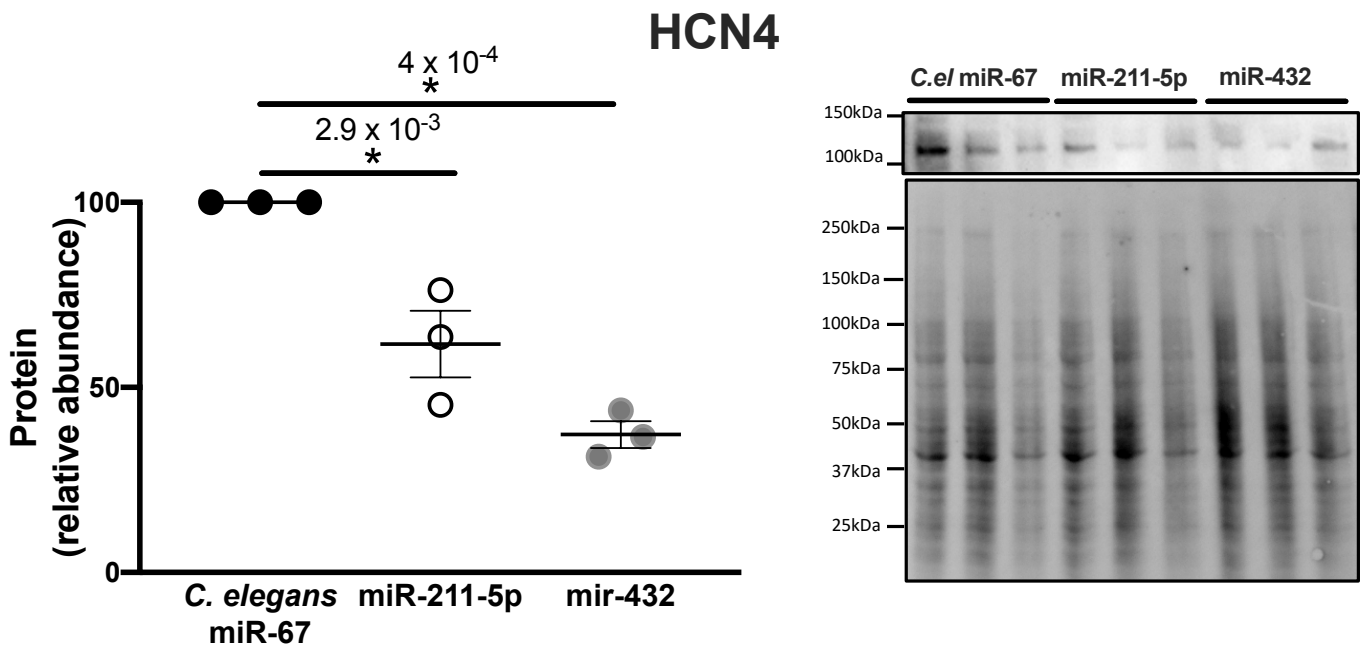

Online Figure VIII. Overexpression of miR-211-5p and miR-432 reduces HCN4 protein levels in embryonic stem cell-derived HCN4/Ca_V1.2 expressing myocytes. Left panel, Mean±SEM HCN4 protein abundance (*P<0.05, Kruskal-Wallis test with Dunn's multiple comparisons test). Abundance expressed as a percentage of that in cells expressing *C. elegans* miR-67 (control). Data from mean of three independent replicates. **Right panel,** Representative HCN4 western blot following 24 h overexpression of *C. elegans* miR-67 (control), miR-211-5p or miR-432. Corresponding stain-free total protein gel used for quantification shown in lower panel.

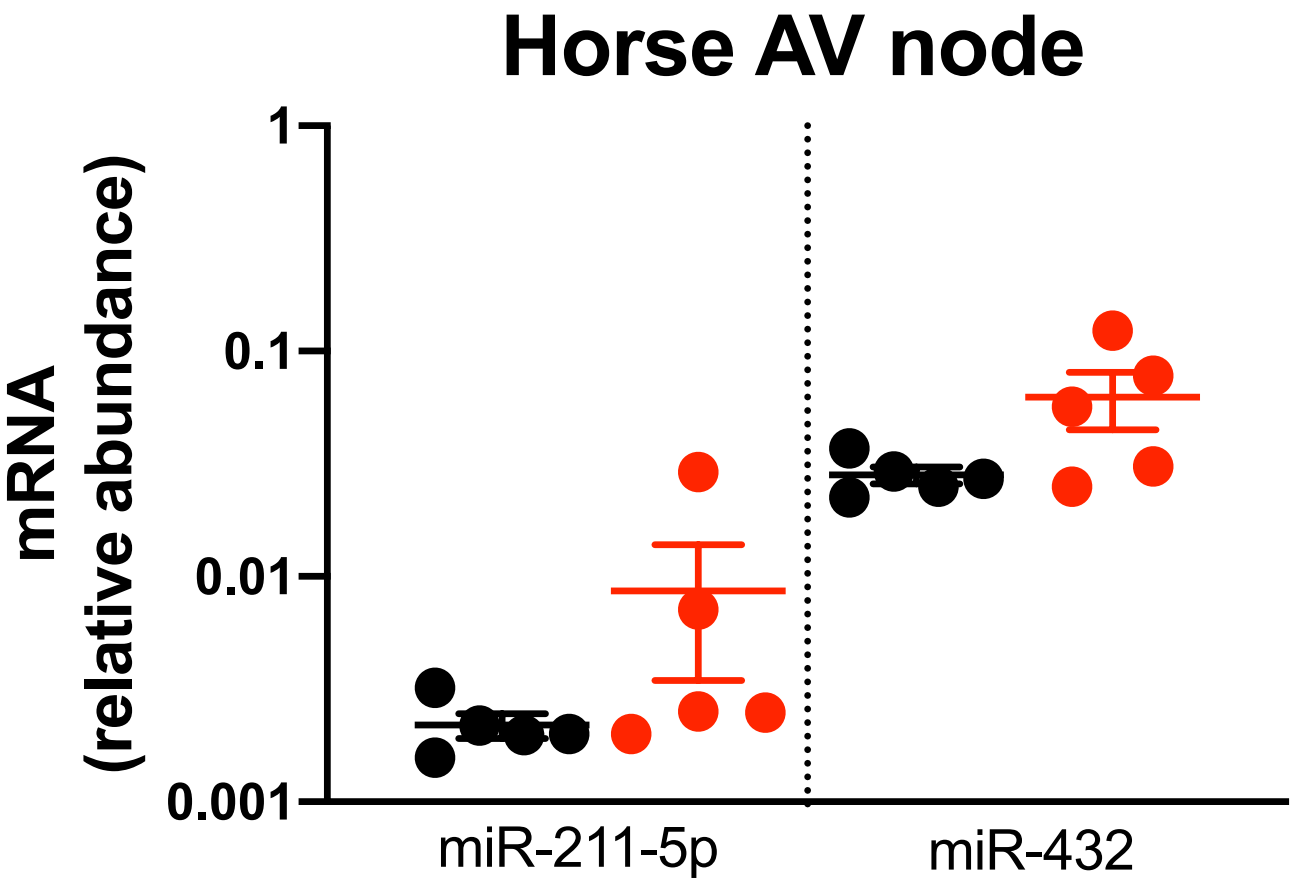

Online Figure IX. miR-211-5p and miR-432 in the horse AV node. Transcript levels of miR 211-5p and miR-432 measured by qPCR in the AV node of sedentary (n=5) and trained (n=5) horses. Expression normalised to *Snord61*, *Snord 95*, *Rnu1a1* and *Rnu6-2*.